Reitman, N.G., Klinger, Y., Briggs, R.W., and Gold, R.D., 2023, Climatic influence on the expression of strike-slip faulting: Geology, https://doi.org/10.1130/G50393.1

Supplementary Material to Accompany:

Climatic Influence on the Expression of Strike-Slip Faulting

By Nadine G. Reitman[1], Yann Klinger[2], Richard W. Briggs[1], and Ryan D. Gold[1]

[1]U.S. Geological Survey, Geologic Hazards Science Center, Golden, Colorado, USA
[2]Université de Paris Cité, Institut de Physique du Globe de Paris, CNRS, Paris, France

Corresponding Author: Nadine Reitman, nreitman@usgs.gov

Disclaimer: Any use of trade, firm, or product names is for descriptive purposes only and does not imply endorsement by the U.S. Government.

Contents:

Supplementary Methods

Data Compilation

We compiled 35 offset measurement datasets from 31 studies of 23 strike-slip faults published in peer-reviewed journals with evidence of multiple strike-slip earthquakes (Figures 1, S1; Table S1) (Lindvall et al., 1989; McGill and Sieh, 1991; Kondo et al., 2005; Mason and Little, 2006; Zielke et al., 2010, 2012; Klinger et al., 2011; Rizza et al., 2011; Li et al., 2012, 2017; Salisbury et al., 2012; De Pascale et al., 2014; Manighetti et al., 2015, 2020; Elliott et al., 2015; Ansberque et al., 2016; Ren et al., 2016; Haddon et al., 2016; Jiang et al., 2017; Han et al., 2019; Kurtz et al., 2018; Chen et al., 2018; Han et al., 2018; Guo et al., 2019; Kang et al., 2020; Bi et al., 2020; Ou et al., 2020; Xiong and Li, 2020; Benjelloun et al., 2021; Zinke et al., 2021; Emre et al., 2021). The compilation is available in Reitman et al., (2022). To ensure we are comparing similar types of data, we excluded three studies (Kondo et al., 2005; Mason and Little, 2006; Emre et al., 2021) from the analysis because the datasets are primarily most recent earthquake (MRE) offsets with <10 cumulative offset measurements. We excluded one study (Chen et al., 2018) because the offsets are a combination of creep and seismogenic slip. We excluded the Superstition Hills fault study (Lindvall et al., 1989) because mean and maximum MRE offset are 0.6 and 0.8 m, respectively, below the resolution of remote sensing methods. Finally, we exclude one study (Xiong and Li, 2020) that covered 2 km of a longer fault, resulting in an order of magnitude greater data density than the other datasets, and the Alpine fault, which has 20 measurements along the 350-km fault length (De Pascale et al., 2014), resulting in one order of magnitude lower data density than the other datasets.

After filtering, the compilation contains 28 offset measurement datasets from 24 studies on 19 strike-slip faults. The faults and fault sections in the filtered compilation are estimated to rupture in M_w ≥6.9-8.1 earthquakes with 11-350 km of fault length investigated in the source study and 53-1800 offset measurements. Slip rate ranges from 0.3-34.0 mm/yr. Approximately 25% of the datasets were collected in the field, 50% via remote methods, and 25% with a mix of field and remote methods.

Mean annual precipitation (MAP) and monthly precipitation variability (MAP CV) data for one location for each fault were taken from the WorldClim2 dataset (Fick and Hijmans, 2017) gridded at ~20 km spacing and averaged over 1970-2000 (Figure 1). The location was chosen as either the epicenter of the most recent earthquake or the approximate center of the offset measurements along the fault (Table S1). Precipitation is reported in cm/yr derived from monthly precipitation data. Precipitation variability is the coefficient of variation (standard deviation/mean, CV) of monthly precipitation. Higher values indicate more variable precipitation rates throughout a year (intra-annual). We consider <25 cm/yr MAP as arid (with <10 cm/yr MAP as extremely arid), 25-50 cm/yr as semi-arid, and >50 cm/yr as wet (with >100 cm/yr as extremely wet) (Holzapfel, 2008).

Comparing global datasets for faults with complex tectonic and climatic settings and histories requires simplifications. We are limited in latitude by where studies have been conducted, cannot include lithologic information because it is not widely available, and choose a single representative location for the fault's precipitation rate. Despite these limitations, we can assess correlations and draw new inferences because we treat all the datasets, which were collected with different intentions by various investigators, with the same processing and analysis.

Calculation of b Values

For each dataset, we plot the offset measurements, reported uncertainties, and locations along the fault if available, and calculate a cumulative offset probability density (COPD) curve (McGill and Sieh, 1991; Zielke et al., 2010; Klinger et al., 2011) and a histogram of all offset measurements (Figure 2; see pages 15-50 for plots for all faults). We clipped the long tails of the offset measurement datasets following the original study or when they become very sparse to ensure dataset compatibility (see pages 51-86 for clipped and unclipped datasets). To ensure consistency across datasets and avoid subjective decision making, we use algorithms with the same parameters to automatically select peaks (Scipy's signal library with the "find_peaks" function) (Virtanen et al., 2020) from the COPD and assign histogram bins (Matplotlib's pyplot library with the "histogram" function) (Hunter, 2007). To find the exponential decay parameter, *b*, for each dataset, we fit exponential decay curves (Scipy's optimize library with the "curve_fit" function) (Virtanen et al., 2020) to the offset measurement datasets for each fault following the equation:

$$y = ae^{-bx} \qquad \text{equation 1}$$

where *y,* the number of measurements, is dependent on offset size, *x*, the rate of decay of large offsets, *b*, and a coefficient that scales by number of measurements, *a*. We calculate the best fit *a* and *b* values for each dataset from (1) all offset measurements plotted from largest to smallest, (2) the peaks in the COPD curve, and (3) the midpoints of the histogram bins. The *b* parameter represents the ratio of small to large offsets in a dataset and exponential decay rate in the occurrence of large offset measurements (Figure 2). Faults with mostly small MRE offsets and only a few large cumulative offsets have higher *b* values. Faults with a more even mix of large cumulative offsets and small offsets have lower *b* values.

To evaluate the effect that measurement approach has on derived *b* values, we compare the exponential decay values derived from all measurements (*b*), COPD peaks, and histogram bins for each dataset. We find b values derived from all measurements and derived from the histogram bins are similar to each other (Pearson $r = 0.72$, $p \approx 0.00$) but different from the values derived from the COPD peaks (Pearson $r = 0.25$, $p = 0.19$) (Figure S3). This could be due to the algorithm used to select COPD peaks missing some small peaks. We use the decay parameter values derived from all measurements in the analysis because deriving it does not require subjective or arbitrary inputs such as selecting prominent peaks from a COPD or bin divisions in a histogram. Furthermore, using b values derived from all measurements is the simplest, most reproducible approach and requires the least data processing.

Finally, we compare the b values from all datasets to tectonic and climate characteristics to test for significant relationships ($p < 0.05$) using the Spearman correlation coefficient. To find the best-fitting relationship between MAP and b value, we tested linear, power-law, exponential, and logarithmic fits to the filtered dataset (Figure S4) and to every permutation of the filtered dataset with one point removed to calculate uncertainty (Figure 3B).

Landscape Evolution Model

We use landscape evolution models that simulate lateral displacement on a section of a strike-slip fault to examine and illustrate tectonic and climatic interaction in a strike-slip landscape. Using the model code of Reitman et al., (2019a) we investigate the influence of mean annual precipitation rate, steady versus variable precipitation, and drastic climate shifts on strike-slip fault geomorphology. Topographic evolution and lateral displacement in time are governed by (Reitman et al., 2019b):

$$\frac{\partial z}{\partial t} = U - V(y)\frac{\partial z}{\partial x} - \left(KA^{1/2}S - E_{crit}\right) + D\nabla^2 z \qquad \text{equation 2}$$

where z is height of the landscape (m), t is time (year), x is fault-parallel direction (m), y is fault-perpendicular direction (m), U is relative rock uplift (m/yr), $V(y)$ is time-averaged lateral displacement rate (m/yr), K is erodibility (yr^{-1}), A is drainage area (m^2), S is slope gradient (positive downward), E_{crit} is a threshold on stream power (m^2/yr), and D is the hillslope diffusivity coefficient (m^2/year). We use an initial topographic surface with self-similar cm-scale random roughness and relative topographic highs in the upper right and left model corners (Figure S2).

We simulate a range of steady dry to wet climates by changing the diffusion rate, D, by one order of magnitude, from $D = 0.001$ to 0.01 m^2/yr (Table S2), values that approximately encompass the natural range for the faults in the compilation. All models have incision rate, $K = 0.001$ yr^{-1}, and we increase K by one order of magnitude in the extra wet (storm) periods in the models that simulate variable precipitation (Table S2). A strike-slip fault crosses the center of the model domain, and all lateral displacement is accommodated on the fault (i.e., no distributed or off-fault deformation) with constant slip along the length of the fault. All models have five, 6-m-slip earthquakes spaced evenly through model run time. We ran models with 3 and 30 mm/yr slip rates for 10,000 and 1,000 years, respectively. All model parameters are given in Table S2.

To simulate a drastic climate shift from a wet to dry period analogous to the end of the Last Glacial Maximum and the transition to the Holocene, we ran a model for 20 kyr with 10 kyr of a wet climate followed by 10 kyr of an arid. A control model was run for 20 kyr with a steady arid climate. Wet climate was simulated with $D = 0.01$ m^2/yr, and arid climate was simulated with $D = 0.001$ m^2/yr (Table S2).

References

Ansberque, C., Bellier, O., Godard, V., Lasserre, C., Wang, M., Braucher, R., Talon, B., De

Sigoyer, J., Xu, X., and Bourlès, D.L., 2016, The Longriqu fault zone, eastern Tibetan Plateau: Segmentation and Holocene behavior: Tectonics, v. 35, p. 565–585, doi:10.1002/2015TC004070.

Benjelloun, Y., de Sigoyer, J., Garambois, S., Carcaillet, J., and Klinger, Y., 2021, Segmentation and Holocene behavior of the middle strand of the North Anatolian fault (NW Turkey): Tectonics, v. 40, p. e2021TC006870, doi:10.1029/2021tc006870.

Bi, H. et al., 2020, Surface slip distribution along the West Helanshan fault, Northern China, and its implications for fault behavior: Journal of Geophysical Research: Solid Earth, v. 125, p. e2020JB019983, doi:10.1029/2020JB019983.

Chen, T., Liu-Zeng, J., Shao, Y., Zhang, P., Oskin, M.E., Lei, Q., and Li, Z., 2018, Geomorphic offsets along the creeping Laohu Shan section of the Haiyuan fault, northern Tibetan Plateau: Geosphere, v. 14, p. 1165–1186, doi:10.1130/GES01561.1.

Elliott, A.J., Oskin, M.E., Liu-Zeng, J., and Shao, Y., 2015, Rupture termination at restraining bends: The last great earthquake on the Altyn Tagh fault: Geophysical Research Letters, v. 42, p. 2164–2170, doi:10.1002/2015GL063107.

Emre, Ö., Kondo, H., Özalp, S., and Elmacı, H., 2021, Fault geometry, segmentation and slip distribution associated with the 1939 Erzincan earthquake rupture along the North Anatolian fault, Turkey: Geological Society, London, Special Publications, v. 501, p. 23–70, doi:10.1144/sp501-2019-141.

Fick, S.E., and Hijmans, R.J., 2017, WorldClim 2: New 1-km spatial resolution climate surfaces for global land areas: International Journal of Climatology, v. 37, p. 4302–4315, doi:10.1002/JOC.5086.

Guo, P., Han, Z., Dong, S., Yuan, R., and Xie, Z., 2019, Surface rupture and slip distribution along the Lenglongling fault in the NE Tibetan Plateau: Implications for faulting behavior: Journal of Asian Earth Sciences, v. 172, p. 190–207, doi:10.1016/j.jseaes.2018.09.008.

Haddon, E.K., Amos, C.B., Zielke, O., Jayko, A.S., and Burgmann, R., 2016, Surface slip during large Owens Valley earthquakes: Geochemistry Geophysics Geosystems, v. 17, p. 2239–2269, doi:10.1002/2015GC006033.

Han, S., Li, H., Pan, J., Lu, H., Zheng, Y., Liu, D., and Ge, C., 2019, Co-seismic surface ruptures in Qiangtang Terrane: Insight into Late Cenozoic deformation of central Tibet: Tectonophysics, v. 750, p. 359–378, doi:10.1016/j.tecto.2018.11.001.

Han, N., Shan, X., Song, X., Ren, Z., Gong, W., and Wang, Z., 2018, Paleoseismic study on the Pingdingshan-Annanba segments of the Altyn Tagh Fault based on offset clusters: Journal of Structural Geology, v. 115, p. 19–27, doi:10.1016/j.jsg.2018.06.020.

Holzapfel, C., 2008, Deserts, *in* Jorgensen, S.E. and Fath, B.D. eds., Encyclopedia of Ecology, Academic Press, p. 879–898, doi:10.1016/B978-008045405-4.00326-8.

Hunter, J.D., 2007, Matplotlib: A 2D graphics environment: Computing in Science and Engineering, v. 9, p. 90–95, doi:10.1109/MCSE.2007.55.

Jiang, W., Zhang, J., Han, Z., Tian, T., Jiao, Q., Wang, X., and Jiang, H., 2017, Characteristic slip of strong earthquakes along the Yishu fault zone in East China evidenced by offset landforms: Tectonics, v. 36, p. 1947–1965, doi:10.1002/2016TC004363.

Kang, W., Xu, X., Oskin, M.E., Yu, G., Luo, J., Chen, G., Luo, H., Sun, X., and Wu, X., 2020, Characteristic slip distribution and earthquake recurrence along the eastern Altyn Tagh fault revealed by high-resolution topographic data: Geosphere, v. 16, p. 392–406, doi:10.1130/GES02116.1.

Klinger, Y., Etchebes, M., Tapponnier, P., and Narteau, C., 2011, Characteristic slip for five

great earthquakes along the Fuyun fault in China: Nature Geoscience, v. 4, p. 389–392, doi:10.1038/ngeo1158.
Kondo, H., Awata, Y., Emre, O., Dogan, A., Ozalp, S., Tokay, F., Yildirim, C., Yoshioka, T., and Okumura, K., 2005, Slip distribution, fault geometry, and fault segmentation of the 1944 Bolu-Gerede earthquake rupture, North Anatolian fault, Turkey: Bulletin of the Seismological Society of America, v. 95, p. 1234–1249, doi:10.1785/0120040194.
Kurtz, R., Klinger, Y., Ferry, M., and Ritz, J.-F., 2018, Horizontal surface-slip distribution through several seismic cycles: The Eastern Bogd fault, Gobi-Altai, Mongolia: Tectonophysics, v. 734–735, p. 167–182, doi:10.1016/j.tecto.2018.03.011.
Li, X., Li, C., Wesnousky, S.G., Zhang, P., Zheng, W., Pierce, I.K.D., and Wang, X., 2017, Paleoseismology and slip rate of the western Tianjingshan fault of NE Tibet, China: Journal of Asian Earth Sciences, v. 146, p. 304–316, doi:10.1016/j.jseaes.2017.04.031.
Li, H., Van Der Woerd, J., Sun, Z., Si, J., Tapponnier, P., Pan, J., Liu, D., and Chevalier, M.-L., 2012, Co-seismic and cumulative offsets of the recent earthquakes along the Karakax left-lateral strike-slip fault in western Tibet: Gondwana Research, v. 21, p. 64–87, doi:10.1016/j.gr.2011.07.025.
Lindvall, S.C., Rockwell, T.K., and Hudnut, K.W., 1989, Evidence of prehistoric earthquakes on the Superstition Hills fault from offset geomorphic features: Bulletin of the Seismological Society of America, v. 79, p. 342–361, doi:10.1785/BSSA0790020342.
Manighetti, I. et al., 2015, Recovering paleoearthquake slip record in a highly dynamic alluvial and tectonic region (Hope Fault, New Zealand) from airborne lidar: Journal of Geophysical Research: Solid Earth, v. 120, p. 3782–3803, doi:10.1002/2014JB011787.
Manighetti, I., Perrin, C., Gaudemer, Y., Dominguez, S., Stewart, N., Malavieille, J., and Garambois, S., 2020, Repeated giant earthquakes on the Wairarapa fault, New Zealand, revealed by Lidar-based paleoseismology: Scientific Reports, v. 10, p. 2124, doi:10.1038/s41598-020-59229-3.
Mason, D.P.M., and Little, T.A., 2006, Refined slip distribution and moment magnitude of the 1848 Marlborough earthquake, Awatere Fault, New Zealand: New Zealand Journal of Geology and Geophysics, v. 49, p. 375–382, doi:10.1080/00288306.2006.9515174.
McGill, S.F., and Sieh, K., 1991, Surficial offsets on the central and eastern Garlock fault associated with prehistoric earthquakes: Journal of Geophysical Research, v. 96, p. 21597-21621, doi:10.1029/91JB02030.
Ou, Q., Kulikova, G., Yu, J., Elliott, A., Parsons, B., and Walker, R., 2020, Magnitude of the 1920 Haiyuan earthquake reestimated using seismological and geomorphological methods: Journal of Geophysical Research: Solid Earth, v. 125, p. e2019JB019244, doi:10.1029/2019JB019244.
De Pascale, G.P., Quigley, M.C., and Davies, T.R.H., 2014, Lidar reveals uniform Alpine fault offsets and bimodal plate boundary rupture behavior, New Zealand: Geology, v. 42, p. 411–414, doi:10.1130/G35100.1.
Reitman, N.G., Mueller, K.J., Tucker, G.E., Gold, R.D., Briggs, R.W., and Barnhart, K.R., 2019a, Numerical model code and input files to run landscape evolution models with strike-slip faulting and measure channel offsets, Zenodo, doi:10.5281/zenodo.3374026.
Reitman, N.G., Klinger, Y., Briggs, R.W., and Gold, R.D., 2022, Compilation of offset measurements and fault data for global strike-slip faults with multiple earthquakes: U.S. Geological Survey data release, doi:10.5066/P9HN0ABD.

Reitman, N.G., Mueller, K.J., Tucker, G.E., Gold, R.D., Briggs, R.W., and Barnhart, K.R., 2019b, Offset channels may not accurately record strike-slip fault displacement: Evidence from landscape evolution models: Journal of Geophysical Research: Solid Earth, v. 124, p. 13427–13451, doi:10.1029/2019JB018596.

Ren, Z., Zhang, Z., Chen, T., Yan, S., Yin, J., Zhang, P., and Zheng, W., 2016, Clustering of offsets on the Haiyuan fault and their relationship to paleoearthquakes: Geological Society of America Bulletin, v. 128, p. 3–18, doi:10.1130/B31155.1.

Rizza, M. et al., 2011, Slip rate and slip magnitudes of past earthquakes along the Bogd left-lateral strike-slip fault (Mongolia): Geophysical Journal International, v. 186, p. 897–927, doi:10.1111/j.1365-246X.2011.05075.x.

Salisbury, J.B., Rockwell, T.K., Middleton, T.J., and Hudnut, K.W., 2012, LiDAR and field observations of slip distribution for the most recent surface ruptures along the central San Jacinto fault: Bulletin of the Seismological Society of America, v. 102, p. 598–619, doi:10.1785/0120110068.

Virtanen, P. et al., 2020, SciPy 1.0: Fundamental algorithms for scientific computing in Python: Nature Methods, v. 17, p. 261–272, doi:10.1038/s41592-019-0686-2.

Xiong, B., and Li, X., 2020, Offset measurements along active faults based on the structure from motion method - A case study of Gebiling in the Xorkoli section of the Altyn Tagh Fault: Geodesy and Geodynamics, v. 11, p. 358–366, doi:10.1016/j.geog.2020.05.005.

Zielke, O., Arrowsmith, J.R., Ludwig, L.G., and Akciz, S.O., 2012, High-resolution topography-derived offsets along the 1857 Fort Tejon earthquake rupture trace, San Andreas Fault: Bulletin of the Seismological Society of America, v. 102, p. 1135–1154, doi:10.1785/0120110230.

Zielke, O., Arrowsmith, J.R., Ludwig, L.G., and Akçiz, S.O., 2010, Slip in the 1857 and earlier large earthquakes along the Carrizo Plain, San Andreas Fault: Science, v. 327, p. 1119–1122, doi:10.1126/science.1182781.

Zinke, R., Dolan, J.F., Rhodes, E.J., Van Dissen, R.J., Hatem, A.E., McGuire, C.P., Brown, N.D., and Grenader, J.R., 2021, Latest Pleistocene–Holocene incremental slip rates of the Wairau Fault: Implications for long-distance and long-term coordination of faulting between North and South Island, New Zealand: Geochemistry, Geophysics, Geosystems, v. 22, p. 1–16, doi:10.1029/2021GC009656.

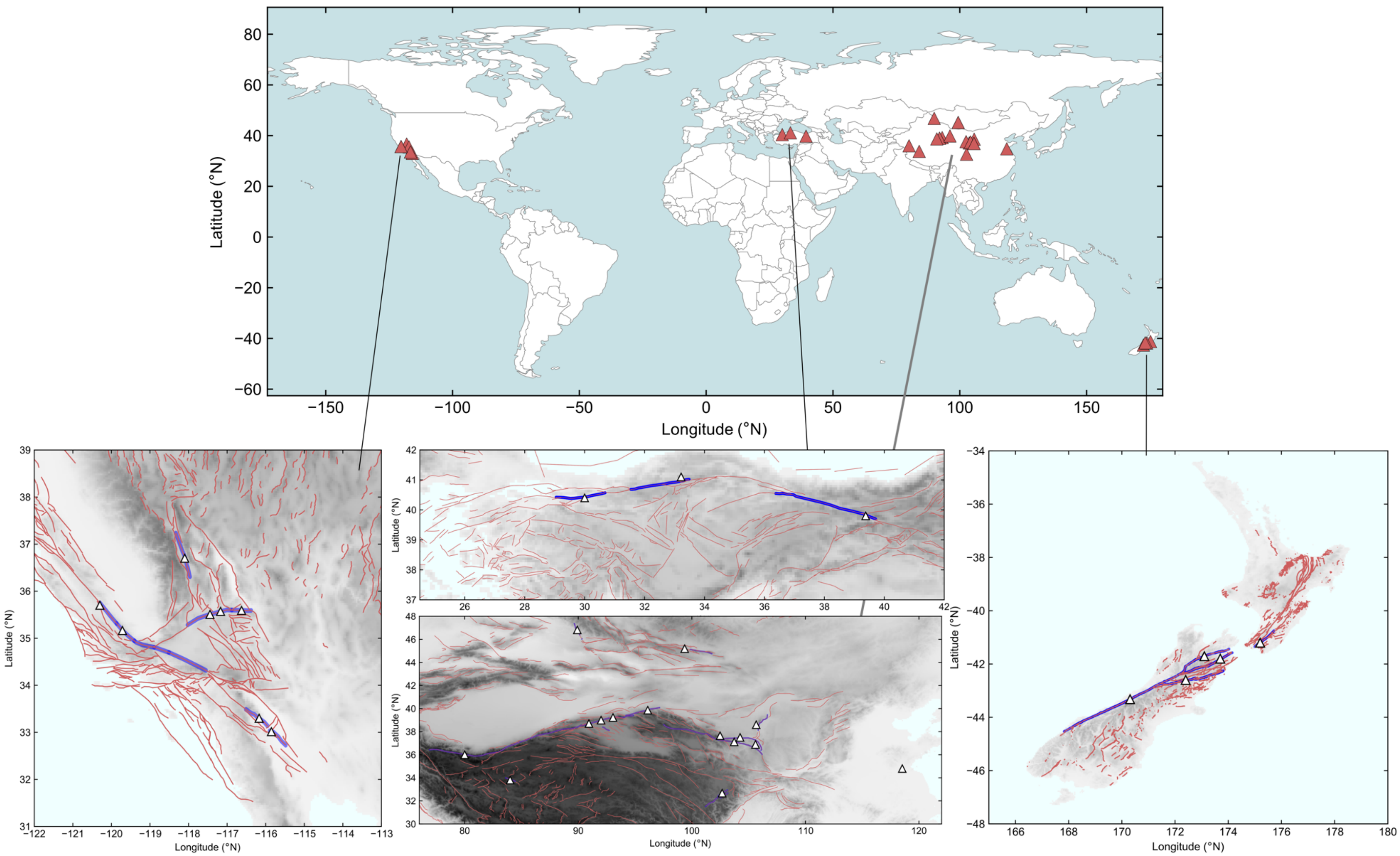

Figure S1: *Locations of faults and fault sections included in the compilation.*

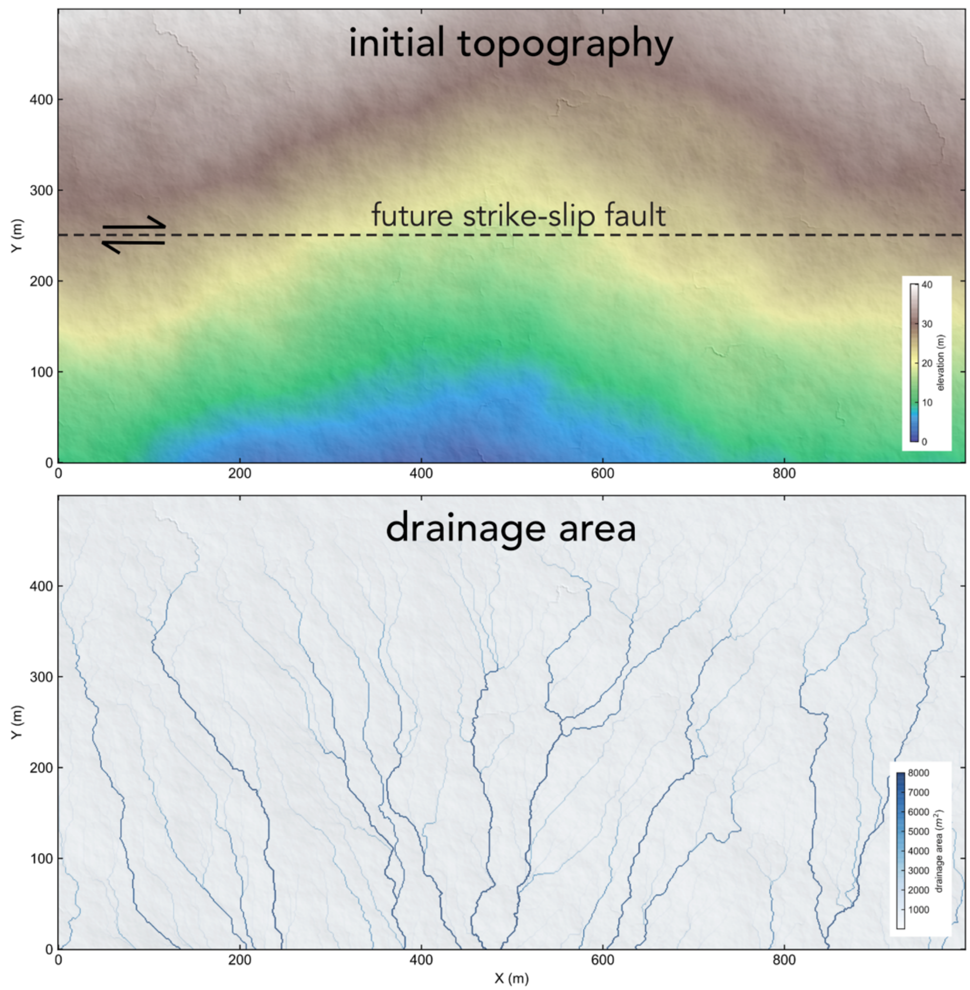

Figure S2: *Initial topographic surface used for landscape evolution models that simulate strike-slip faulting.*

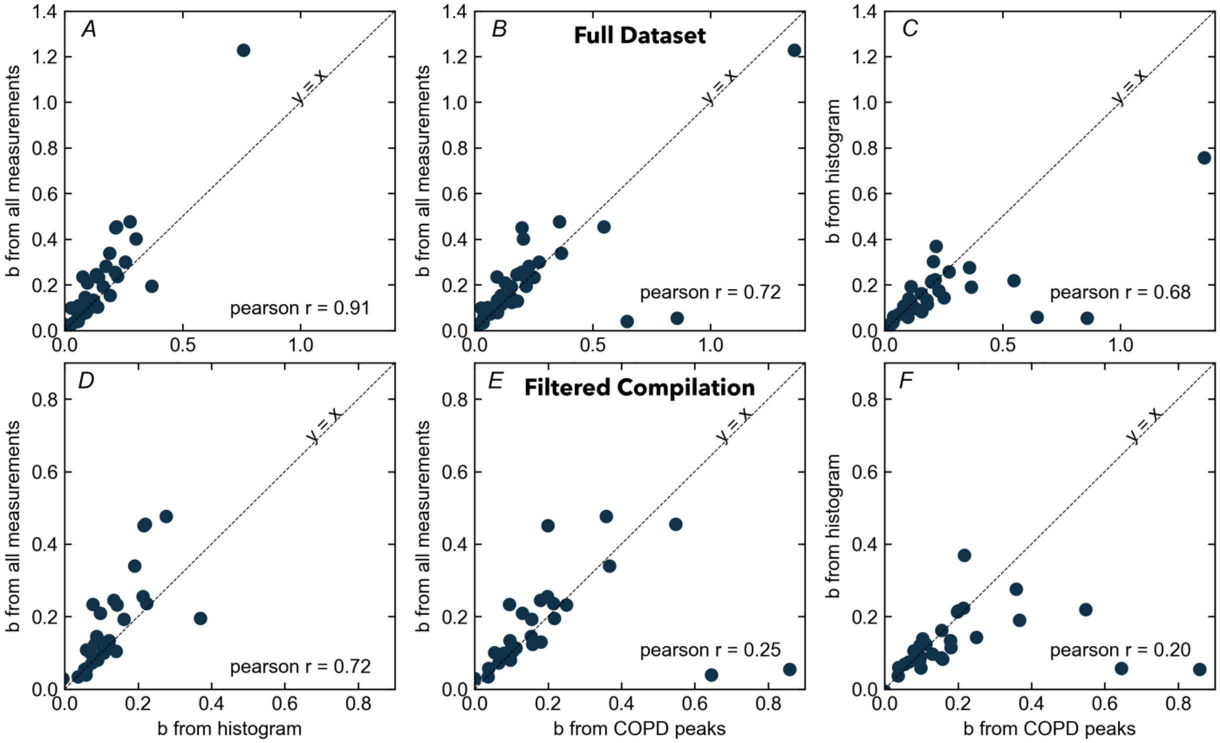

Figure S3: *Exponential decay fits (b values) for b derived from all measurements, COPD peaks, and histogram bin midpoints for the full (A-C) and filtered (D-F) compilations.*

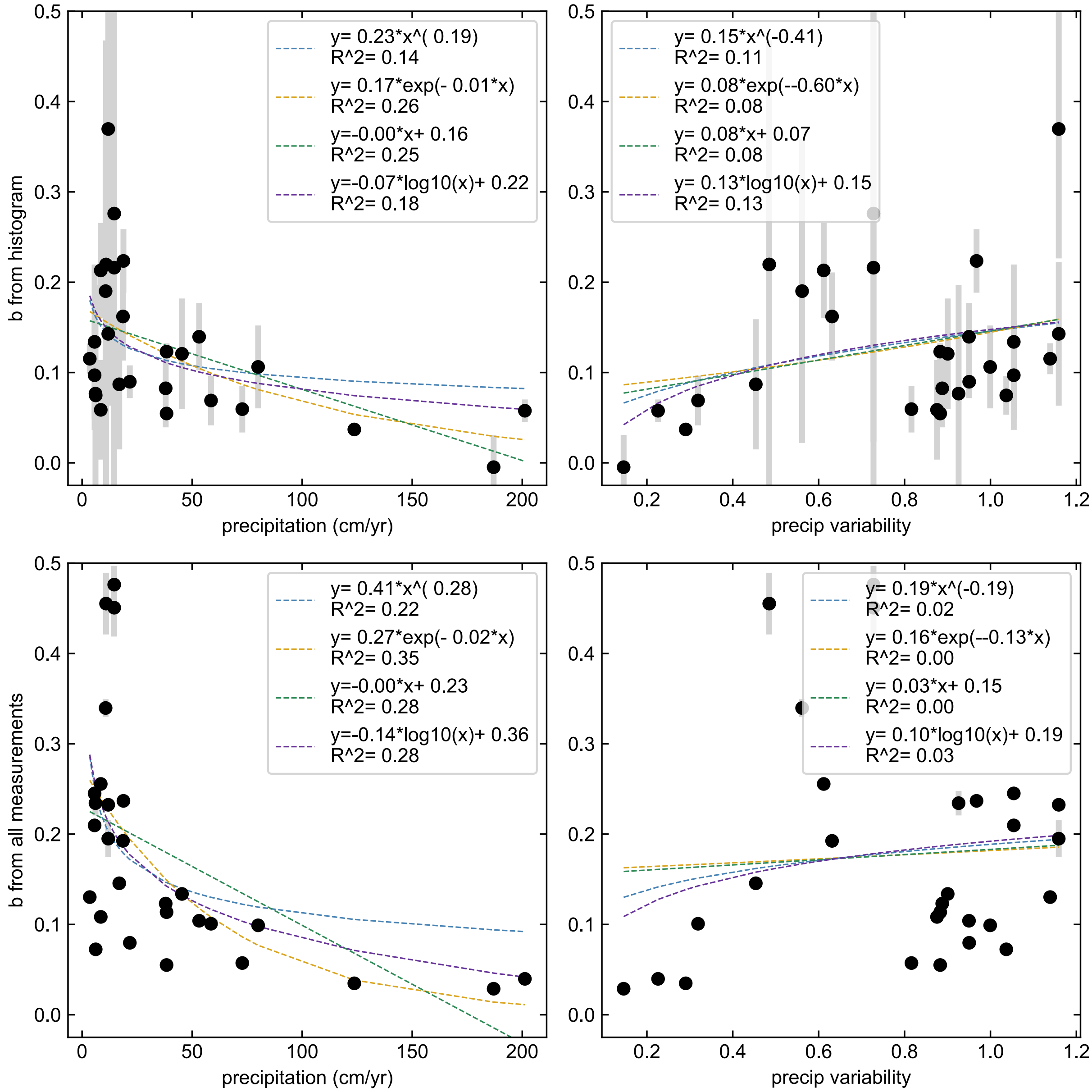

Figure S4: *Fits between b values from the histogram (top) and from all measurements (bottom) and precipitation (left) or precipitation variability (right) for the filtered compilation. Error bars are 2-sigma. Some error bars are smaller than the data point size.*

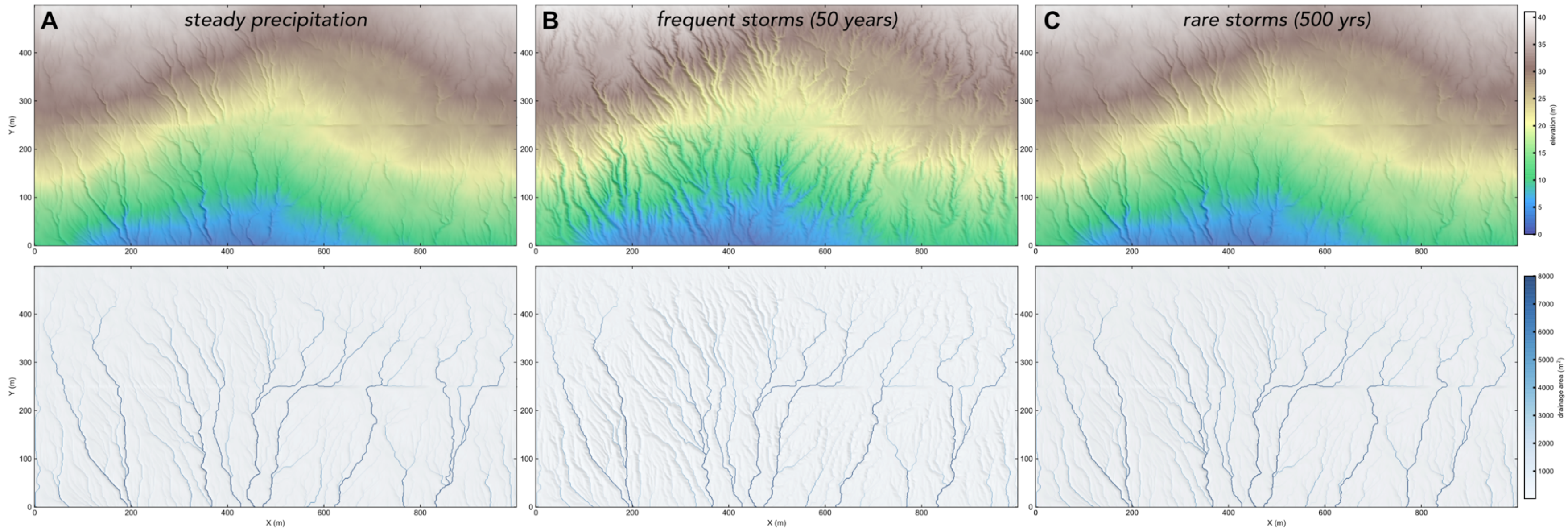

Figure S5: *Testing how storm frequency affects offset development on strike-slip faults. Models with (A) steady precipitation, (B) frequent storms, and (C) rare storms demonstrate little difference in near-fault geomorphology and offset sizes. Earthquakes occur every 200 years in these models.*

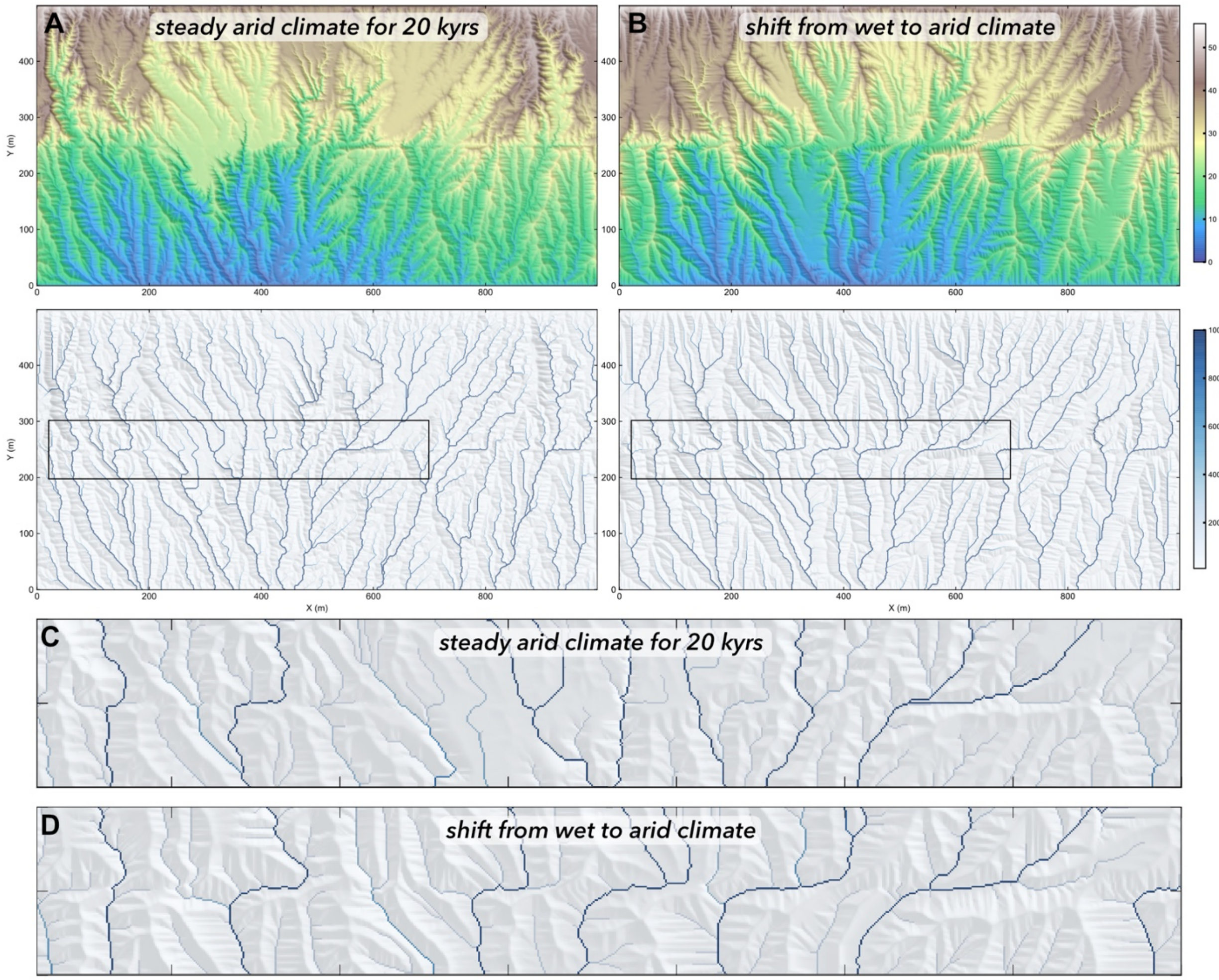

Figure S6: *Testing how climate shifts from wet to dry affect offset development on strike-slip faults. Models with (A) steady arid climate for 20 kyr and (B) a shift from wet to arid climate (10 kry each) demonstrate differences in near-fault geomorphology and offset sizes. Boxes in (A) and (B) are enlarged in (C) and (D) to show the larger offset sizes in the model with a climate shift from wet to arid.*

Table S1: *Offset measurement and fault data.*

Data Source Study	Fault (Section)	Latitude (N)	Longitude (E)	Studied Length (km)	MRE Rupture Length (km)	Slip Rate (mm/yr)	MRE Mw	Mean MRE offset (m)	Time Since MRE (yrs)	Density (#/km)	n offsets	MAP (cm/yr)	MAP CV	Bcopd	Bhist	Bmsmts	Bmsmts Error (2σ)	Exclude?	Reason
Ansberque 2016	Longriqu	32.670	102.670	80	80	3.2	7.2	4.1	5080	0.85	68	72.8	8.2	0.038	0.059	0.057	0.0018		
Benjelloun 2021	Middle North Anatolian (eastern)	40.400	30.000	148	148	4.4	7.3	5	957	0.77	114	58.6	3.2	0.055	0.069	0.101	0.0032		
Bi 2020	West Henlanshan	38.600	105.670	50	86	0.3	7.3	2.5	5495	3.60	180	21.7	9.5	0.097	0.090	0.080	0.0029		
Chen 2018	Haiyuan (Laohu Shan)	37.110	103.730	55	55	4.0	6.6	2.5	134	5.35	294	32.6	9.5	0.112	0.192	0.155	0.0040	Y	Creeping fault
Dspascale 2014	Alpine (1717 rupture)	-43.322	170.310	350	380	27.0	8.1	7.5	305	0.06	20	294.7	2.6	0.027	0.028	0.099	0.0125	Y	Low data density
Elliott 2015	Altyn Tagh (Annanba)	39.220	93.060	45	365	8.0	7.9	7.2	1011	2.60	117	6.1	9.3	0.094	0.077	0.234	0.0136		
Emre 2021	North Anatolian (eastern)	39.800	39.380	330	330	20.0	7.9	4.58	83	0.30	100	49.2	4.9	0.229	0.174	0.282	0.0112	Y	Majority MRE
Guo 2019	Lenglongling	37.591	101.720	110	120	6.4	7.7	4.8	1440	1.75	192	53.2	9.5	0.103	0.140	0.104	0.0023		
Haddon 2016	Owens Valley	36.700	-118.100	113	113	1.1	7.5	3.3	150	1.62	183	18.6	6.3	0.156	0.162	0.193	0.0026		
Han 2018	Altyn Tagh (Xorkoli)	38.990	92.010	120	140	8.0	7.5	3.12	502	1.35	162	5.7	10.5	0.179	0.134	0.245	0.0051		
Han 2018	Altyn Tagh (Xorkoli-Annanba)	38.990	92.010	167	260	8.0	7.6	5	1011	1.21	202	5.7	10.5	0.130	0.097	0.210	0.0047		
Han 2019	Burgar Co	33.800	84.000	88	50	1.5	7.0	1.4	unknown	2.07	182	6.2	10.4	0.065	0.075	0.072	0.0011		
Jiang 2017	Yishu (F5)	34.800	118.530	220	220	2.4	8.1	9	354	1.82	401	80.0	10.0	0.080	0.106	0.099	0.0022		
Kang 2020	Altyn Tagh (eastern)	39.860	96.120	150	180	2.4	7.6	6	2750	2.14	321	8.5	8.8	0.098	0.059	0.108	0.0020		
Klinger 2011	Fuyun	46.817	89.915	100	160	3.0	7.6	6.3	91	5.69	569	16.9	4.5	0.153	0.087	0.146	0.0039		
Kondo 2005	North Anatolian (central)	41.100	33.220	180	180	22.0	7.4	3.4	78	0.36	64	59.2	3.4	0.273	0.257	0.300	0.0156	Y	Majority MRE
Kurtz 2018	Bogd	45.189	99.368	160	360	1.0	8.0	3.5	65	11.25	1800	11.9	11.6	0.250	0.143	0.232	0.0016		
Li 2012	Karakax	36.000	80.000	55	100	6.5	7.5	6.6	1002	3.15	173	3.5	11.4	0.181	0.115	0.130	0.0044		
Li 2017	Tianjingshan (western)	37.500	104.250	11	60	1.2	7.4	3.5	1202	21.82	240	18.8	9.7	0.214	0.224	0.237	0.0031		
Lindvall 1989	Superstition Hills	33.015	-115.852	23.5	23.5	3.0	6.6	0.6	35	3.23	76	8.5	6.5	1.356	0.757	1.229	0.0815	Y	Small offsets
Manighetti 2015	Hope (eastern)	-42.600	172.400	30	30	23.0	7.2	4.4	134	4.77	143	201.2	2.3	0.646	0.058	0.040	0.0019		
Manighetti 2020	Wairarapa	-41.200	175.200	70	135	10.0	8.1	14.6	167	9.54	668	123.7	2.9	0.036	0.037	0.035	0.0002		
Mason 2006	Awatere	-41.800	173.700	110	110	5.8	7.5	5.3	174	0.38	42	134.0	1.6	0.207	0.303	0.402	0.0316	Y	Majority MRE
McGill 1991	Garlock (central & eastern)	35.570	-117.170	130	148	5.0	7.5	3.5	477	1.73	225	10.7	5.6	0.367	0.190	0.340	0.0098		
McGill 1991	Garlock (central)	35.506	-117.444	80	148	5.3	7.5	3.5	477	1.55	124	8.5	6.1	0.199	0.213	0.256	0.0047		
McGill 1991	Garlock (eastern)	35.591	-116.626	30	148	5.0	6.9	2.5	477	3.37	101	10.9	4.8	0.547	0.220	0.455	0.0342		
Ou 2020	Haiyuan	36.481	105.540	237	237	3.9	7.9	3.75	102	1.70	402	38.4	8.8	0.112	0.123	0.114	0.0016		
Ren 2016	Haiyuan	36.481	105.540	88	237	4.5	7.9	3.4	102	4.72	415	38.4	8.8	0.858	0.055	0.055	0.0004		
Rizza 2011	Bogd	45.189	99.368	100	260	1.0	7.9	4	65	0.53	53	11.9	11.6	0.217	0.370	0.195	0.0204		
Salisbury 2012	San Jacinto (Clark)	33.299	-116.170	80	80	14.0	7.4	2.7	222	2.86	229	14.6	7.3	0.359	0.276	0.476	0.0207		
Salisbury 2012	San Jacinto (Clark)	33.299	-116.170	80	80	14.0	7.4	2.7	222	2.46	197	14.6	7.3	0.200	0.216	0.451	0.0319		
Xiong 2020	Altyn Tagh (Xorkoli)	38.700	90.940	2	140	8.0	7.9	7.1	502	101.00	202	7.2	11.2	0.013	0.023	0.023	0.0006	Y	High data density; short length studied
Zielke 2010	San Andreas (Carrizo Plain)	35.164	-119.714	60	350	34.0	7.9	5.3	165	2.48	149	45.4	9.0	0.095	0.121	0.134	0.0038		
Zielke 2012	San Andreas (1857 rupture)	35.700	-120.300	350	350	34.0	7.9	3.5	165	1.27	443	38.0	8.9	0.158	0.083	0.123	0.0024		
Zinke 2021	Wairau (central)	-41.708	173.102	35	140	5.0	7.5	7.7	2000	1.86	65	187.0	1.5	0.000	-0.005	0.029	0.0028		

**Underlined entries are the minimum and maximum values in each column.*
MAP: mean annual precipitation derived from monthly precipitation
MAP CV: coefficient of variation of monthly precipitation
MRE: most recent earthquake
Bcopd: b value from COPD peaks
Bhist: b value from histogram bin midpoints
Bmsmts: b value from all measurements

Table S2: *Parameters for landscape evolution model runs.*

Model Name	*K (/yr)*	*Kstorm (/yr)*	*D (m^2/yr)*	*Slip Rate (mm/yr)*	*Model Run Time (yr)*	*Time Step (yr)*	*Total Slip (m)*	*Slip per Event (m)*	*Earthquake Recurrence (yr)*	*Storm Recurrence (yr)*	*Precipitation*
k001d001frac1k30mm	0.001	n/a	0.001	30	1000	1	30	6	200	n/a	steady
k001d005frac1k30mm	0.001	n/a	0.005	30	1000	1	30	6	200	n/a	steady
k001d01frac1k30mm	0.001	n/a	0.01	30	1000	1	30	6	200	n/a	steady
k001d001frac10k3mm	0.001	n/a	0.001	3	10000	1	30	6	2000	n/a	steady
k001d005frac10k3mm	0.001	n/a	0.005	3	10000	1	30	6	2000	n/a	steady
k001d01frac10k3mm	0.001	n/a	0.01	3	10000	1	30	6	2000	n/a	steady
k001d001frac20k3mm	0.001	n/a	0.001	3	20000	1	60	6	2000	n/a	steady
k001d01frac20k3mm_dshift001	0.001	n/a	0.01-->0.001	3	20000	1	60	6	2000	n/a	shift
k001d005frac1k30mm_storm_rare	0.001	0.1	0.005	30	1000	1	30	6	200	500	variable
k001d005frac1k30mm_storm_freq	0.001	0.1	0.005	30	1000	1	30	6	200	50	variable

Plots of clipped versus full datasets:

In the following plots, black circles are offset measurements included in the clipped dataset and blue circles are offset measurements excluded from the clipped dataset. The left panel shows offset measurements along the fault with uncertainty ranges. If distance along the fault is not provided, then offsets are plotted from smallest to largest. The right panel shows offset measurements plotted from smallest to largest.

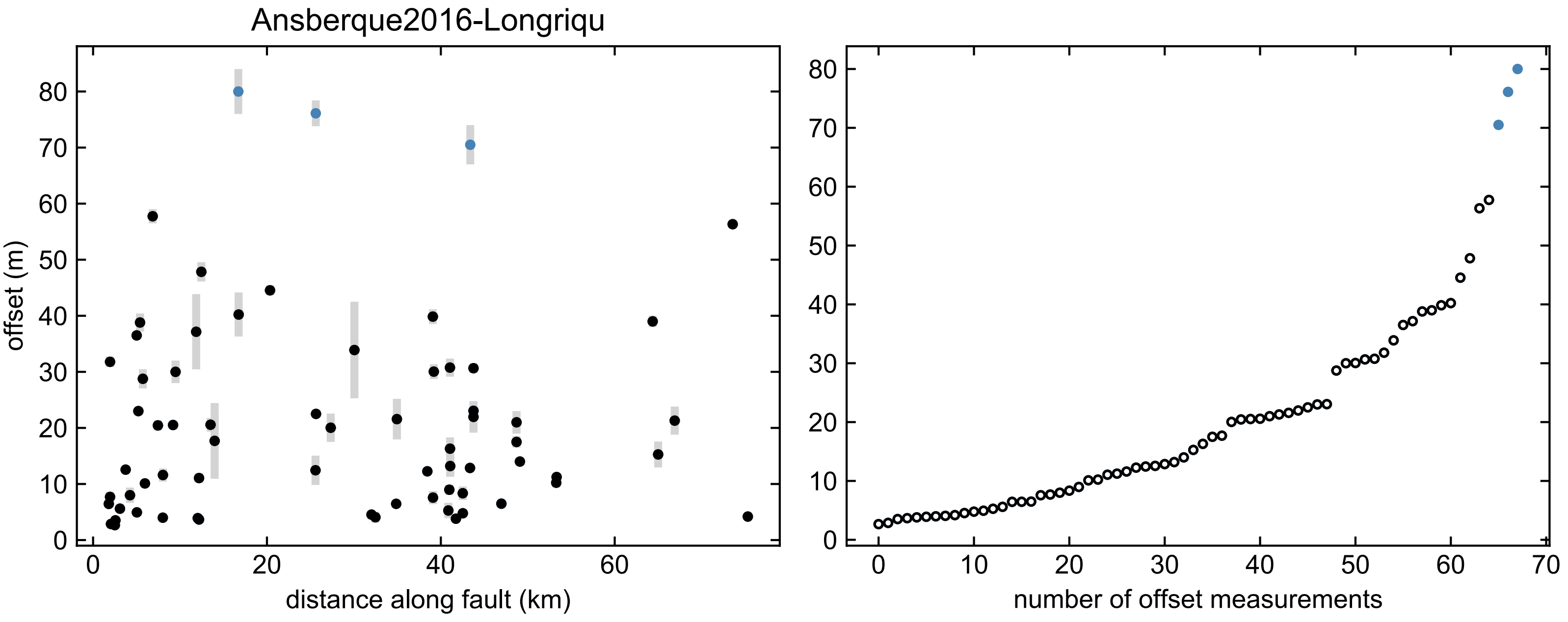

Ansberque2016-Longriqu
offset (m)
distance along fault (km)
number of offset measurements
0
10
20
30
40
50
60
70
80

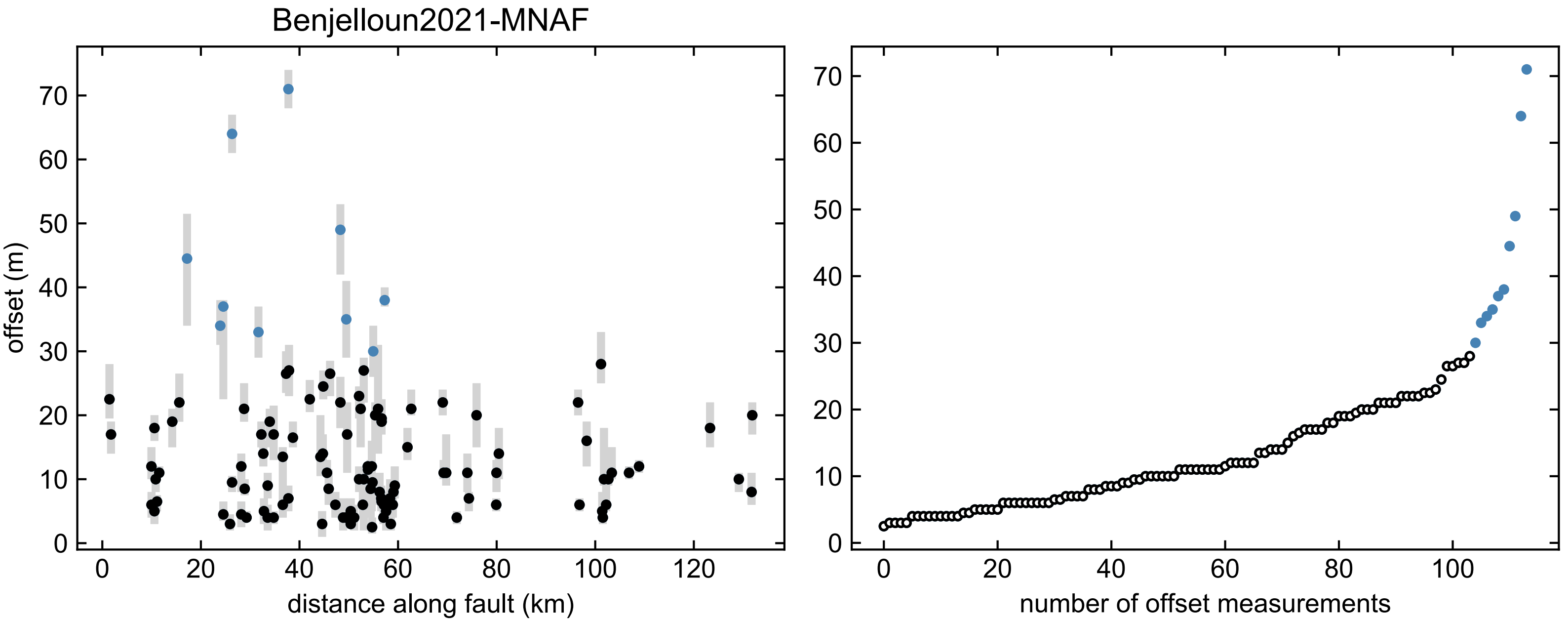

Benjelloun2021-MNAF
offset (m)
distance along fault (km)
number of offset measurements
0
10
20
30
40
50
60
70
0
20
40
60
80
100
120

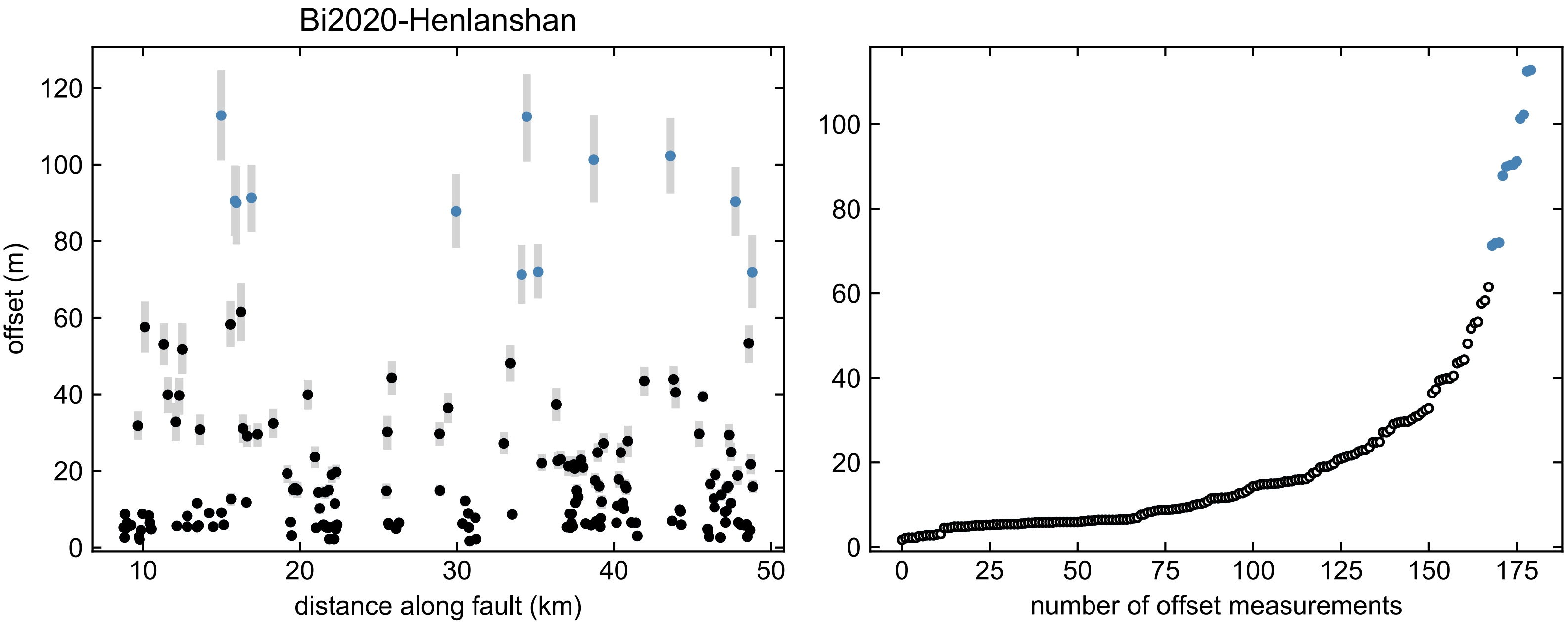
Bi2020-Henlanshan
offset (m)
distance along fault (km)
number of offset measurements
0
20
40
60
80
100
120
10
20
30
40
50
0
25
50
75
100
125
150
175

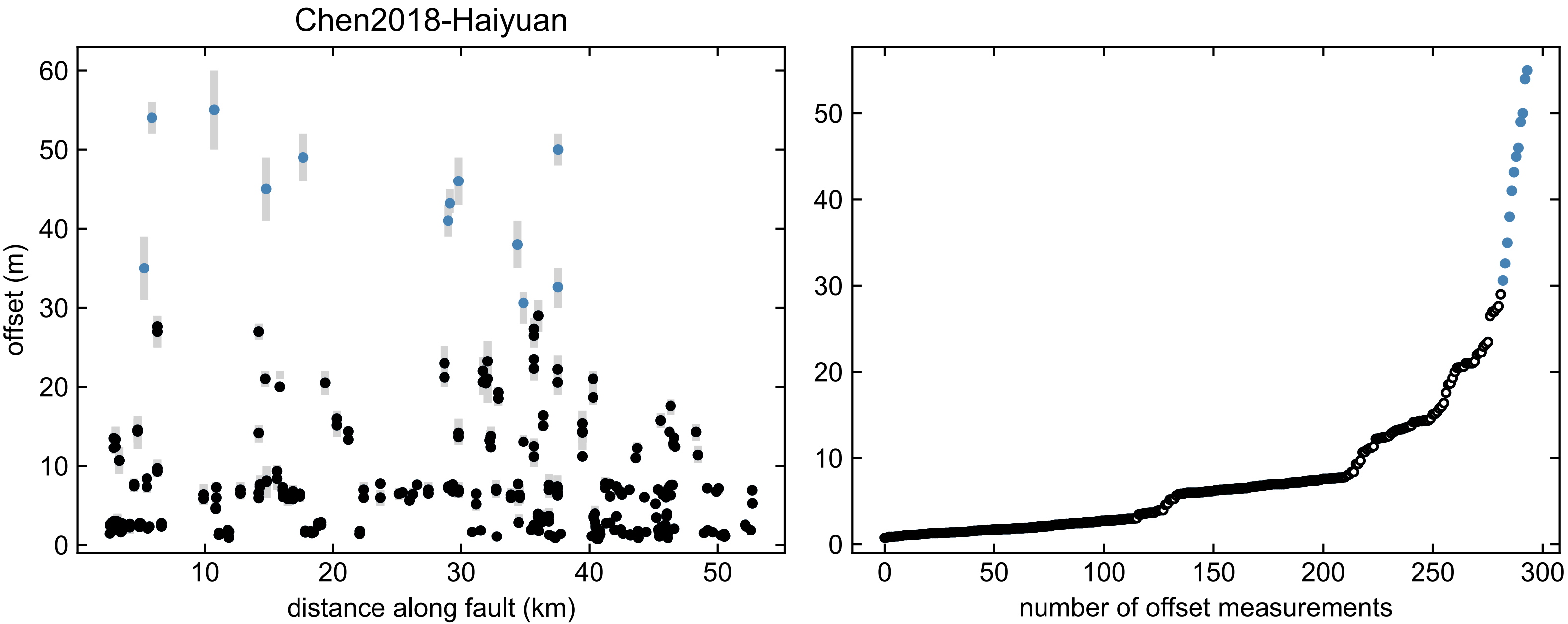
Chen2018-Haiyuan
offset (m)
0
10
20
30
40
50
60
10
20
30
40
50
distance along fault (km)
0
10
20
30
40
50
0
50
100
150
200
250
300
number of offset measurements

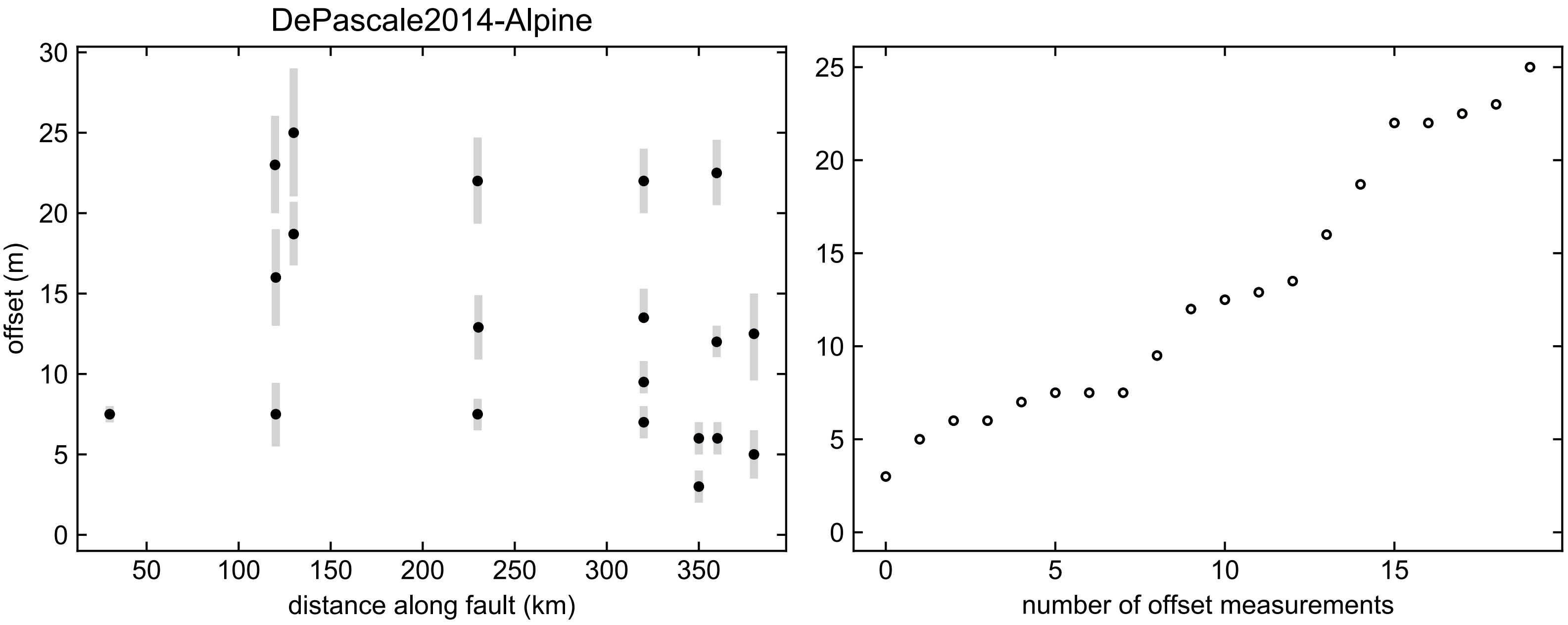
DePascale2014-Alpine
offset (m)
distance along fault (km)
number of offset measurements
0
5
10
15
20
25
30
50
100
150
200
250
300
350

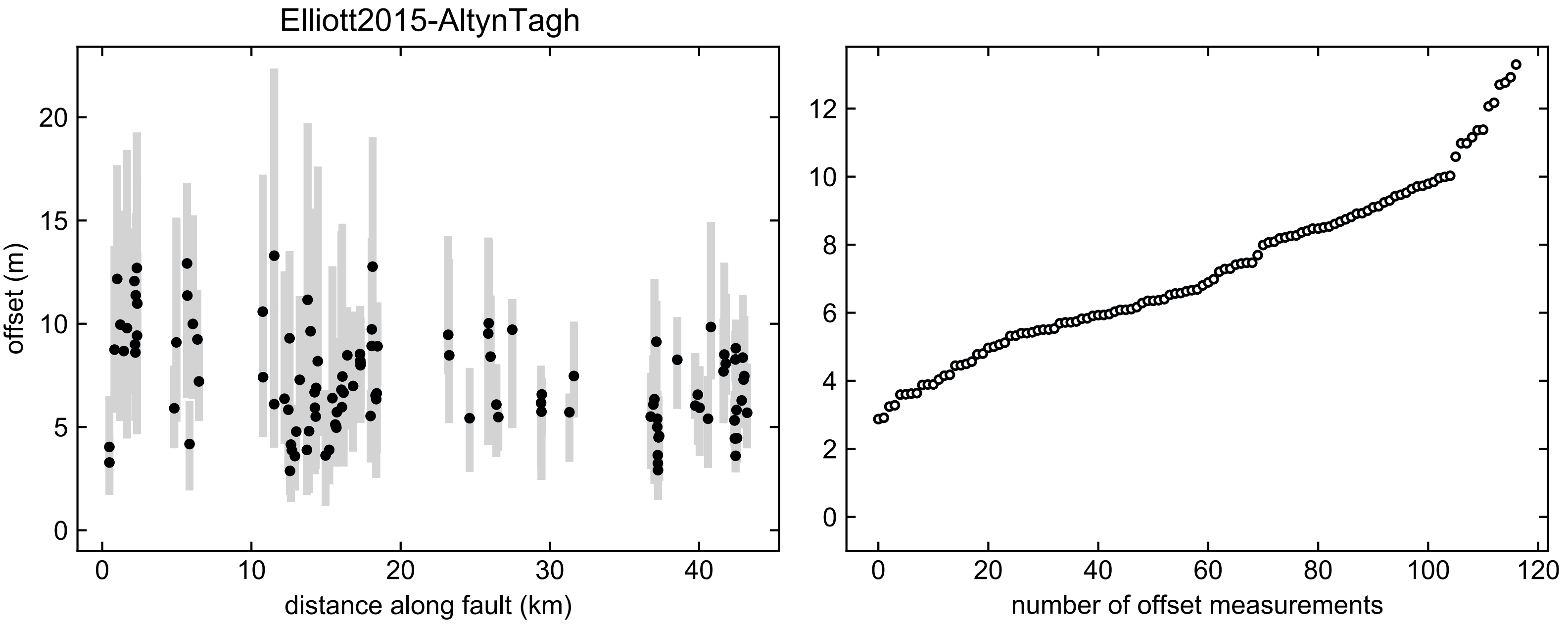
Elliott2015-AltynTagh
offset (m)
distance along fault (km)
number of offset measurements
0
5
10
15
20
0
10
20
30
40
0
2
4
6
8
10
12
0
20
40
60
80
100
120

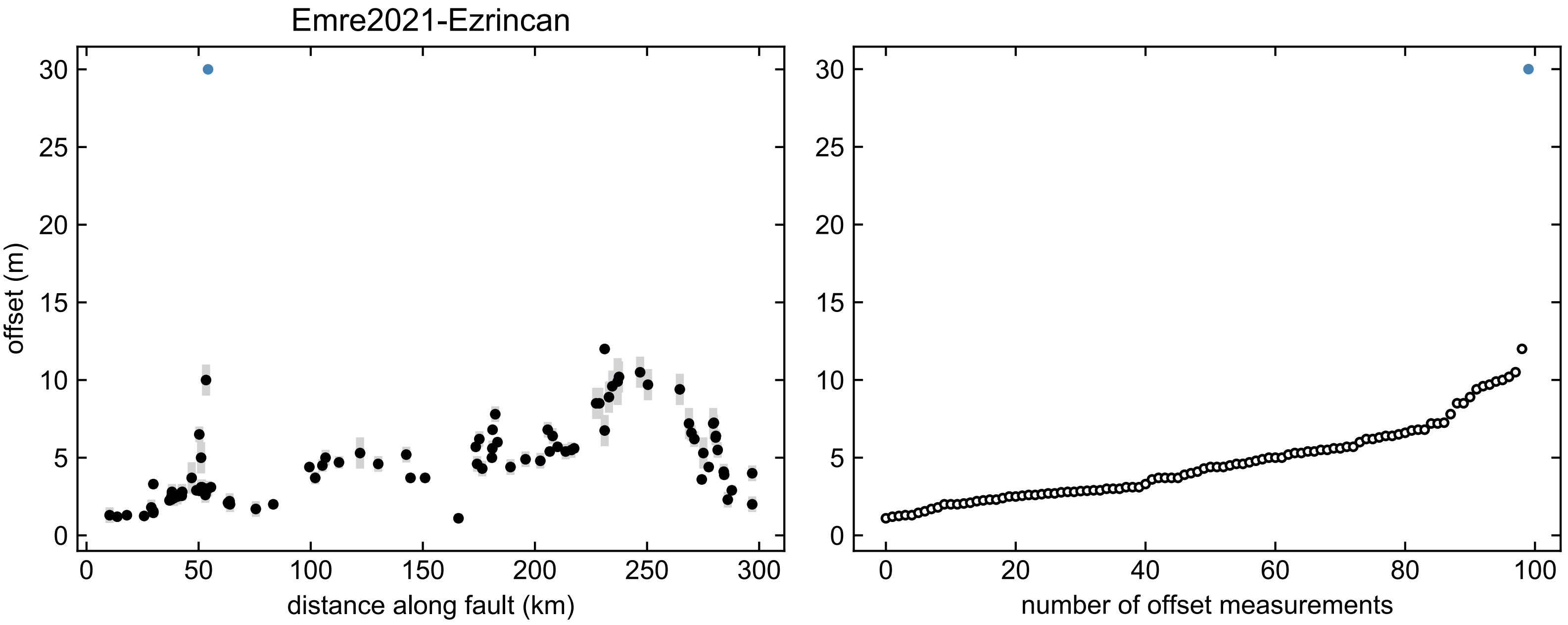

Emre2021-Ezrincan
offset (m)
distance along fault (km)
number of offset measurements
0
5
10
15
20
25
30
0
50
100
150
200
250
300
0
20
40
60
80
100

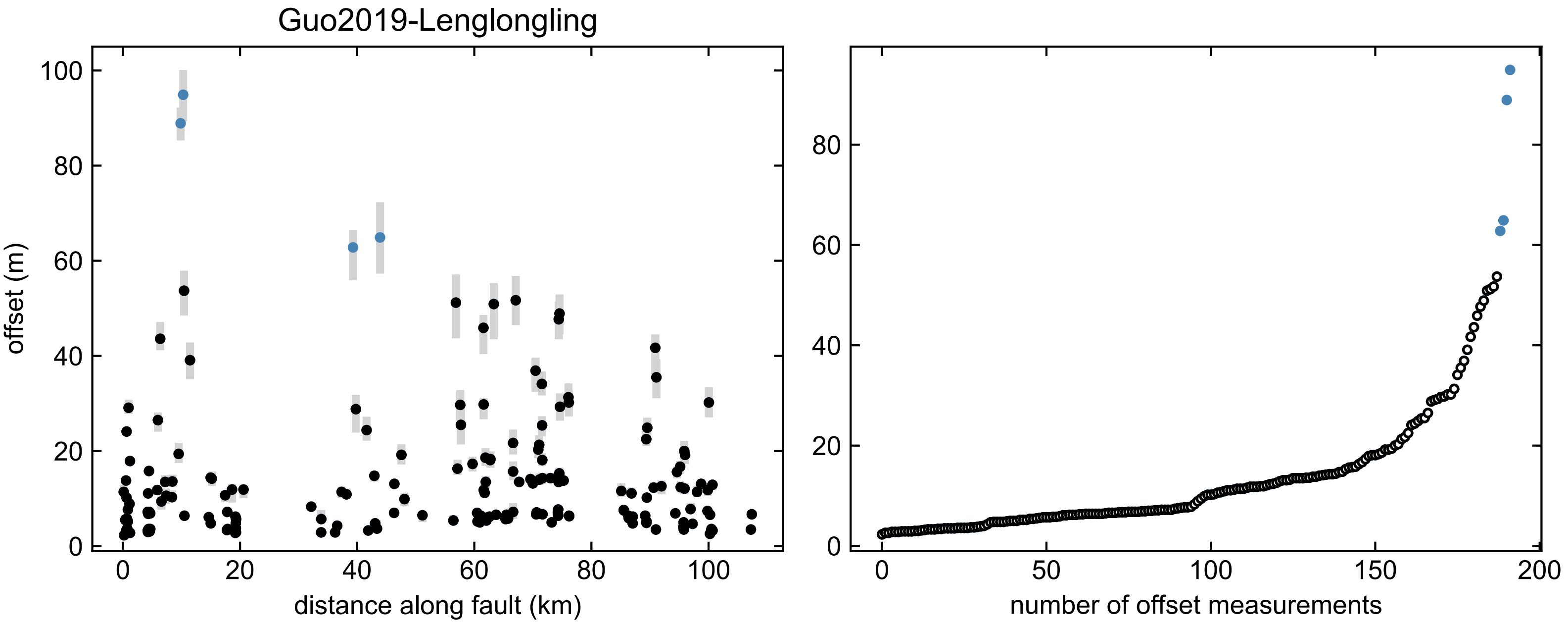

Guo2019-Lenglongling
offset (m)
distance along fault (km)
number of offset measurements

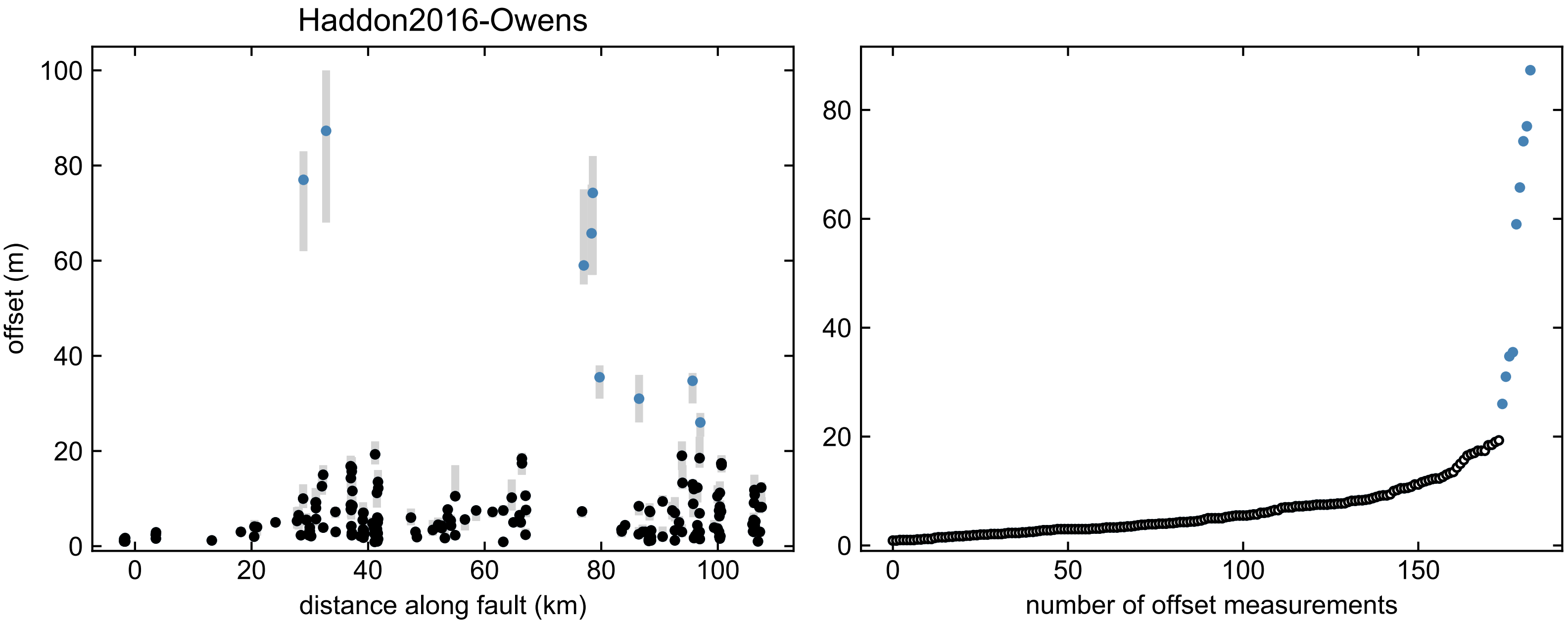

Haddon2016-Owens
offset (m)
100
80
60
40
20
0
0
20
40
60
80
100
distance along fault (km)
80
60
40
20
0
0
50
100
150
number of offset measurements

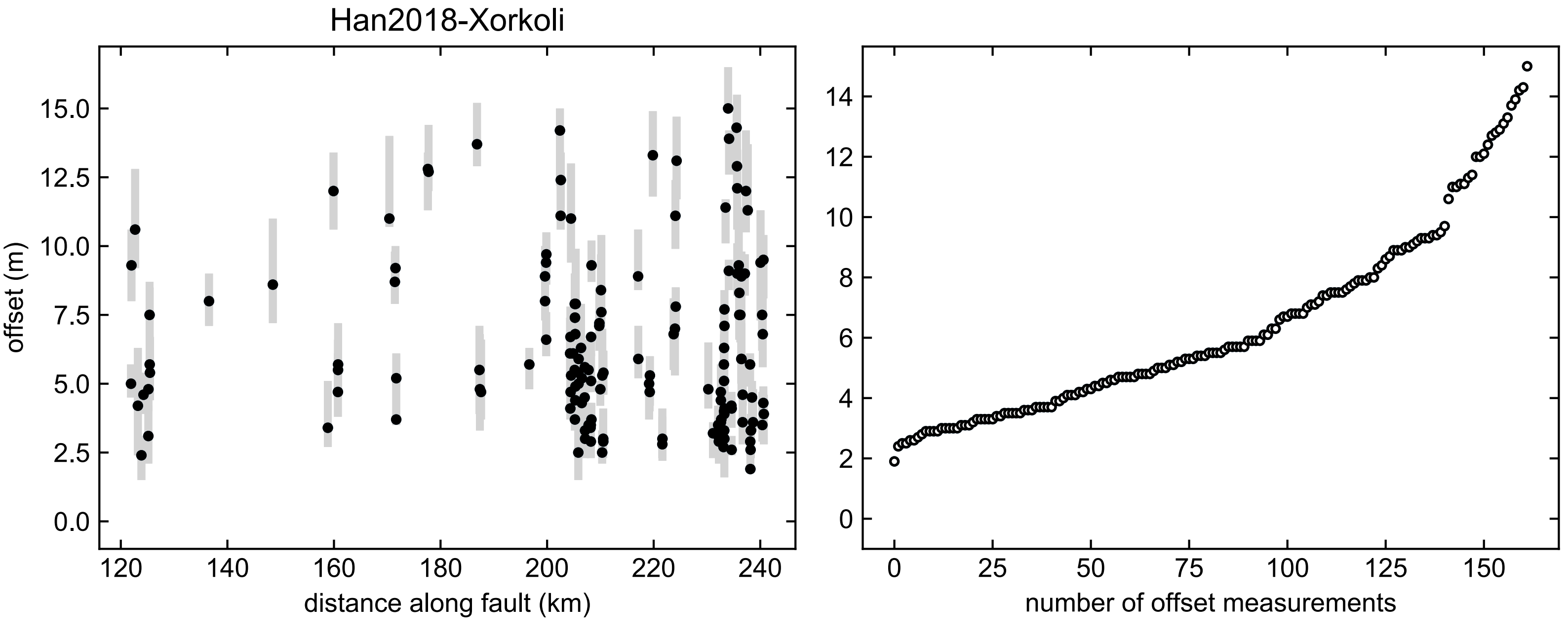
Han2018-Xorkoli
offset (m)
distance along fault (km)
number of offset measurements

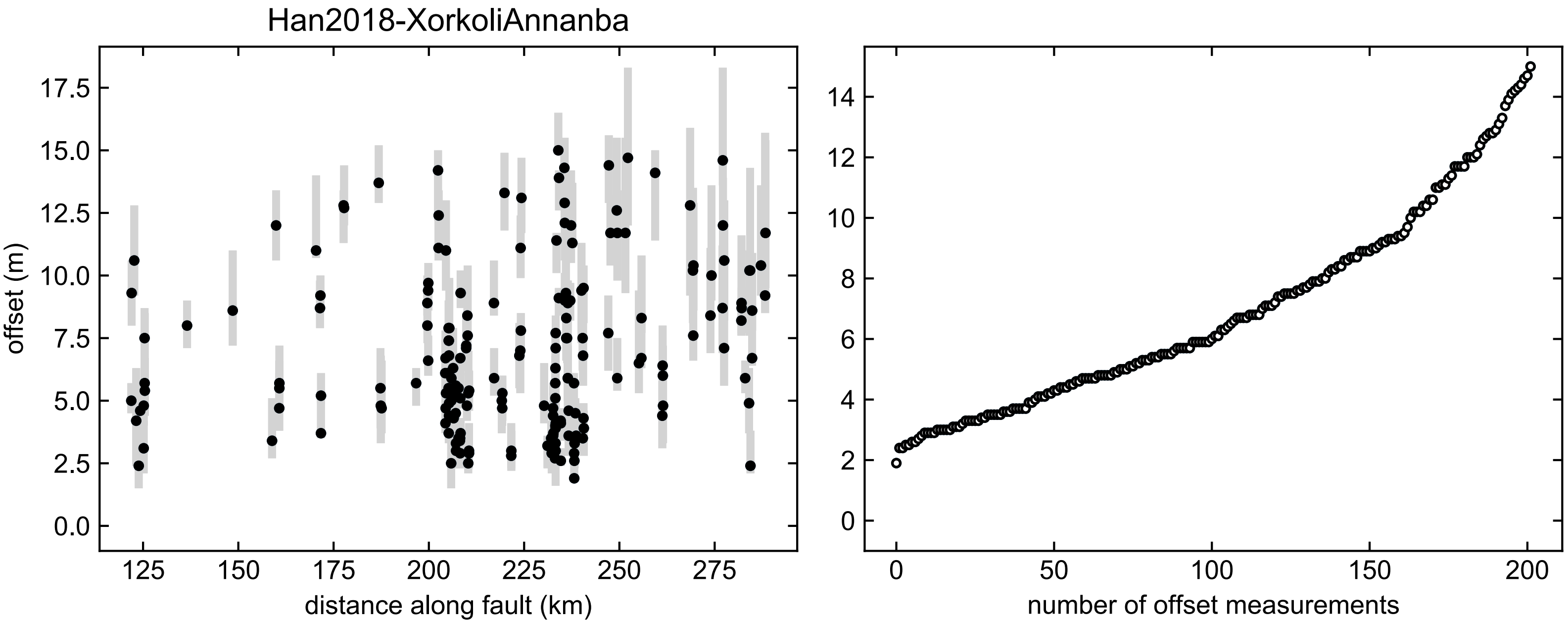
Han2018-XorkoliAnnanba
offset (m)
0.0
2.5
5.0
7.5
10.0
12.5
15.0
17.5
125
150
175
200
225
250
275
distance along fault (km)
0
2
4
6
8
10
12
14
0
50
100
150
200
number of offset measurements

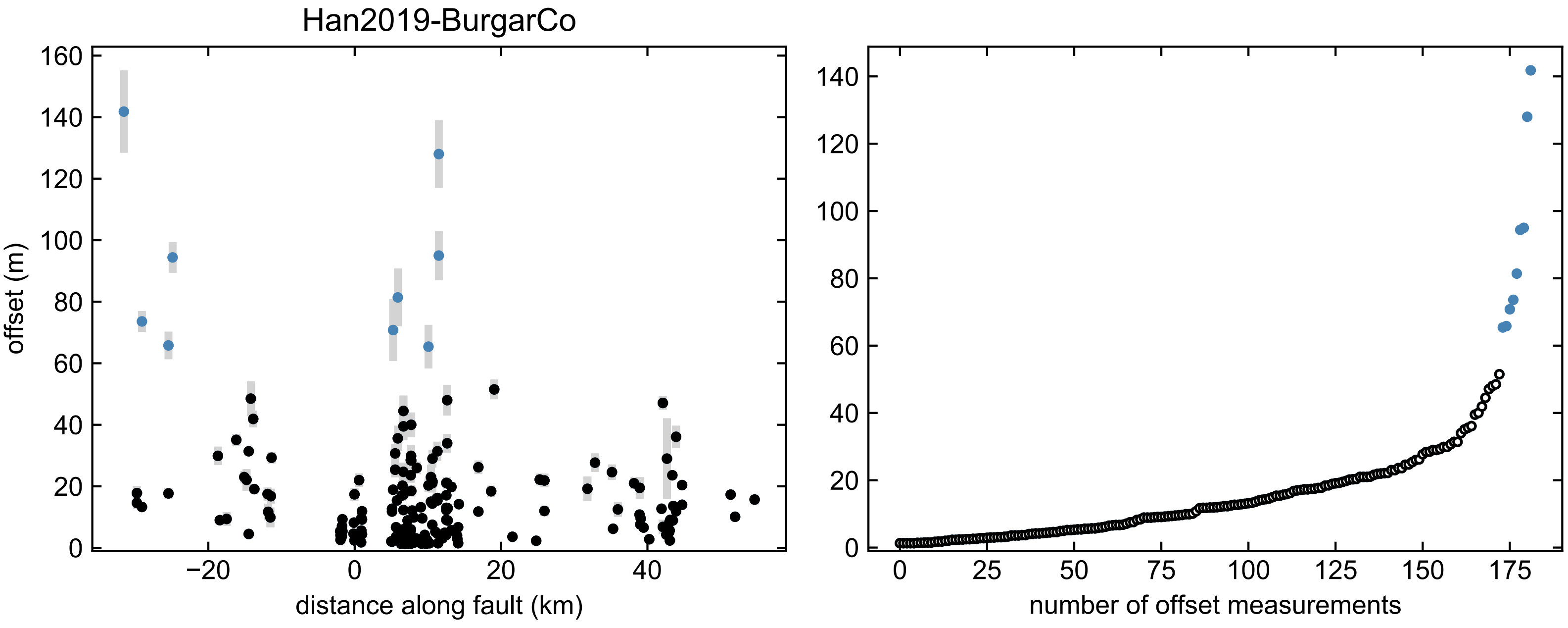
Han2019-BurgarCo
offset (m)
distance along fault (km)
number of offset measurements
160
140
120
100
80
60
40
20
0
−20
0
20
40
0
25
50
75
100
125
150
175

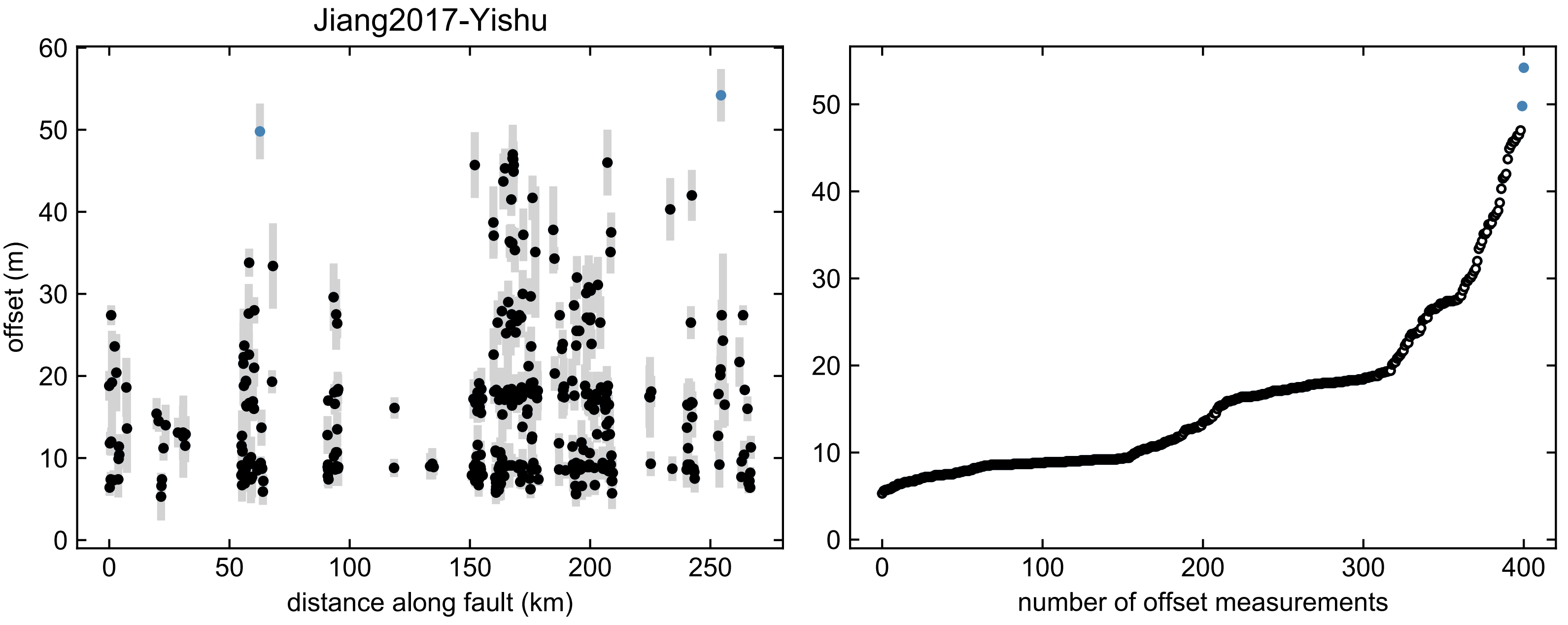
Jiang2017-Yishu
offset (m)
0
10
20
30
40
50
60
0
50
100
150
200
250
distance along fault (km)
0
10
20
30
40
50
0
100
200
300
400
number of offset measurements

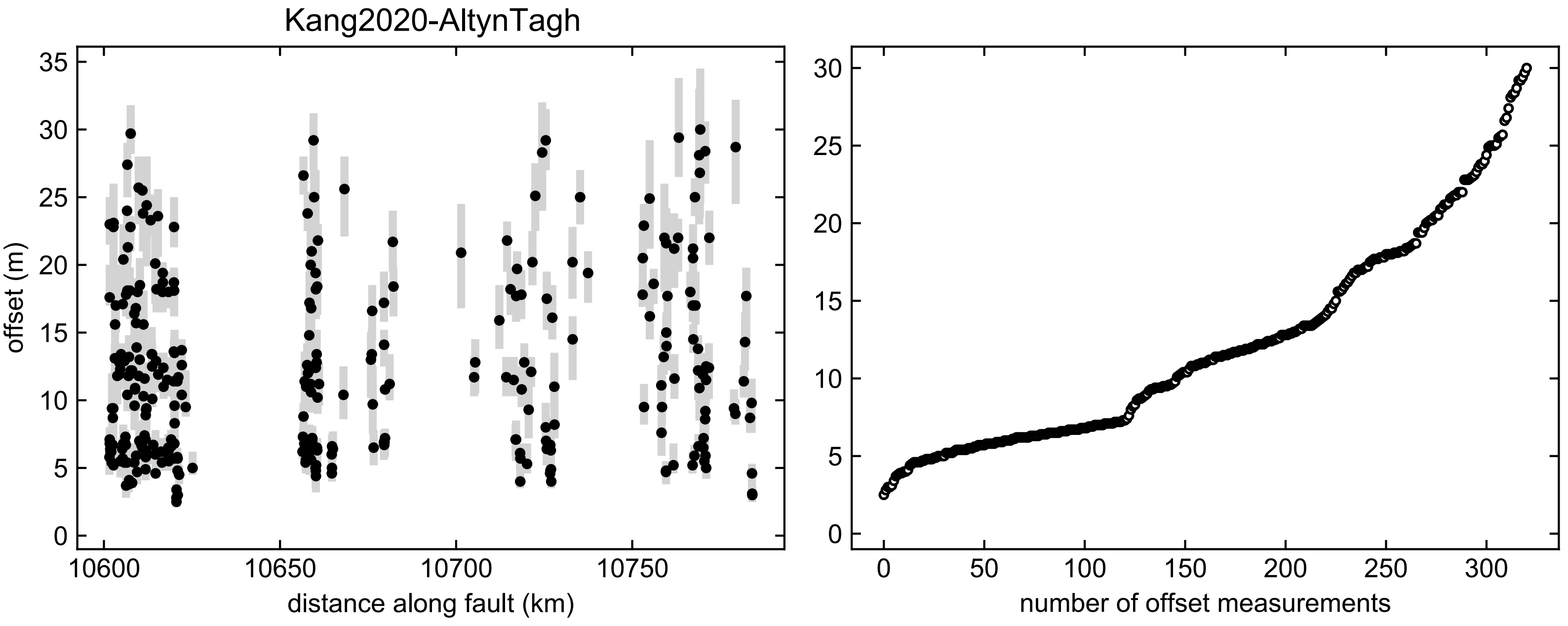
Kang2020-AltynTagh
offset (m)
distance along fault (km)
number of offset measurements

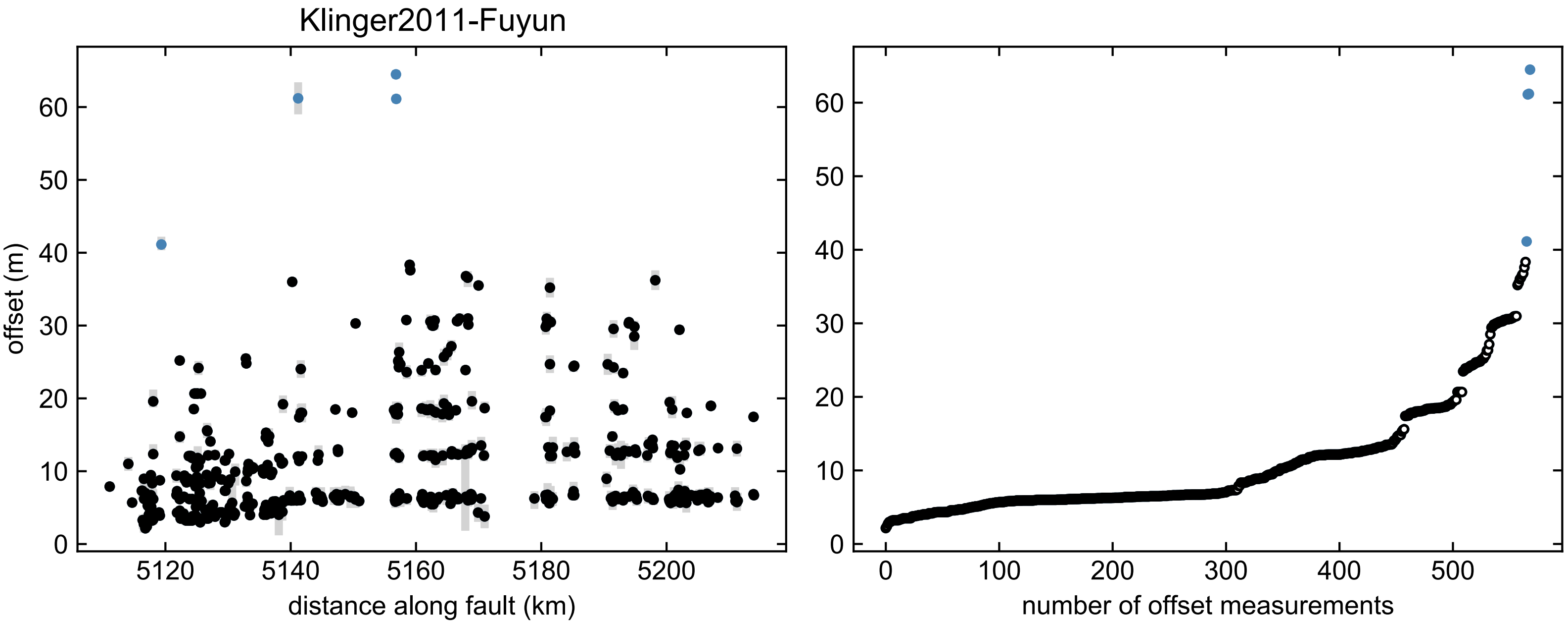

Klinger2011-Fuyun
offset (m)
0
10
20
30
40
50
60
5120
5140
5160
5180
5200
distance along fault (km)
0
10
20
30
40
50
60
0
100
200
300
400
500
number of offset measurements

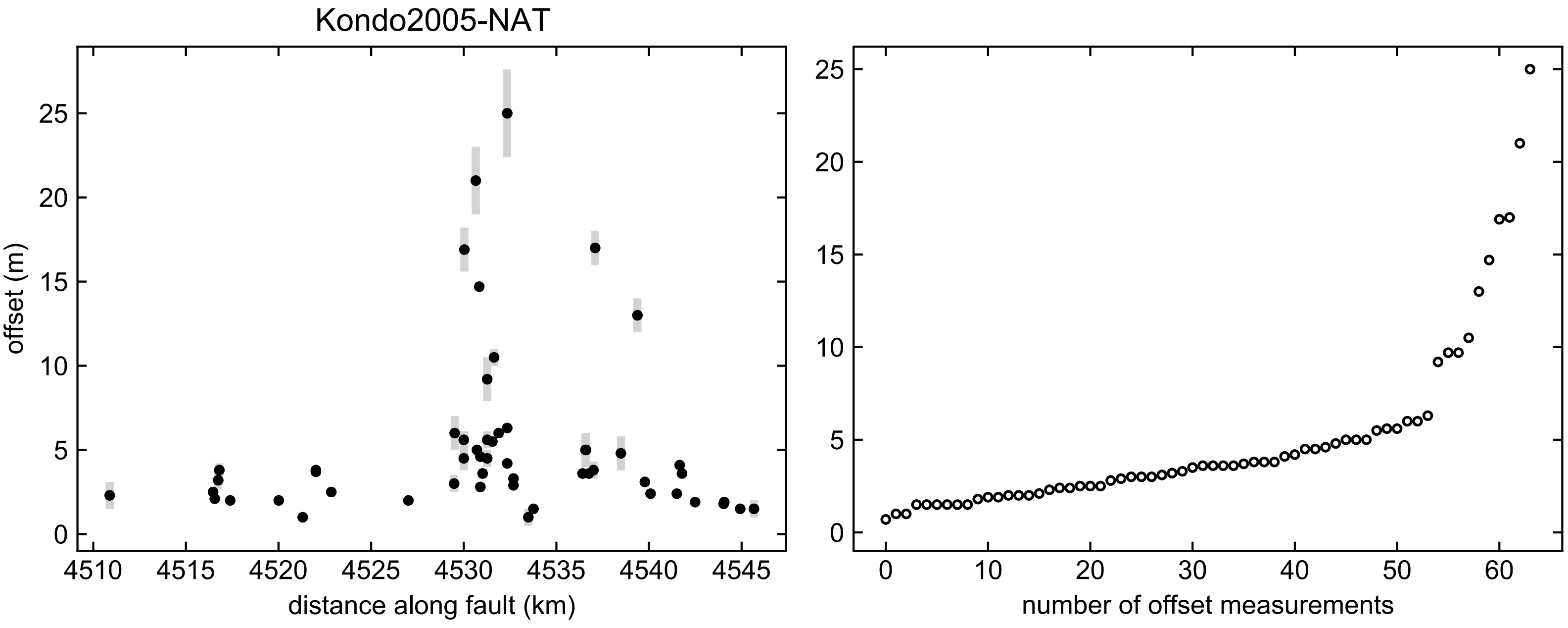

Kondo2005-NAT
offset (m)
0
5
10
15
20
25
4510
4515
4520
4525
4530
4535
4540
4545
distance along fault (km)
0
5
10
15
20
25
0
10
20
30
40
50
60
number of offset measurements

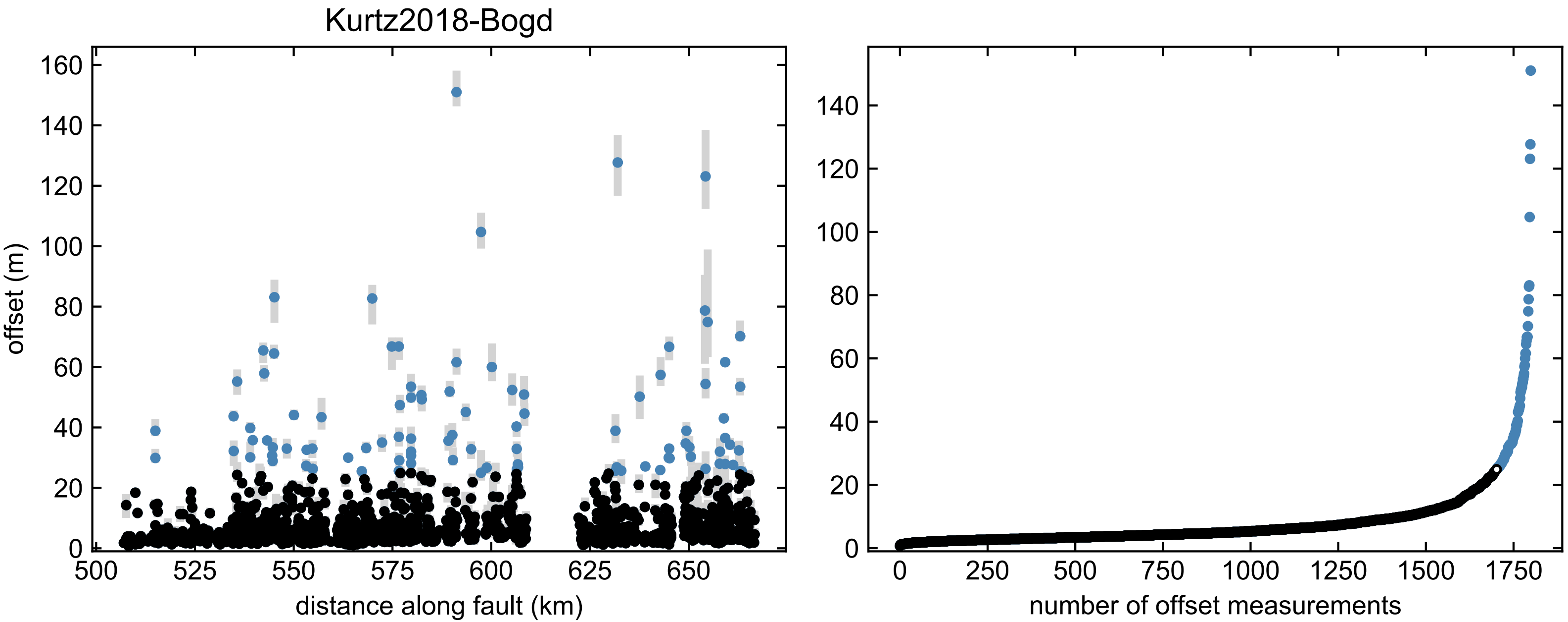

Kurtz2018-Bogd
offset (m)
distance along fault (km)
number of offset measurements

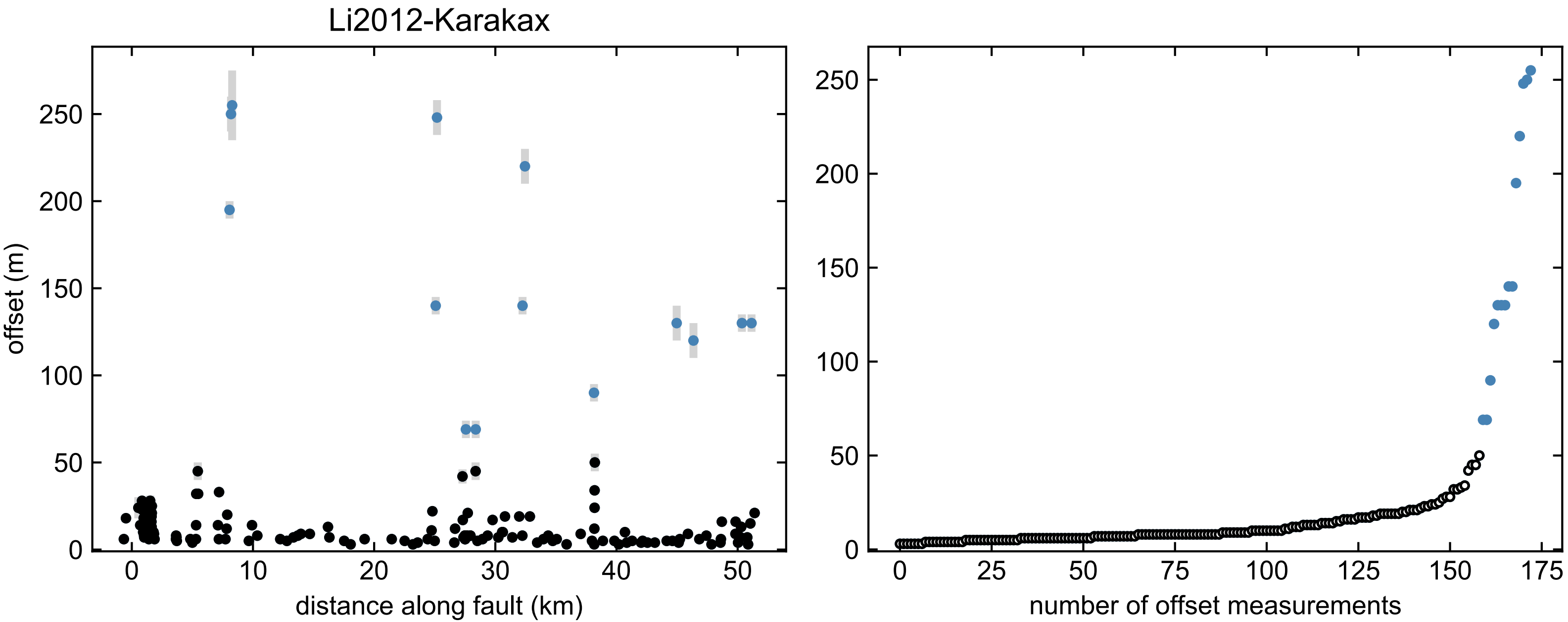
Li2012-Karakax
offset (m)
distance along fault (km)
number of offset measurements
0
50
100
150
200
250
0
10
20
30
40
50
0
25
50
75
100
125
150
175

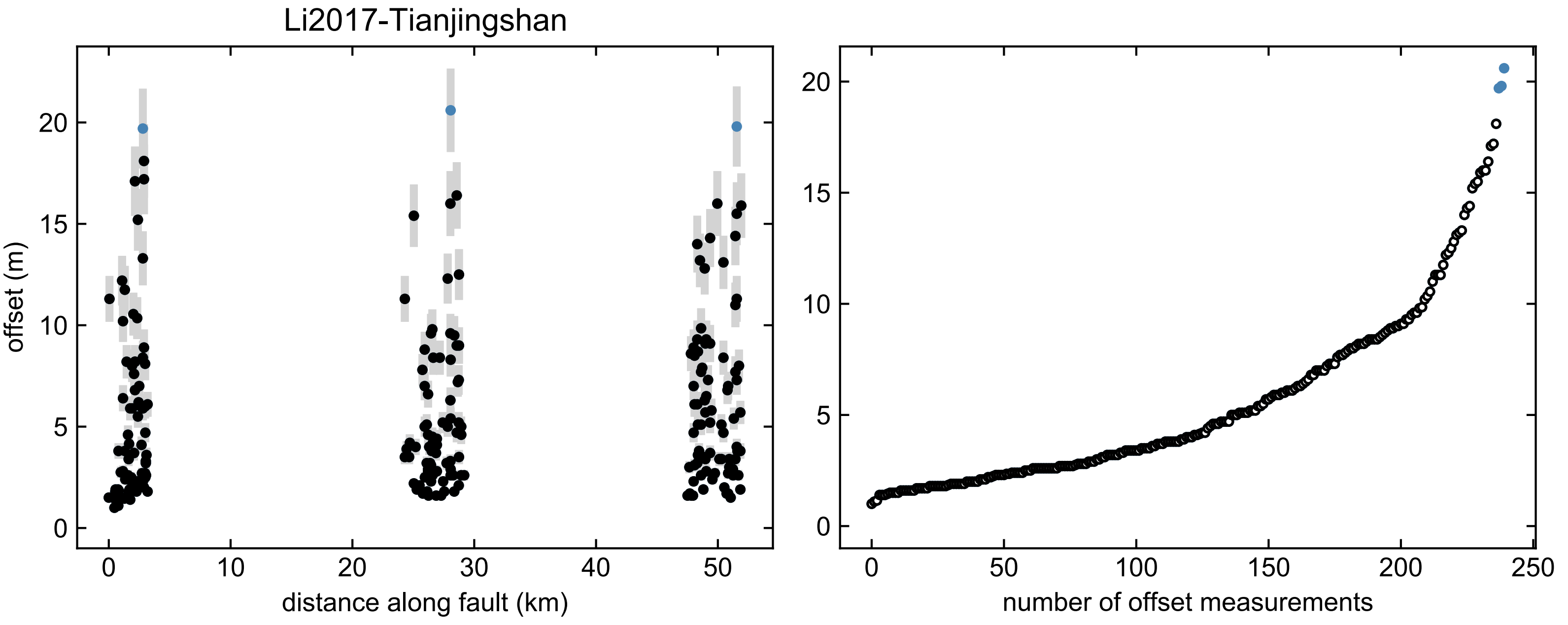

Li2017-Tianjingshan
offset (m)
distance along fault (km)
number of offset measurements
0
5
10
15
20
0
10
20
30
40
50
0
50
100
150
200
250

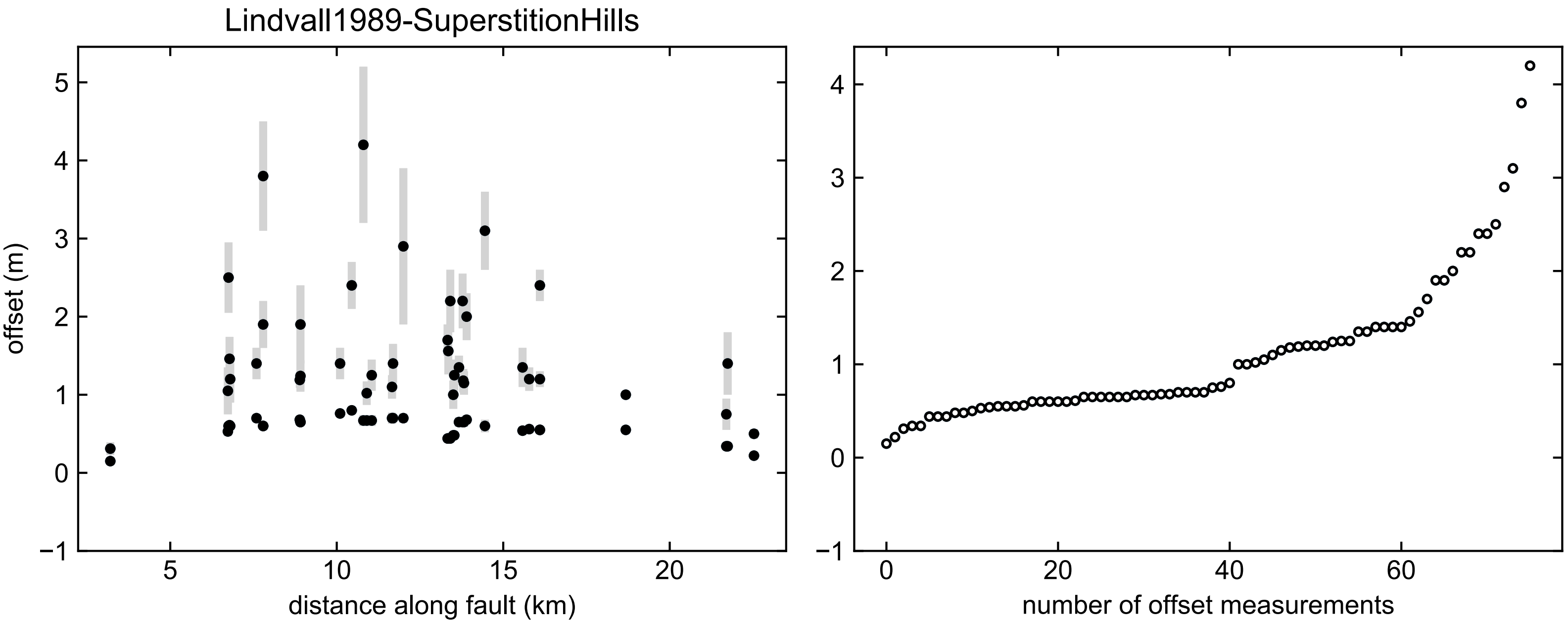

Lindvall1989-SuperstitionHills
offset (m)
distance along fault (km)
number of offset measurements

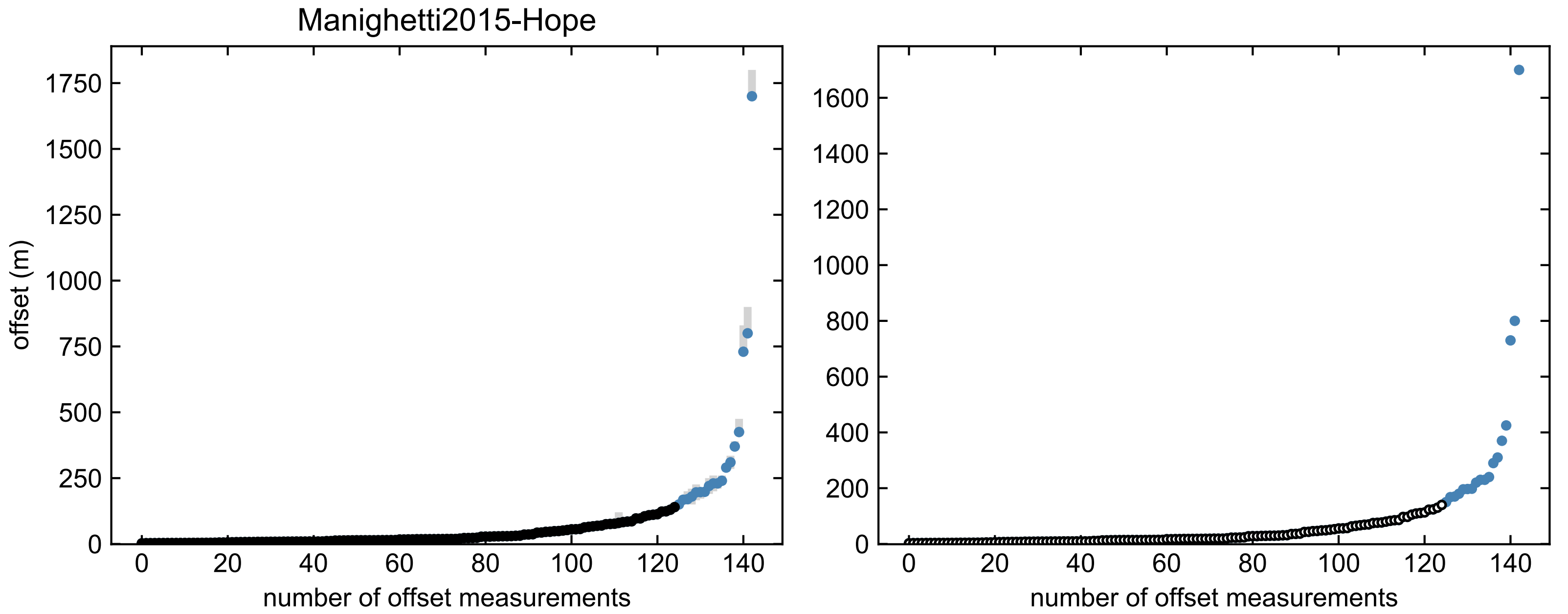

Manighetti2015-Hope
offset (m)
0
250
500
750
1000
1250
1500
1750
0
20
40
60
80
100
120
140
number of offset measurements
0
200
400
600
800
1000
1200
1400
1600
0
20
40
60
80
100
120
140
number of offset measurements

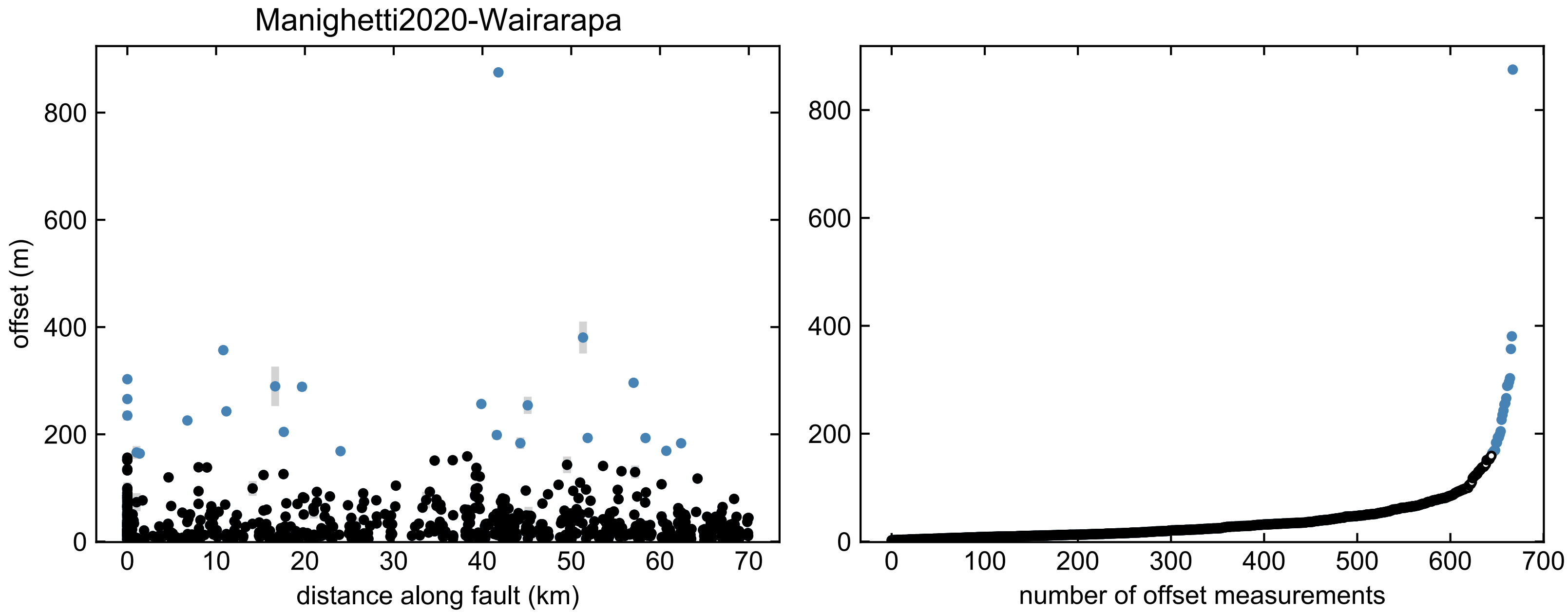
Manighetti2020-Wairarapa
offset (m)
0
200
400
600
800
0
10
20
30
40
50
60
70
distance along fault (km)
0
200
400
600
800
0
100
200
300
400
500
600
700
number of offset measurements

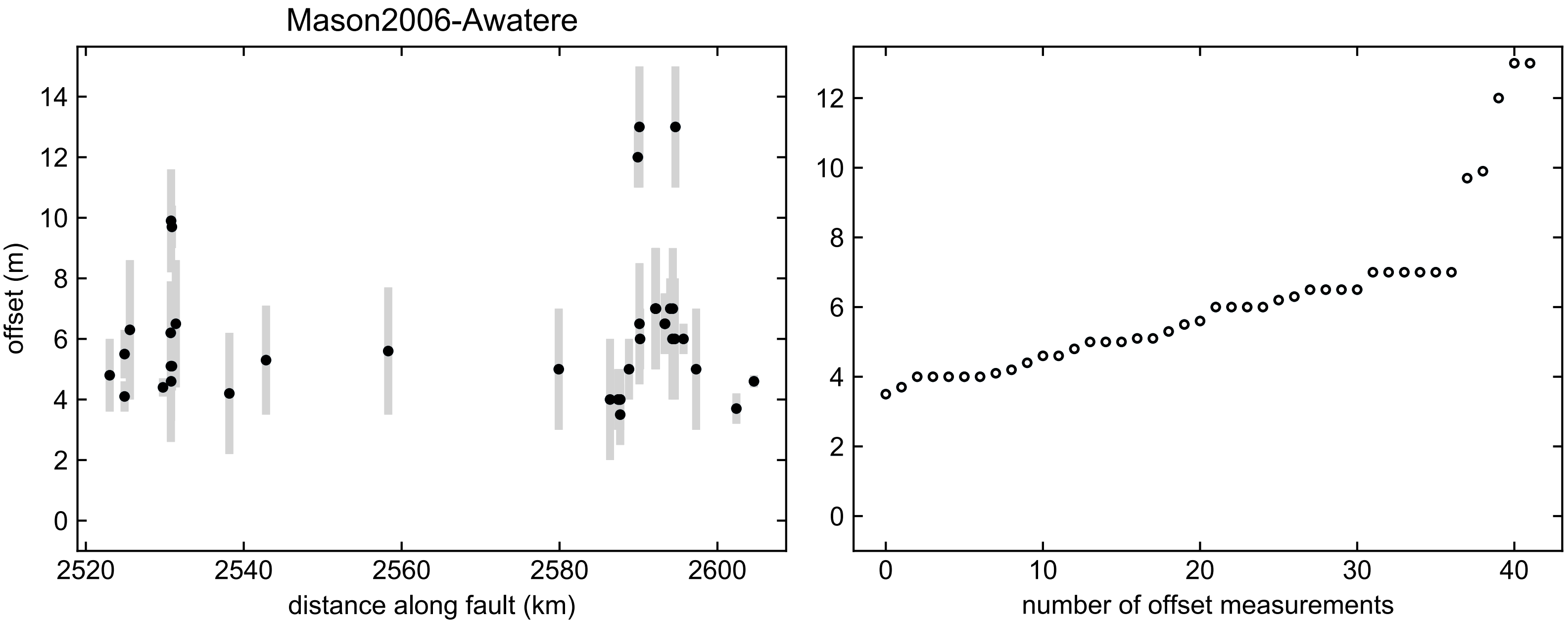

Mason2006-Awatere
offset (m)
distance along fault (km)
number of offset measurements

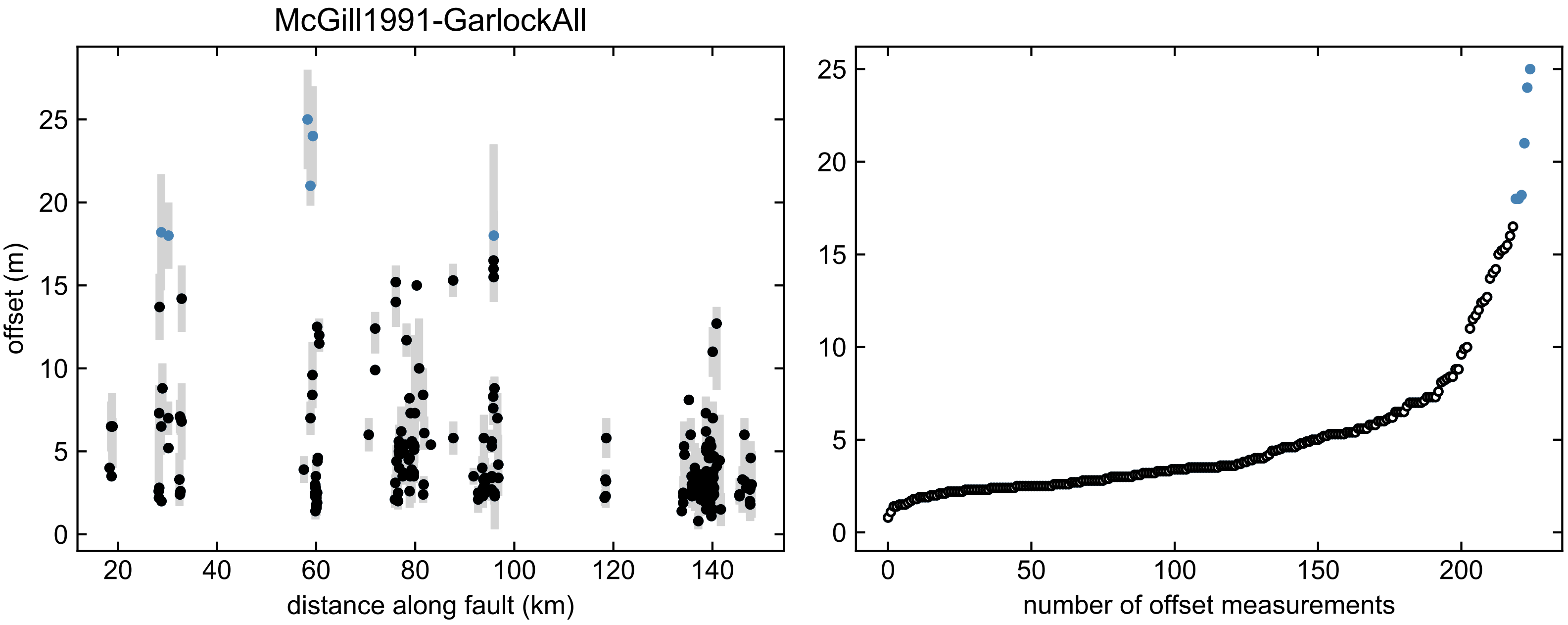
McGill1991-GarlockAll
offset (m)
distance along fault (km)
number of offset measurements
0
5
10
15
20
25
20
40
60
80
100
120
140
0
50
100
150
200

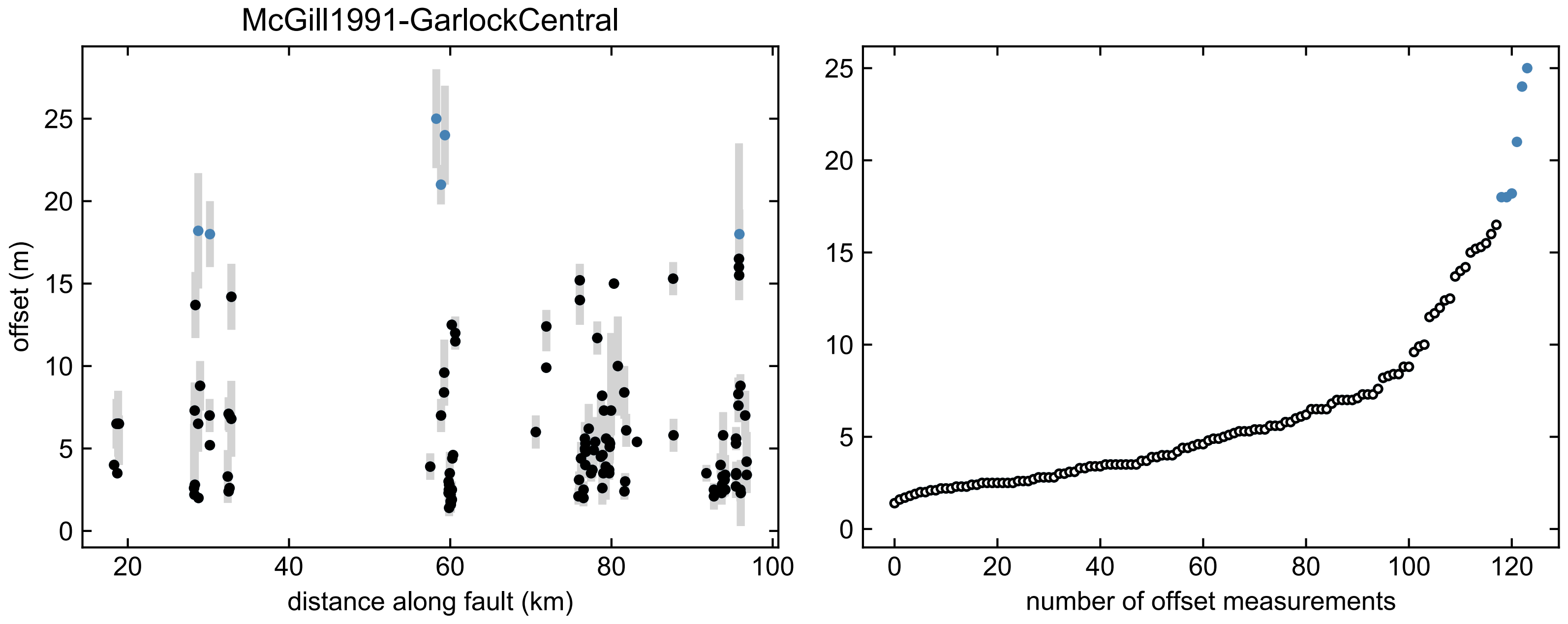
McGill1991-GarlockCentral
offset (m)
distance along fault (km)
number of offset measurements

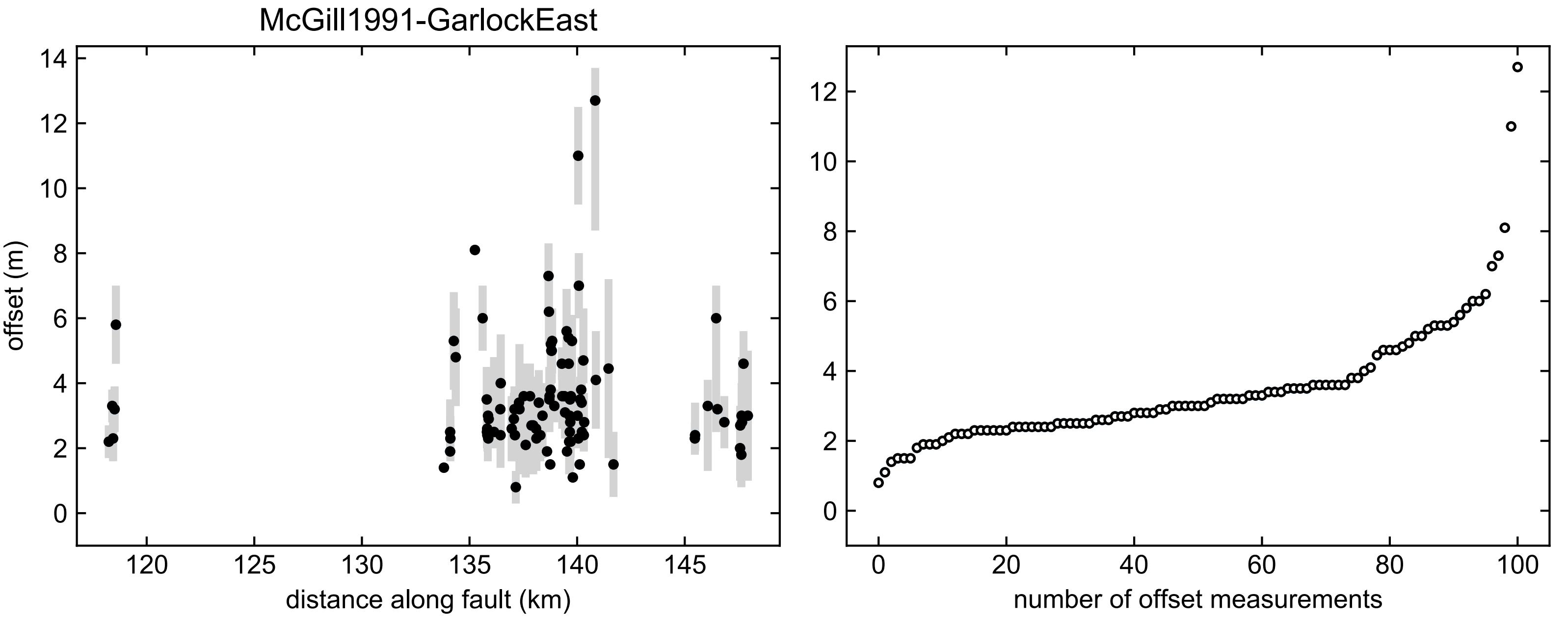
McGill1991-GarlockEast
offset (m)
distance along fault (km)
number of offset measurements
0
2
4
6
8
10
12
14
120
125
130
135
140
145
20
40
60
80
100

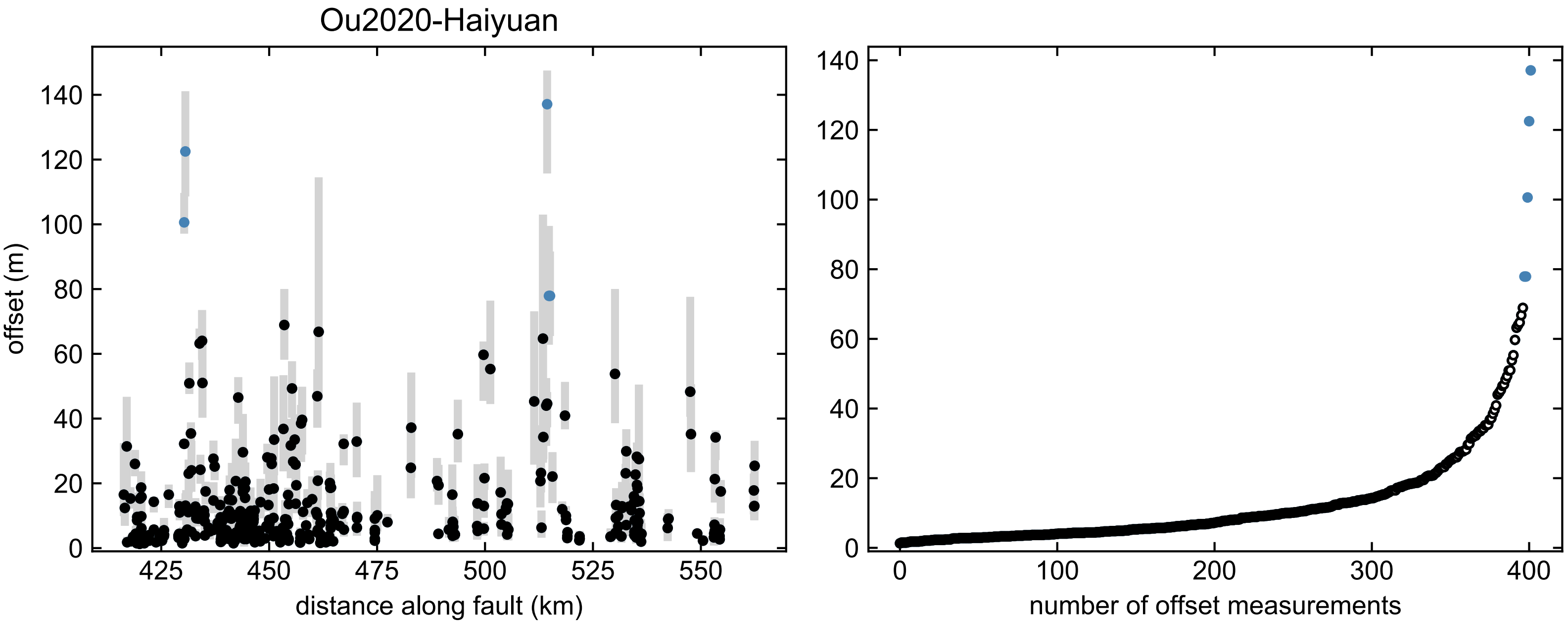

Ou2020-Haiyuan
offset (m)
0
20
40
60
80
100
120
140
425
450
475
500
525
550
distance along fault (km)
0
20
40
60
80
100
120
140
0
100
200
300
400
number of offset measurements

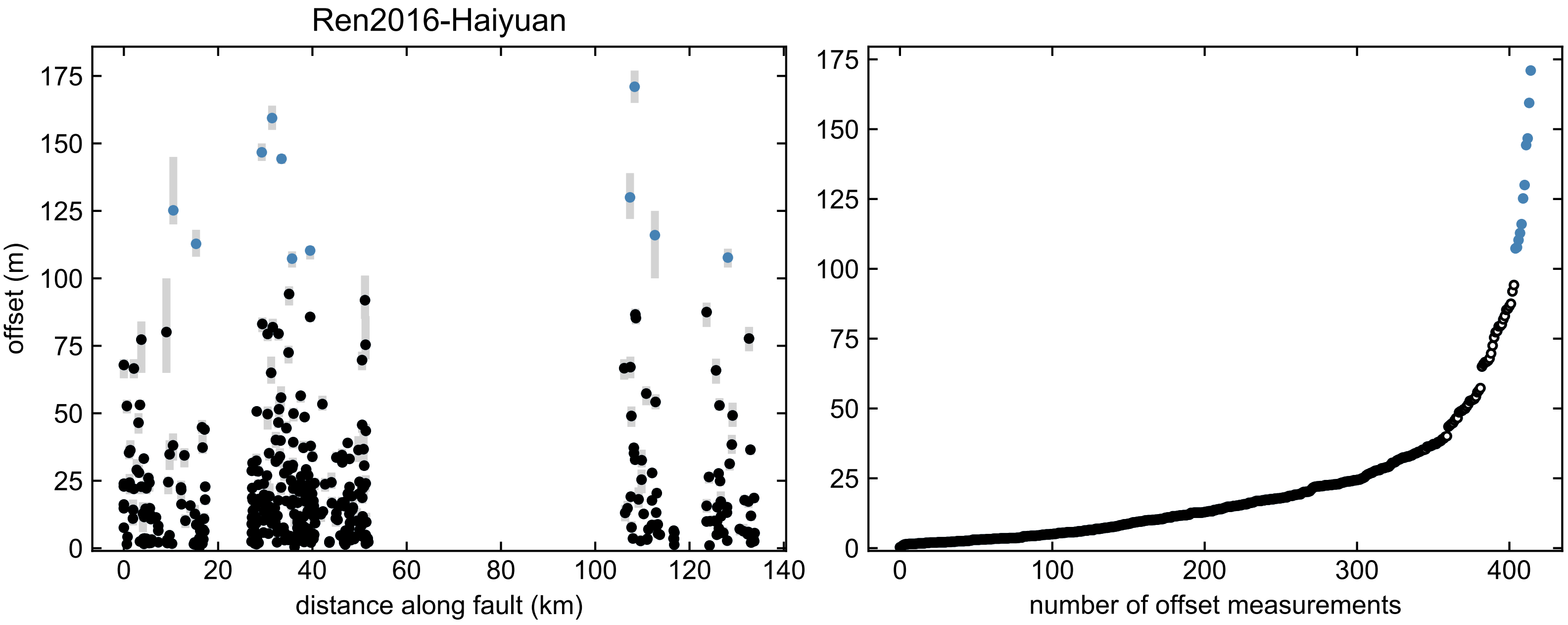

Ren2016-Haiyuan
offset (m)
175
150
125
100
75
50
25
0
0
20
40
60
80
100
120
140
distance along fault (km)
175
150
125
100
75
50
25
0
0
100
200
300
400
number of offset measurements

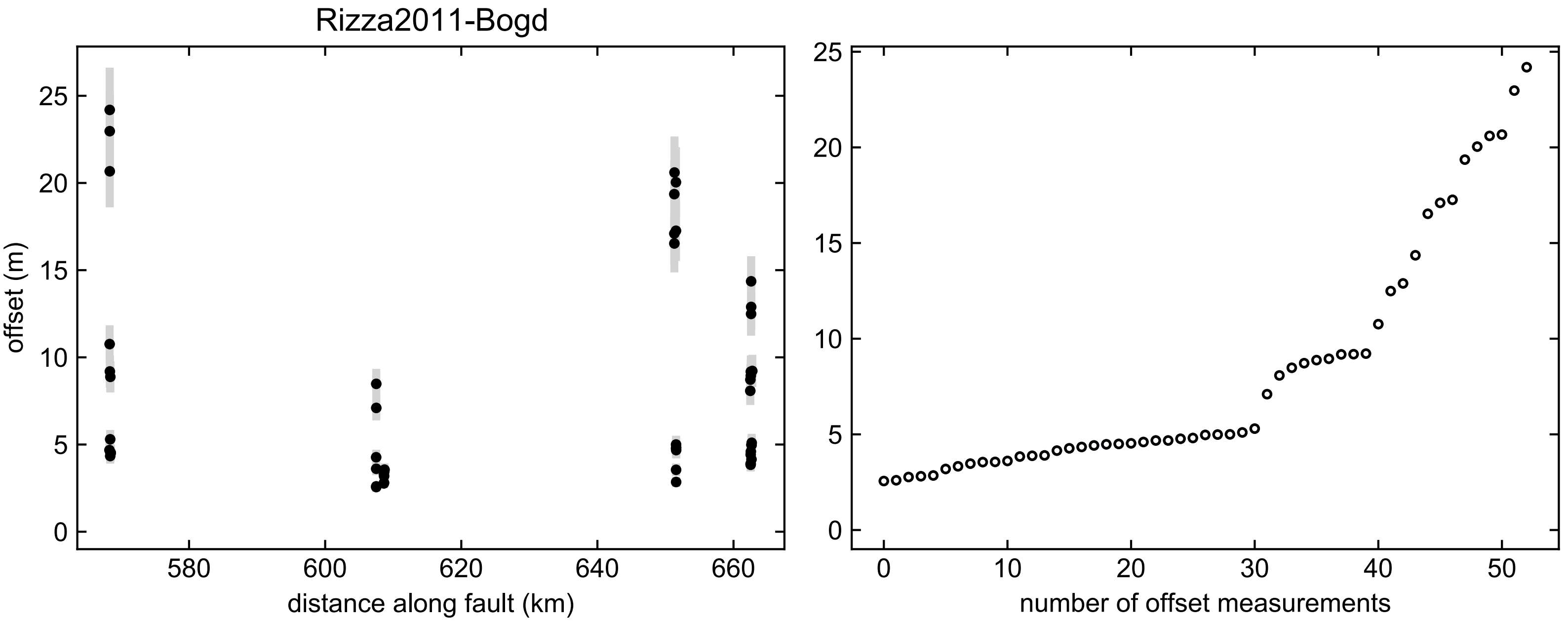

Rizza2011-Bogd
offset (m)
0
5
10
15
20
25
580
600
620
640
660
distance along fault (km)
0
5
10
15
20
25
0
10
20
30
40
50
number of offset measurements

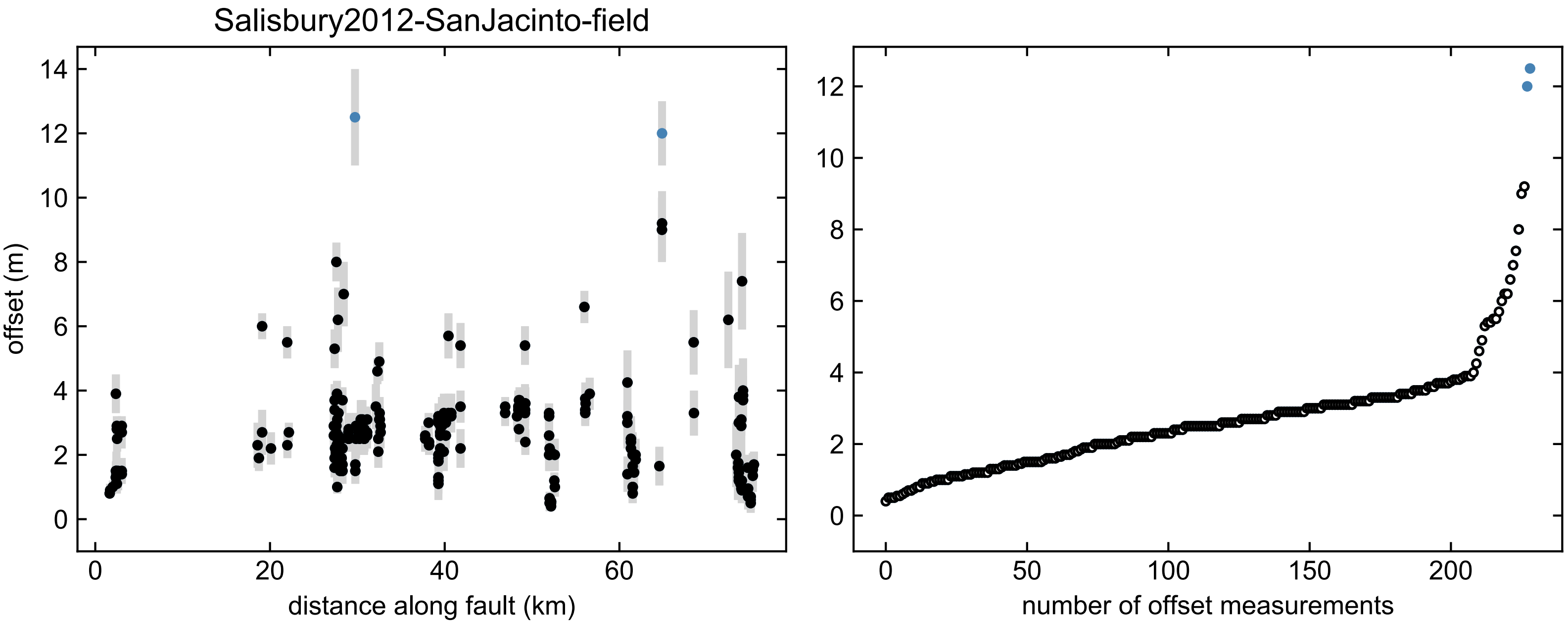

Salisbury2012-SanJacinto-field
offset (m)
distance along fault (km)
number of offset measurements
0
2
4
6
8
10
12
14
20
40
60
50
100
150
200

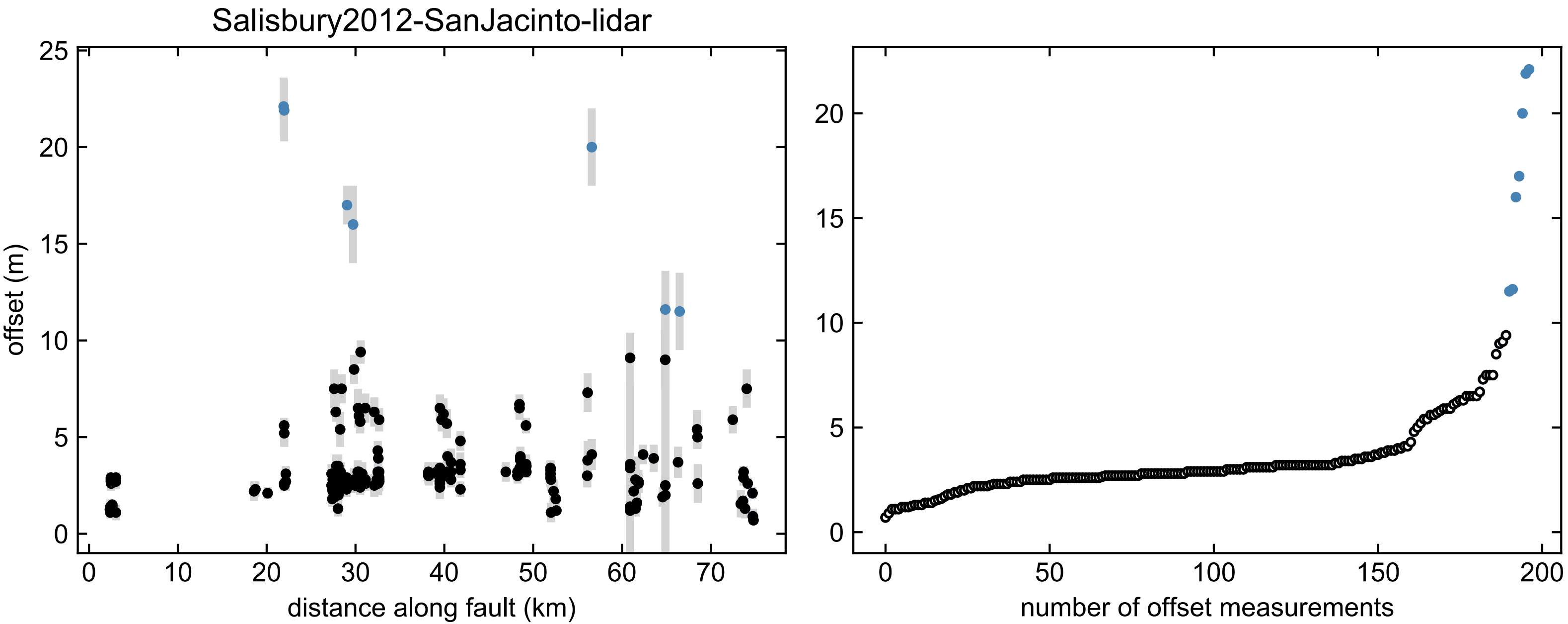

Salisbury2012-SanJacinto-lidar
offset (m)
25
20
15
10
5
0
0
10
20
30
40
50
60
70
distance along fault (km)
20
15
10
5
0
0
50
100
150
200
number of offset measurements

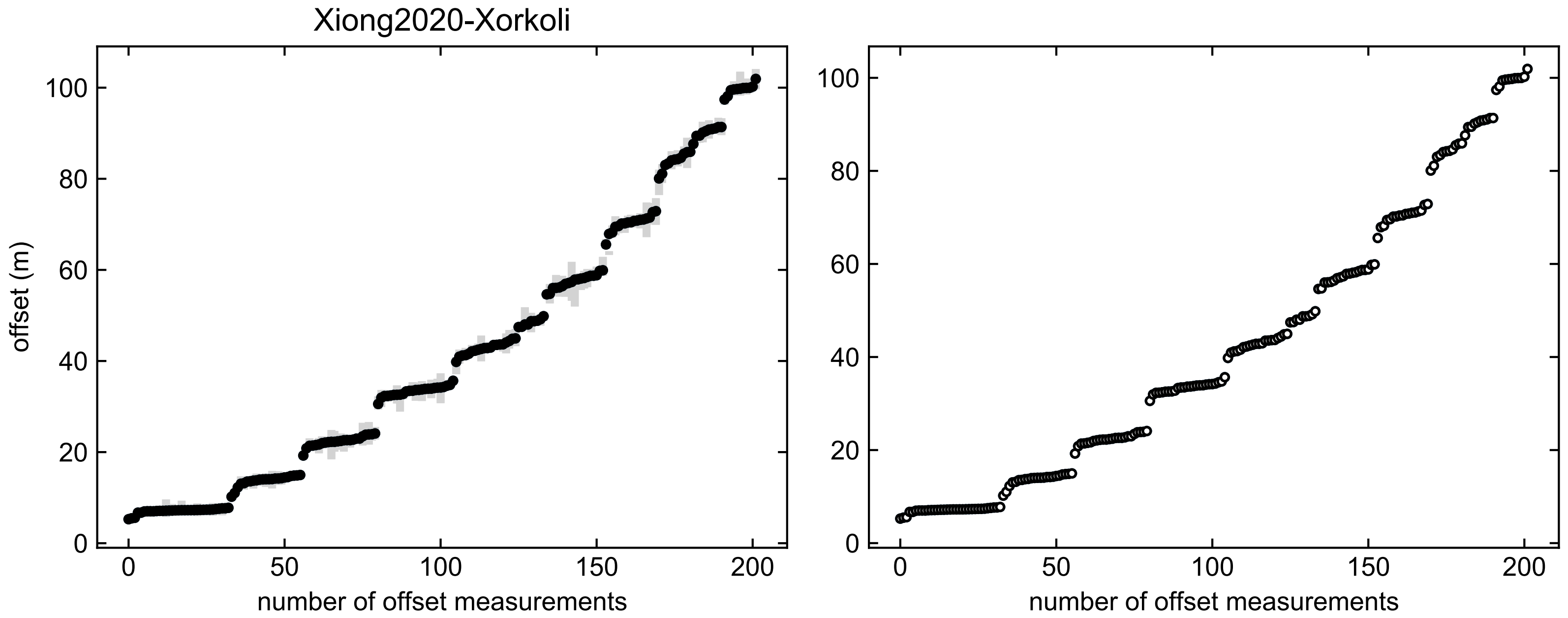
Xiong2020-Xorkoli
offset (m)
number of offset measurements
number of offset measurements
0
20
40
60
80
100
0
50
100
150
200

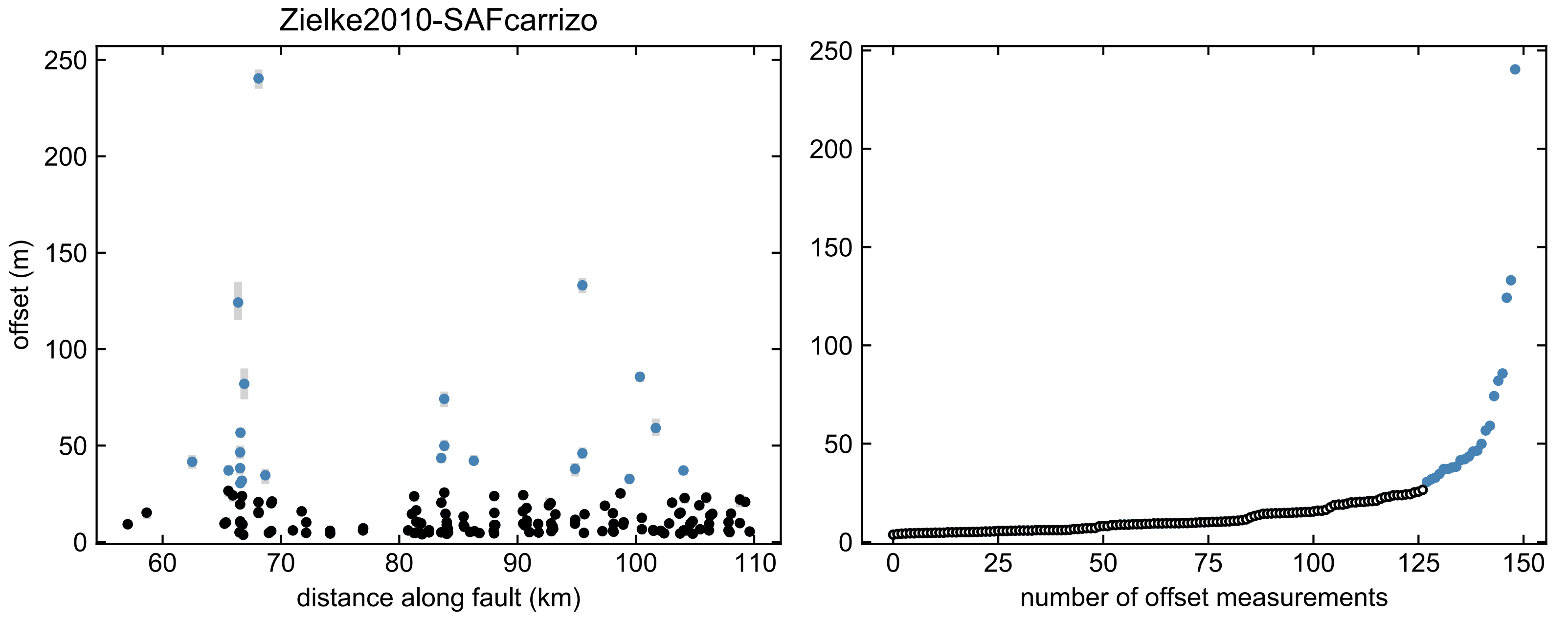
Zielke2010-SAFcarrizo
offset (m)
250
200
150
100
50
0
60
70
80
90
100
110
distance along fault (km)
250
200
150
100
50
0
0
25
50
75
100
125
150
number of offset measurements

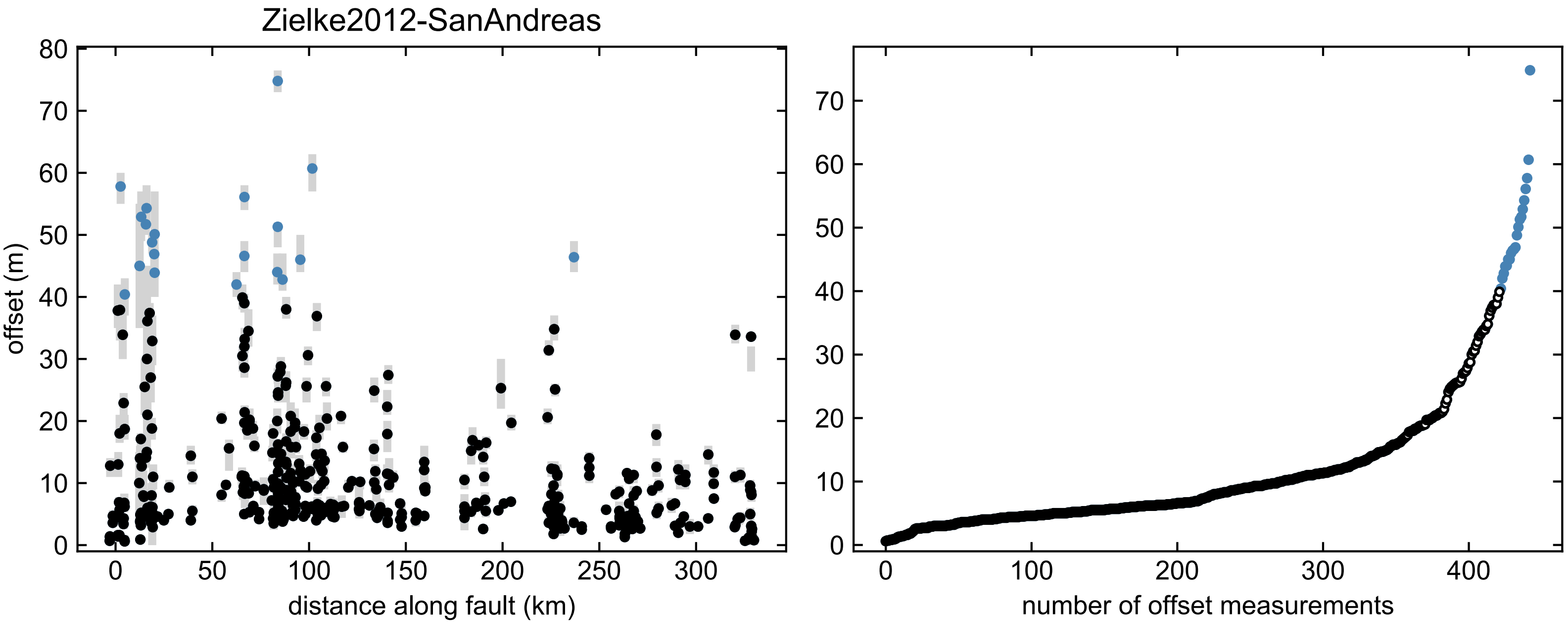

Zielke2012-SanAndreas
offset (m)
distance along fault (km)
number of offset measurements
0
10
20
30
40
50
60
70
80
0
50
100
150
200
250
300
400

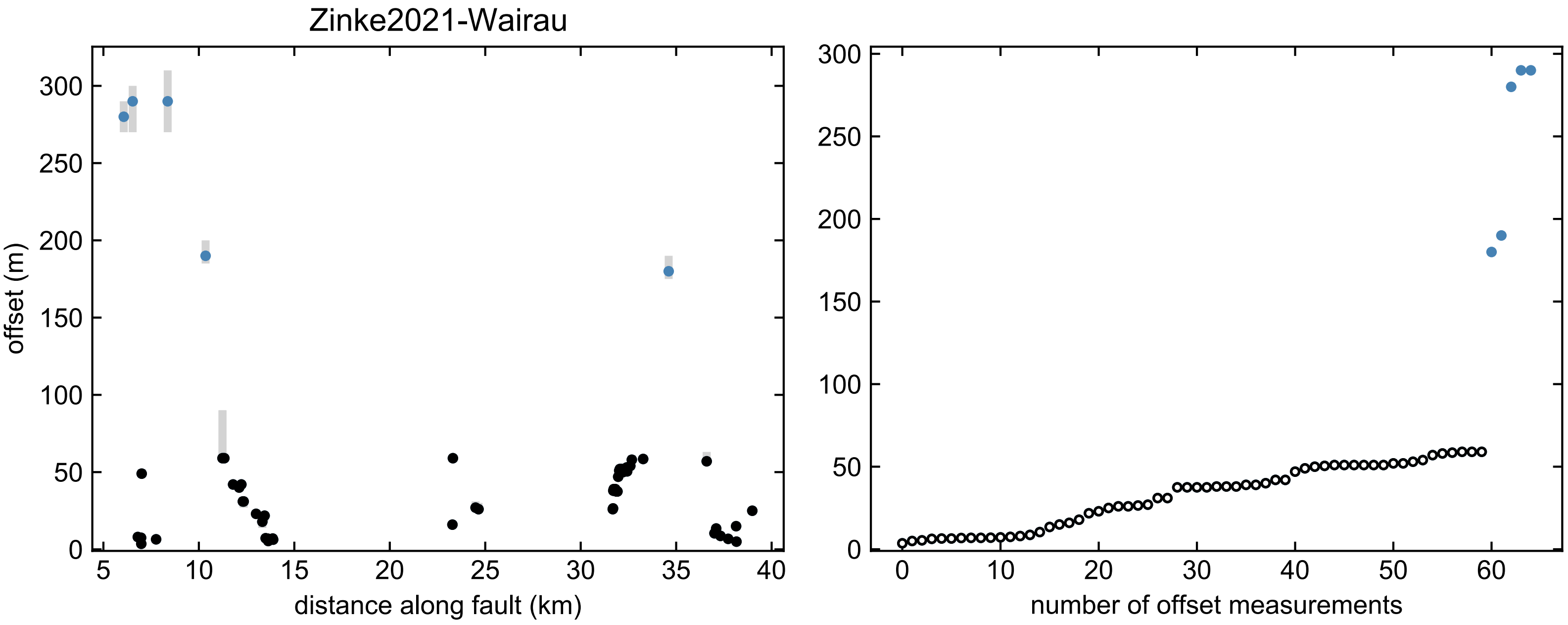

Zinke2021-Wairau
offset (m)
distance along fault (km)
number of offset measurements

Plots of *b* value calculations for each dataset:

In the following plots, offset measurement (m) is on the x-axis for all panels. The left panel shows offset measurements with uncertainty ranges plotted by distance along the fault. If distance along the fault is not provided, then offsets are plotted from smallest to largest. The second panel shows offset measurements with uncertainty ranges plotted from largest to smallest with the best fitting exponential decay curve fit to all offset measurements. The third panel is a cumulative offset probability density (COPD) curve with automatically selected peaks (red stars) and the best fitting exponential decay curve fit to the COPD peaks. The final (right) panel is a histogram of the offset measurements with the best fitting exponential decay curve fit to bin midpoints (red circles). The fit parameters from equation 1, a and b, are shown in the third through fifth panels.

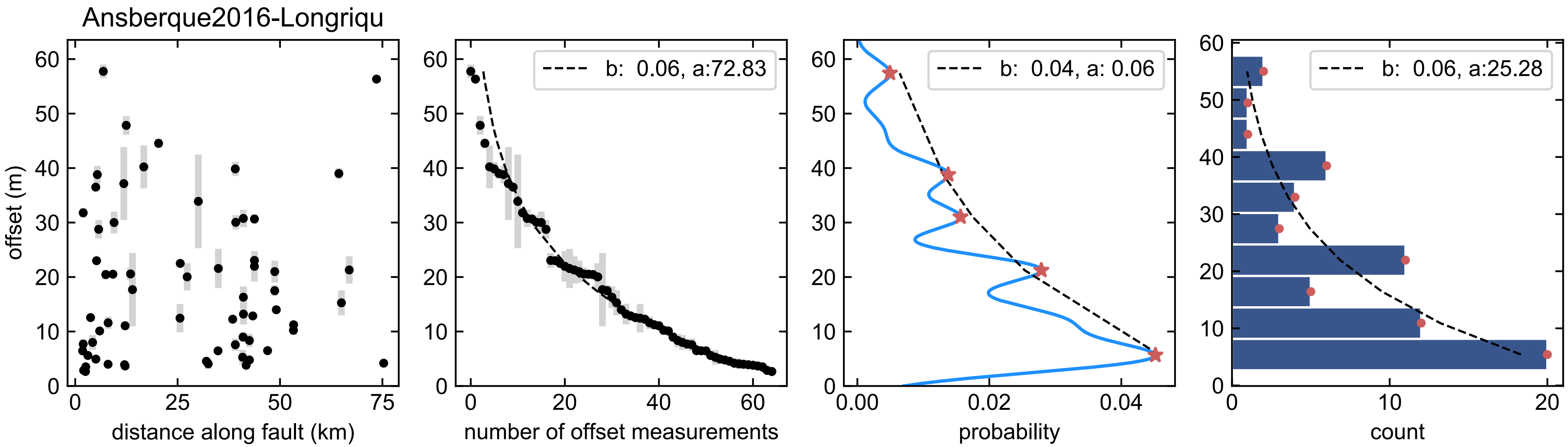
Ansberque2016-Longriqu
offset (m)
distance along fault (km)
number of offset measurements
b: 0.06, a:72.83
probability
b: 0.04, a: 0.06
count
b: 0.06, a:25.28

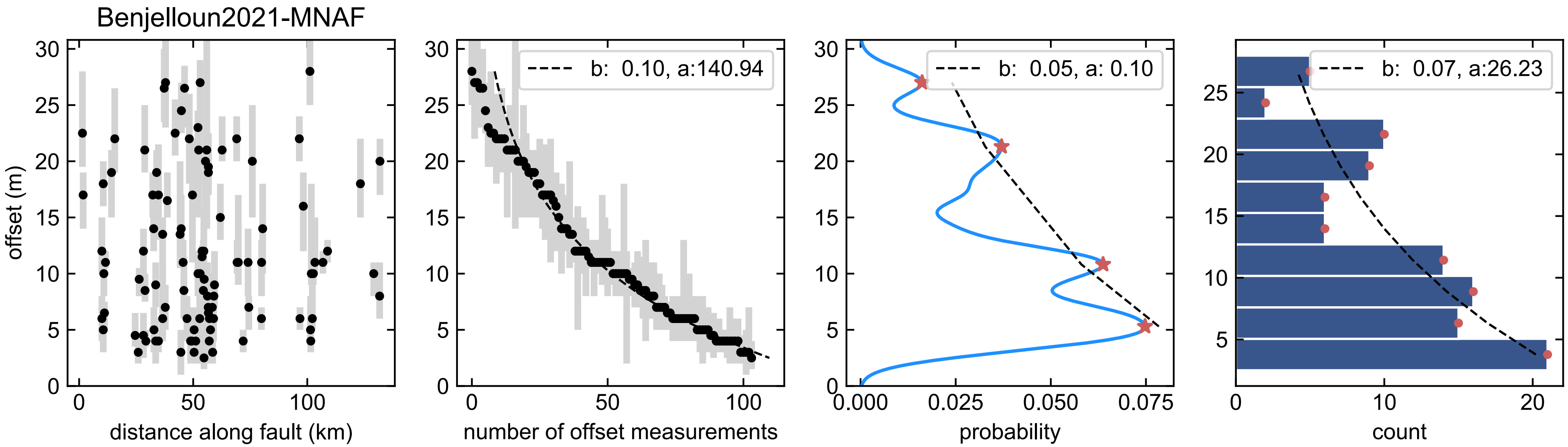

Benjelloun2021-MNAF
offset (m)
distance along fault (km)
b: 0.10, a:140.94
number of offset measurements
b: 0.05, a: 0.10
probability
b: 0.07, a:26.23
count

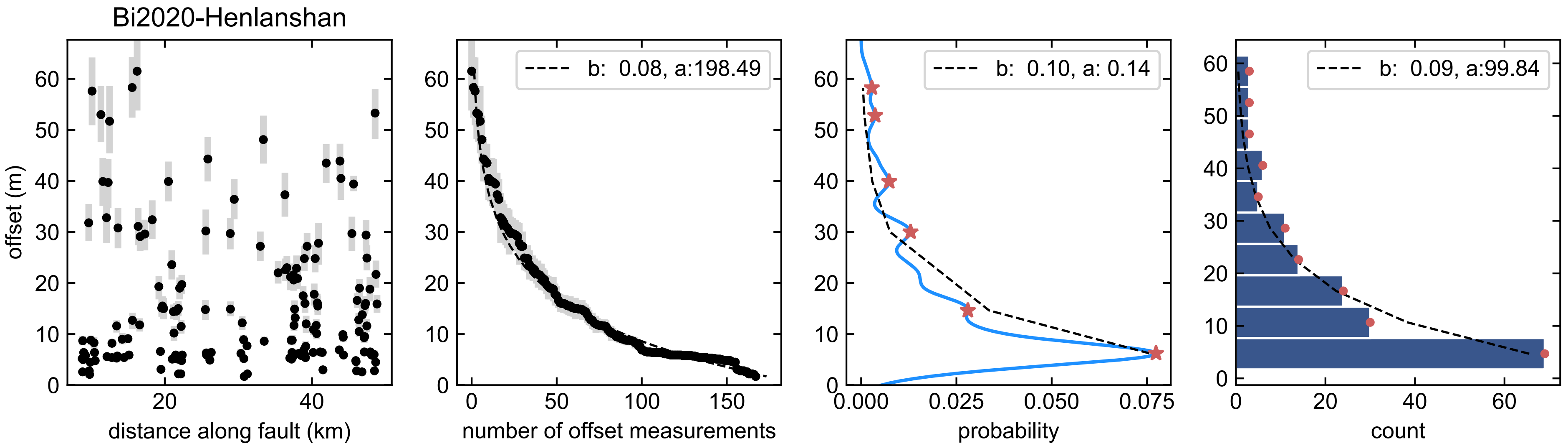
Bi2020-Henlanshan
offset (m)
distance along fault (km)
number of offset measurements
b: 0.08, a:198.49
probability
b: 0.10, a: 0.14
count
b: 0.09, a:99.84

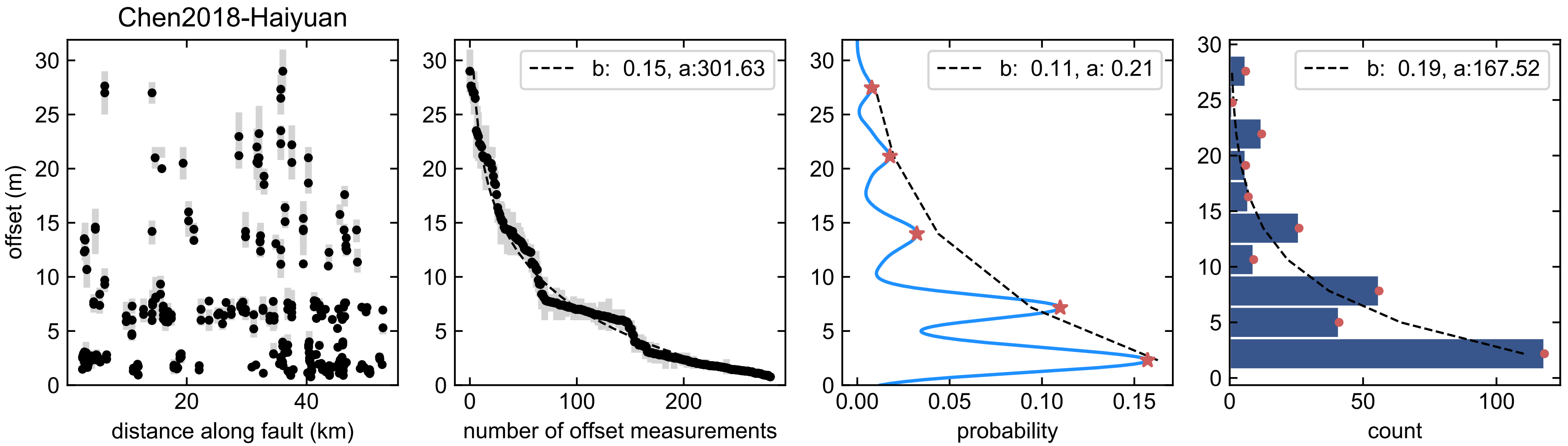
Chen2018-Haiyuan
offset (m)
distance along fault (km)
b: 0.15, a:301.63
number of offset measurements
b: 0.11, a: 0.21
probability
b: 0.19, a:167.52
count

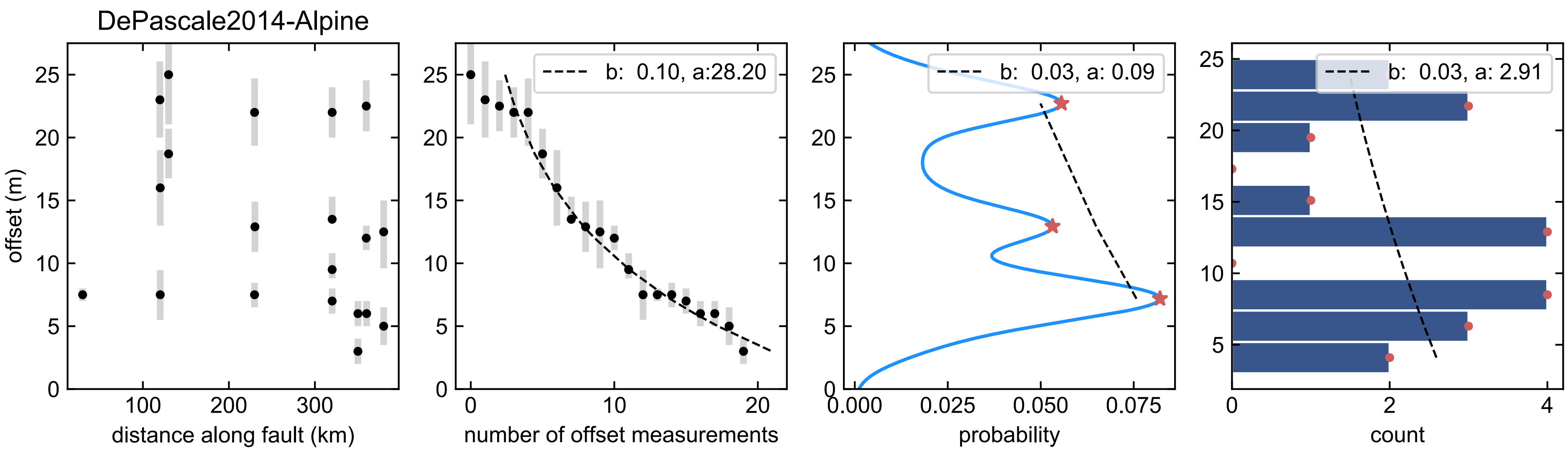
DePascale2014-Alpine
offset (m)
distance along fault (km)
b: 0.10, a:28.20
number of offset measurements
b: 0.03, a: 0.09
probability
b: 0.03, a: 2.91
count

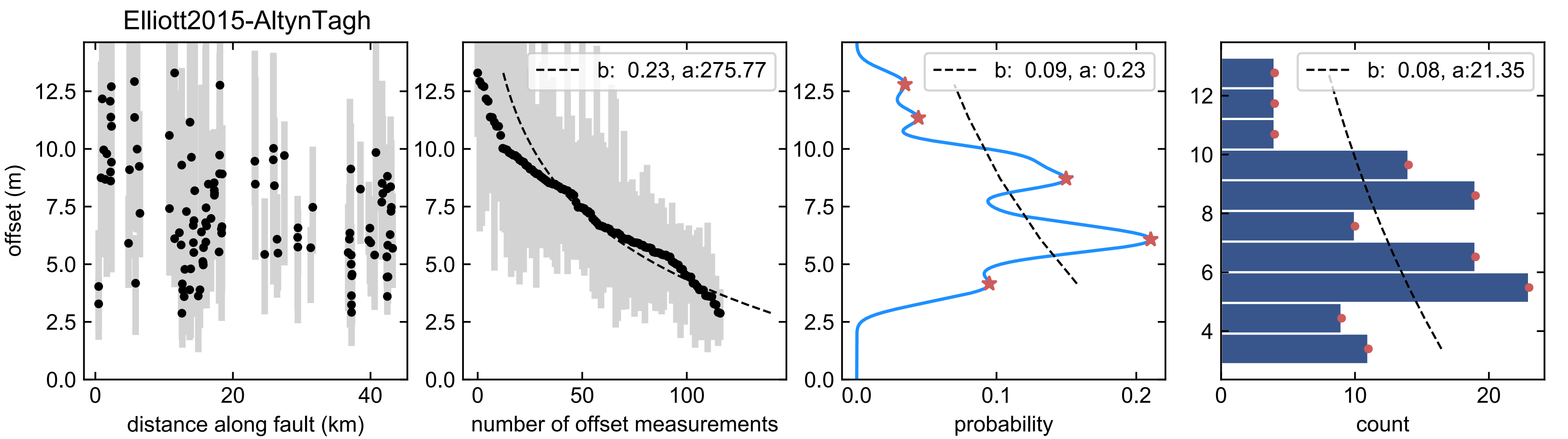

Elliott2015-AltynTagh
offset (m)
distance along fault (km)
number of offset measurements
b: 0.23, a:275.77
probability
b: 0.09, a: 0.23
count
b: 0.08, a:21.35

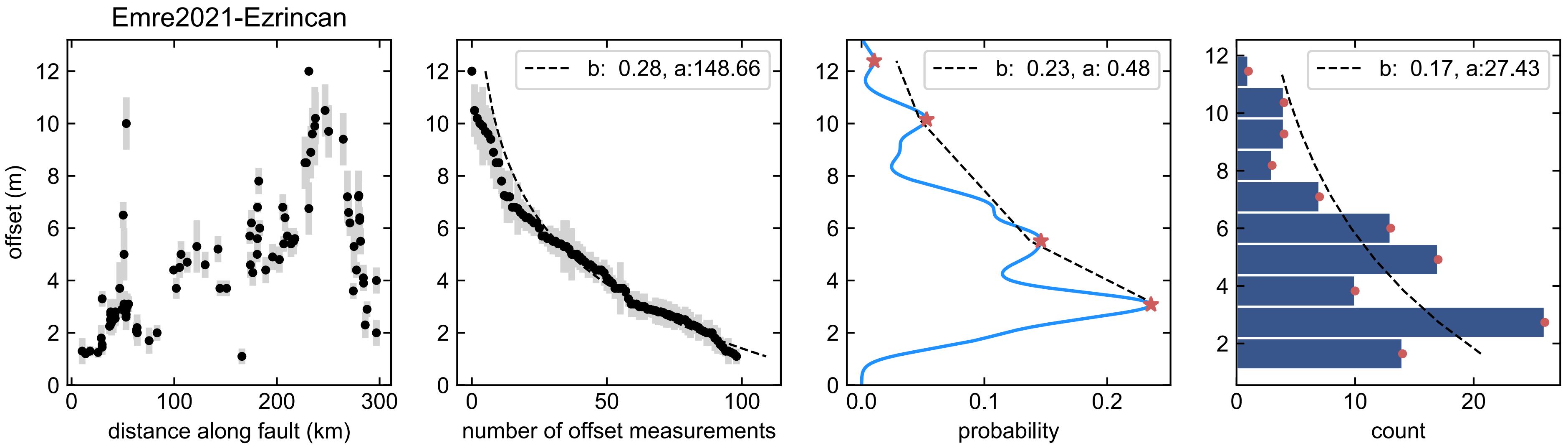

Emre2021-Ezrincan
offset (m)
distance along fault (km)
b: 0.28, a:148.66
number of offset measurements
b: 0.23, a: 0.48
probability
b: 0.17, a:27.43
count

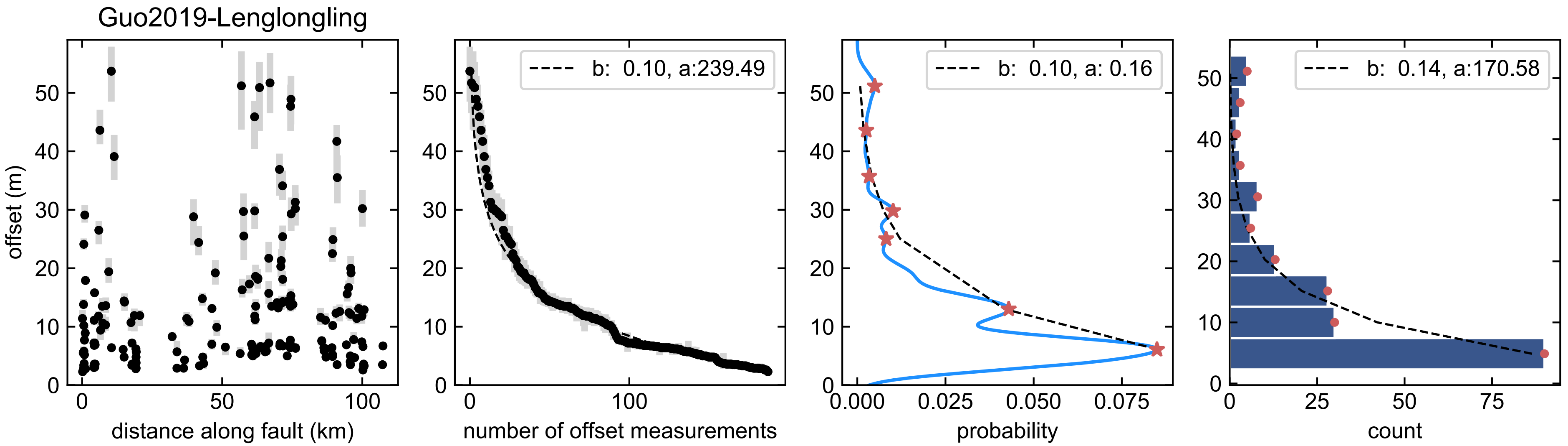

Guo2019-Lenglongling
offset (m)
distance along fault (km)
number of offset measurements
b: 0.10, a:239.49
probability
b: 0.10, a: 0.16
count
b: 0.14, a:170.58

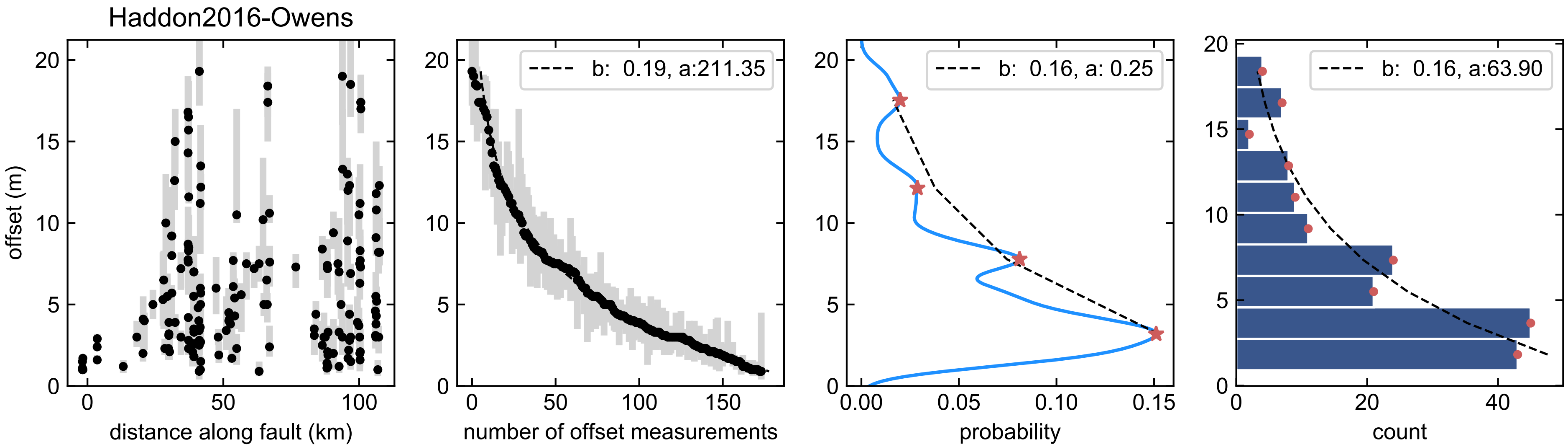

Haddon2016-Owens
offset (m)
distance along fault (km)
b: 0.19, a:211.35
number of offset measurements
b: 0.16, a: 0.25
probability
b: 0.16, a:63.90
count

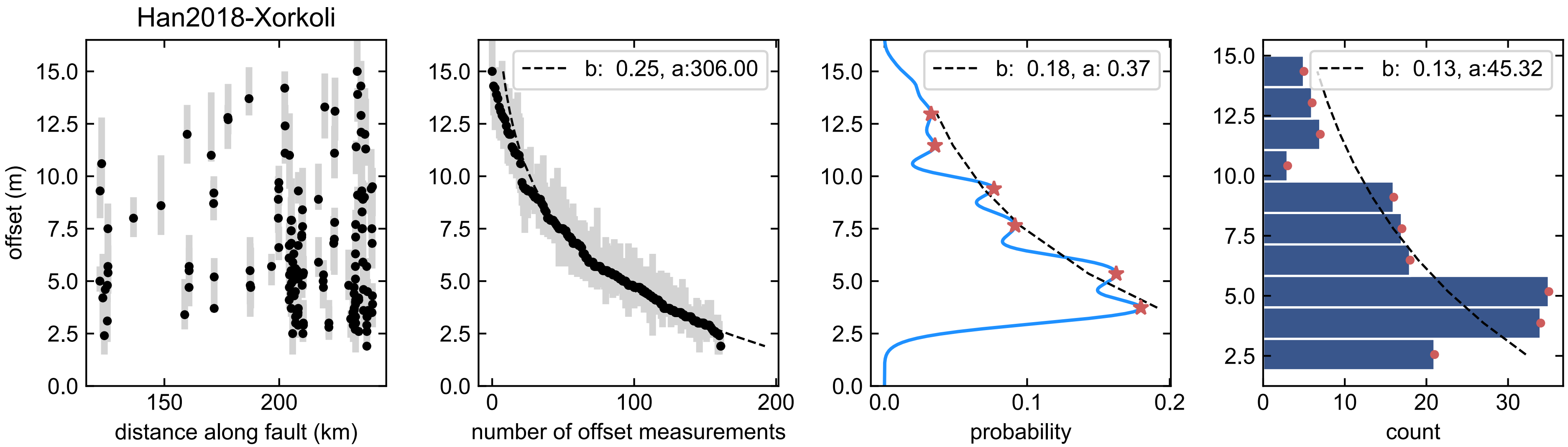

Han2018-Xorkoli
offset (m)
distance along fault (km)
number of offset measurements
b: 0.25, a:306.00
probability
b: 0.18, a: 0.37
count
b: 0.13, a:45.32

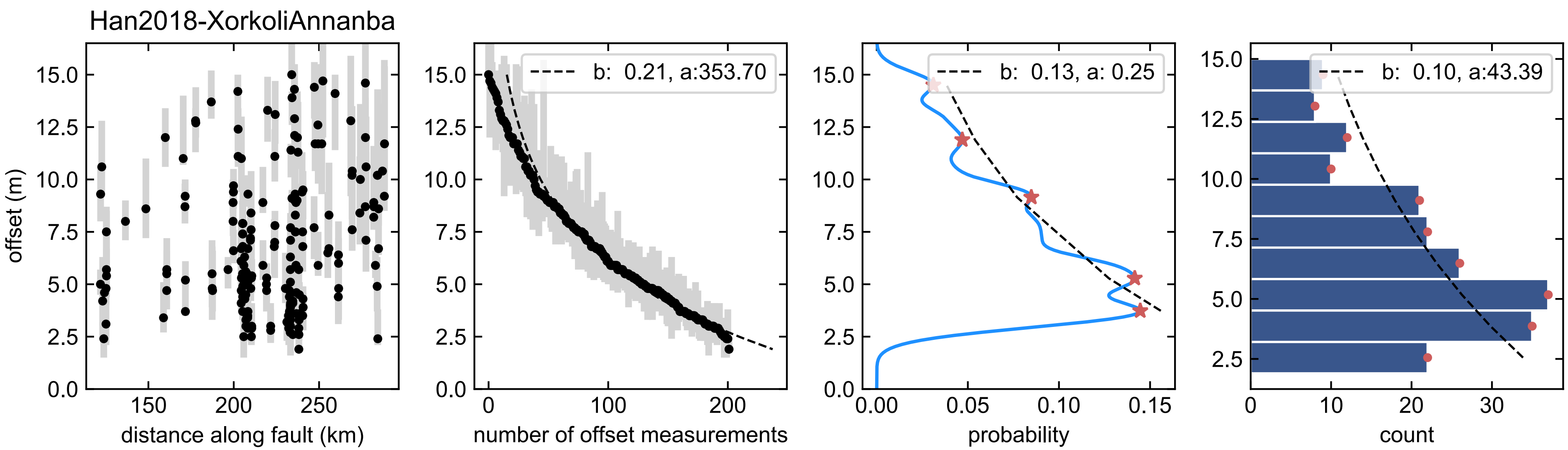

Han2018-XorkoliAnnanba
offset (m)
distance along fault (km)
b: 0.21, a:353.70
number of offset measurements
b: 0.13, a: 0.25
probability
b: 0.10, a:43.39
count

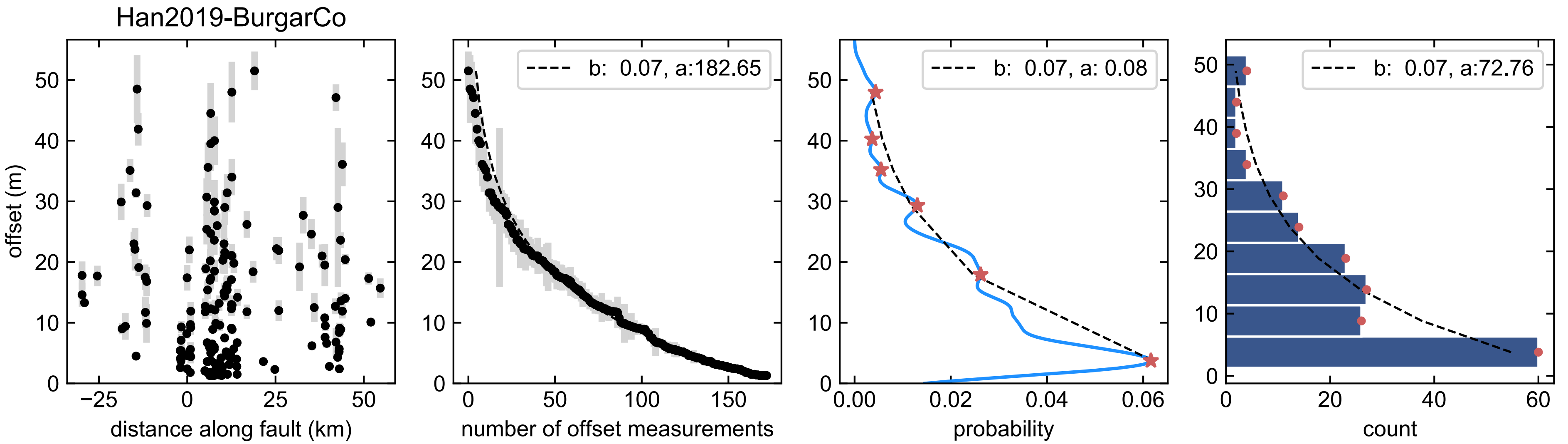
Han2019-BurgarCo
offset (m)
distance along fault (km)
number of offset measurements
b: 0.07, a:182.65
probability
b: 0.07, a: 0.08
count
b: 0.07, a:72.76

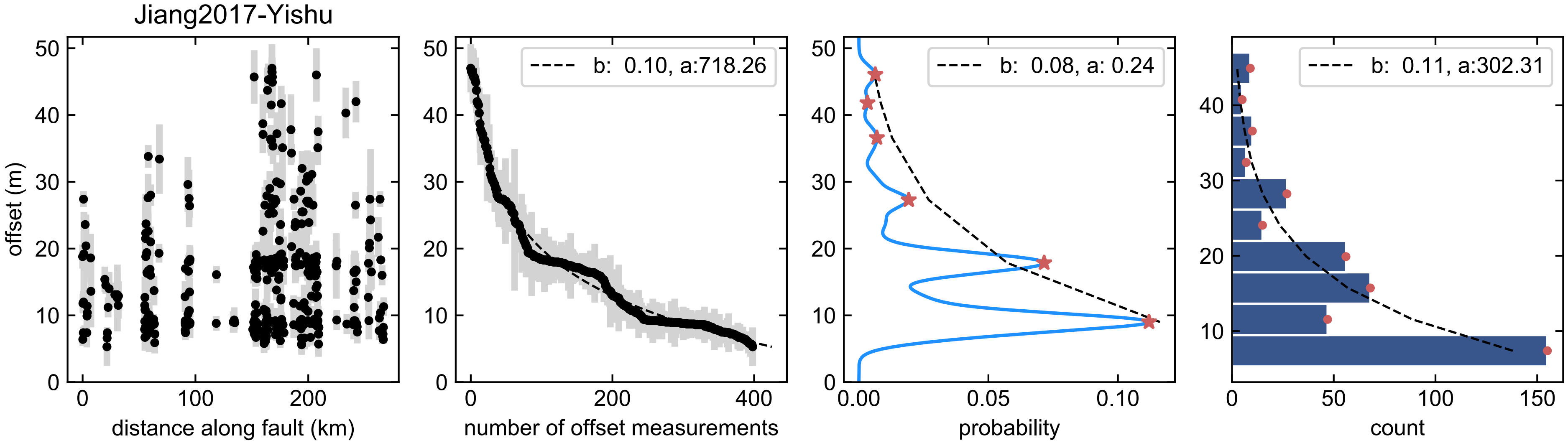

Jiang2017-Yishu
offset (m)
distance along fault (km)
number of offset measurements
b: 0.10, a:718.26
probability
b: 0.08, a: 0.24
count
b: 0.11, a:302.31

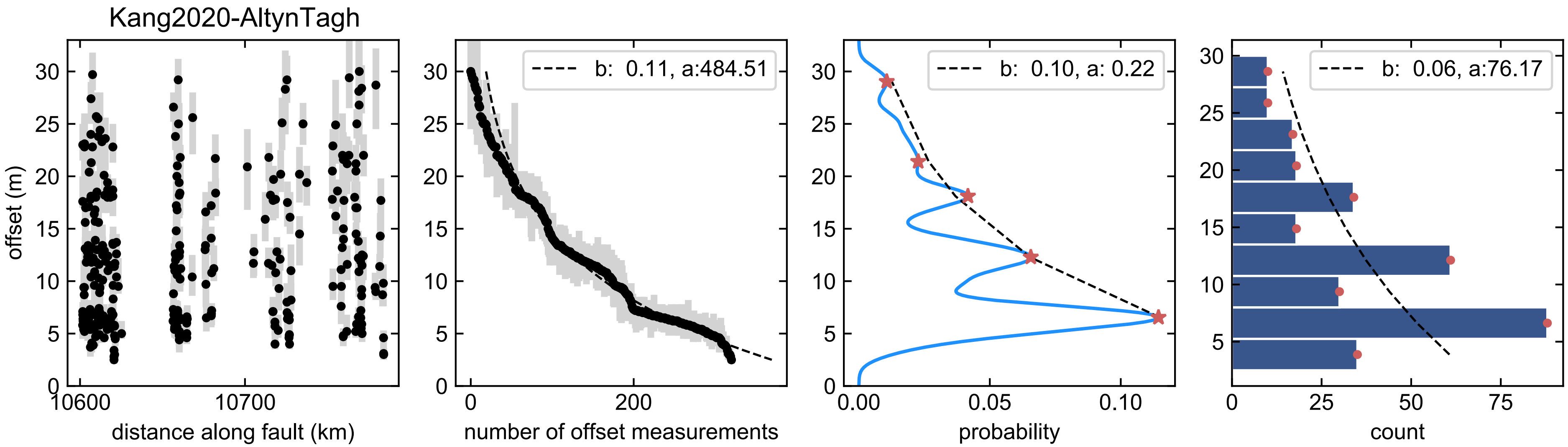

Kang2020-AltynTagh
offset (m)
distance along fault (km)
10600
10700
number of offset measurements
b: 0.11, a:484.51
probability
b: 0.10, a: 0.22
count
b: 0.06, a:76.17

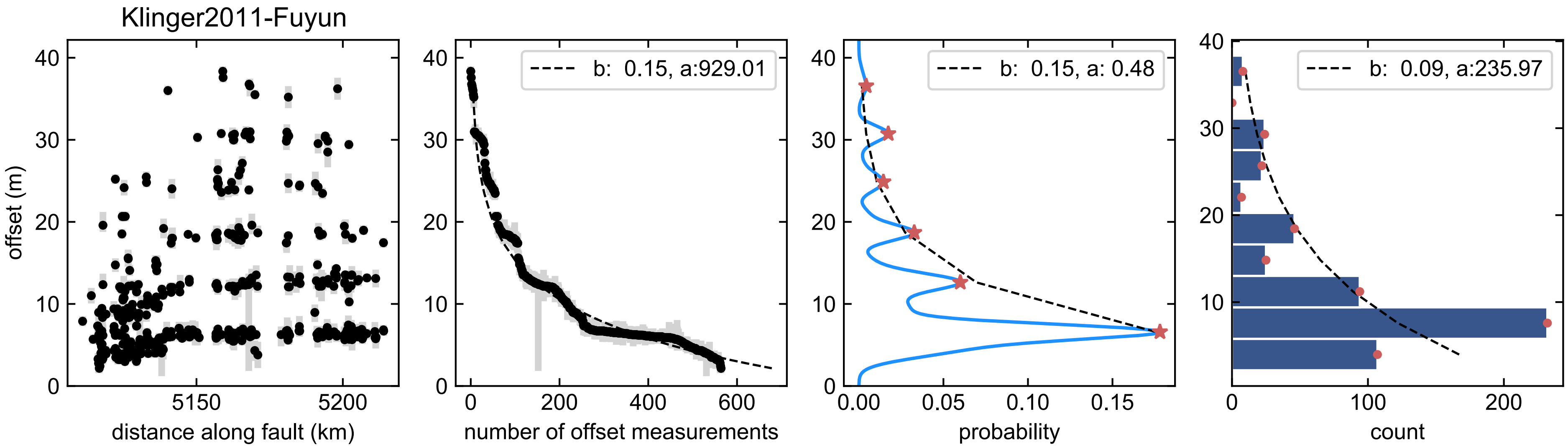

Klinger2011-Fuyun
offset (m)
40
30
20
10
0
5150
5200
distance along fault (km)
b: 0.15, a:929.01
0
200
400
600
number of offset measurements
b: 0.15, a: 0.48
0.00
0.05
0.10
0.15
probability
b: 0.09, a:235.97
0
100
200
count

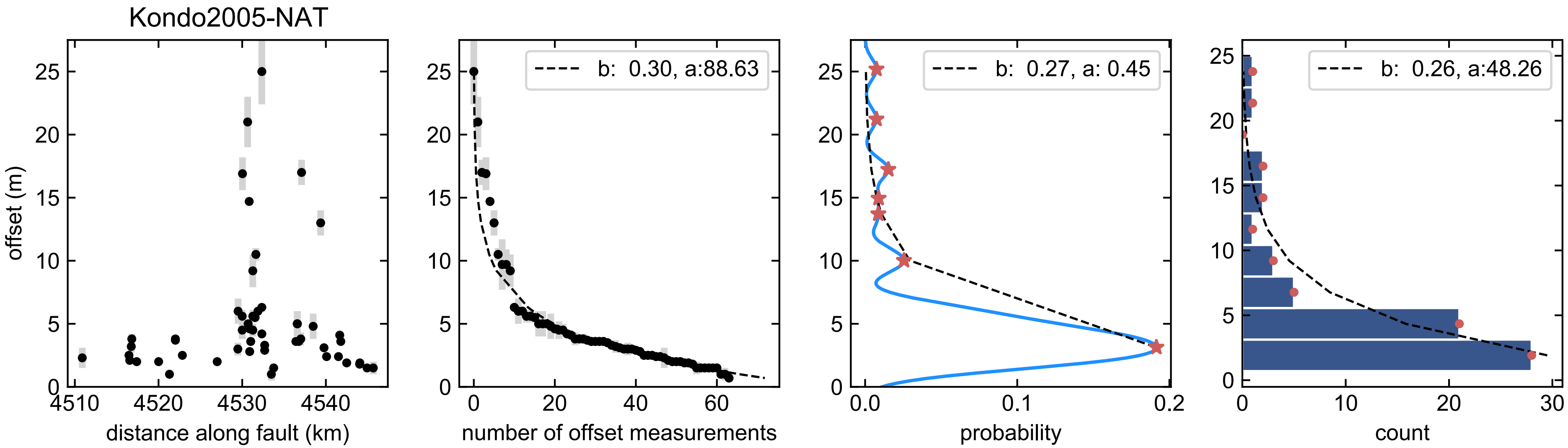

Kondo2005-NAT
offset (m)
distance along fault (km)
number of offset measurements
b: 0.30, a:88.63
probability
b: 0.27, a: 0.45
count
b: 0.26, a:48.26

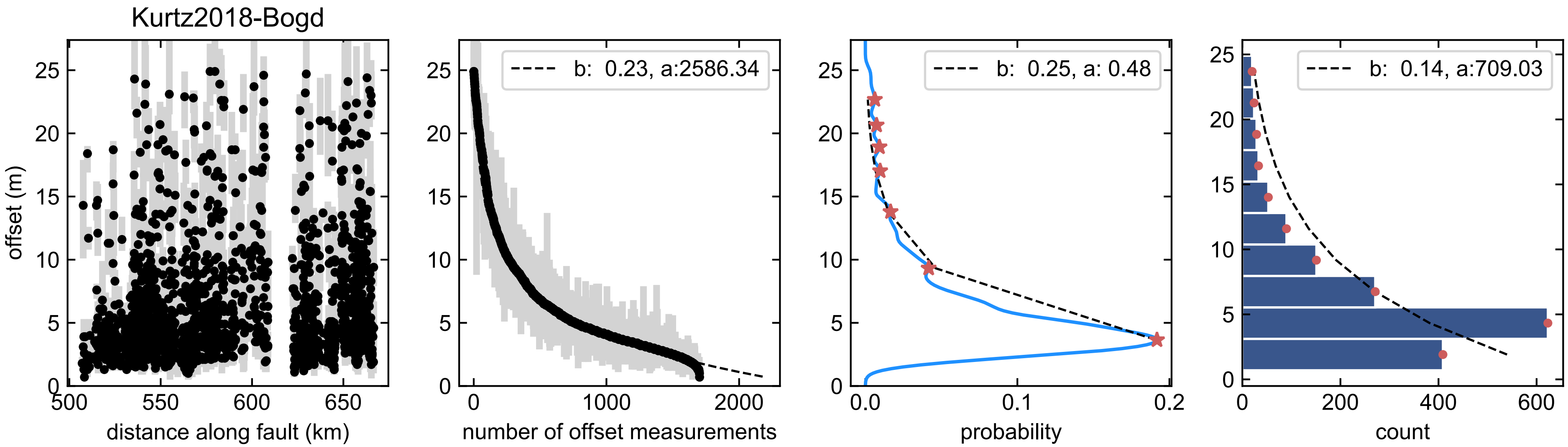

Kurtz2018-Bogd
offset (m)
distance along fault (km)
b: 0.23, a:2586.34
number of offset measurements
b: 0.25, a: 0.48
probability
b: 0.14, a:709.03
count

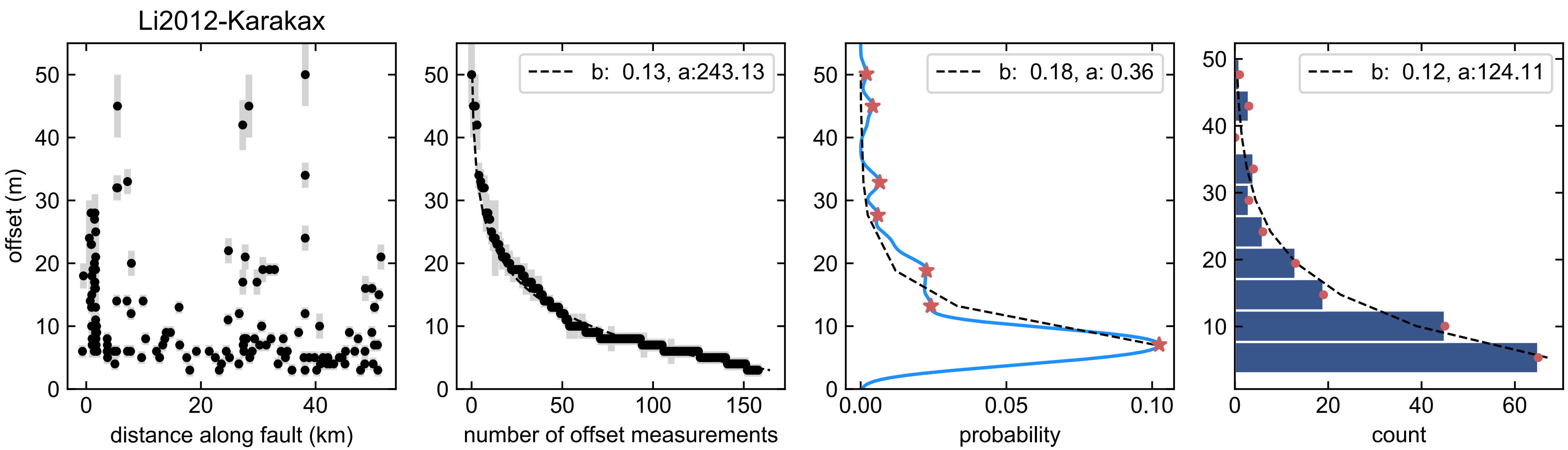

Li2012-Karakax
offset (m)
distance along fault (km)
b: 0.13, a:243.13
number of offset measurements
b: 0.18, a: 0.36
probability
b: 0.12, a:124.11
count

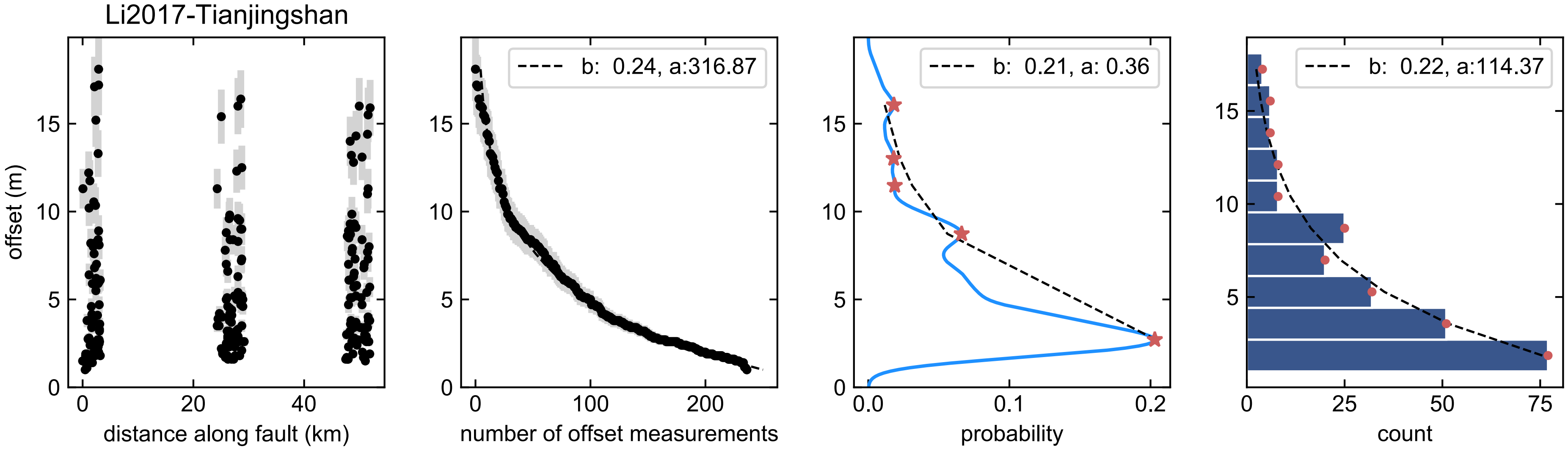

Li2017-Tianjingshan
offset (m)
distance along fault (km)
b: 0.24, a:316.87
number of offset measurements
b: 0.21, a: 0.36
probability
b: 0.22, a:114.37
count

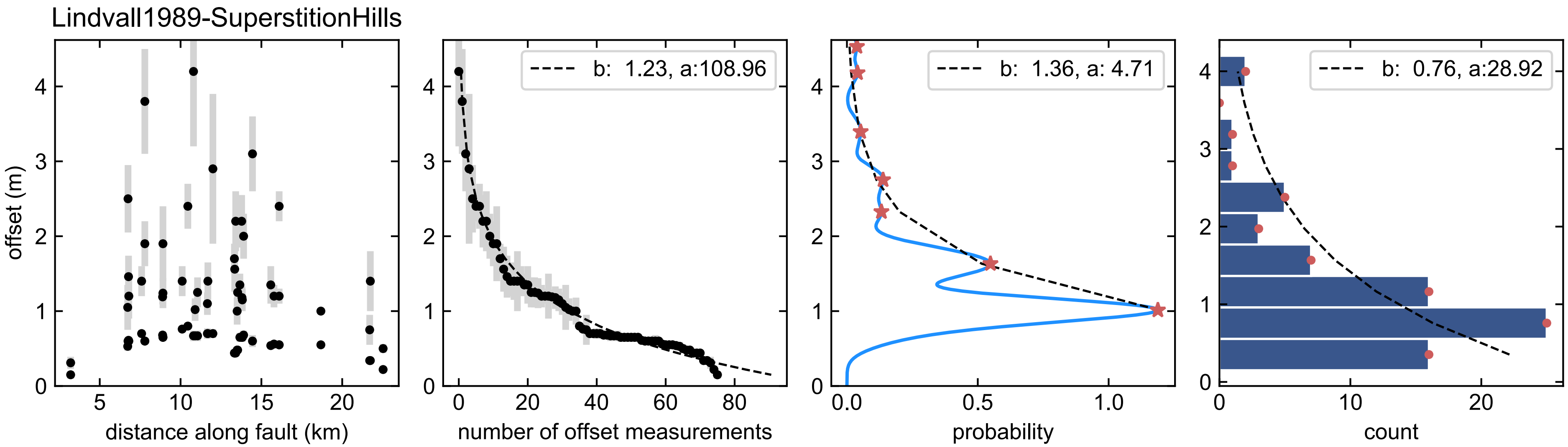
Lindvall1989-SuperstitionHills
offset (m)
distance along fault (km)
number of offset measurements
b: 1.23, a:108.96
probability
b: 1.36, a: 4.71
count
b: 0.76, a:28.92

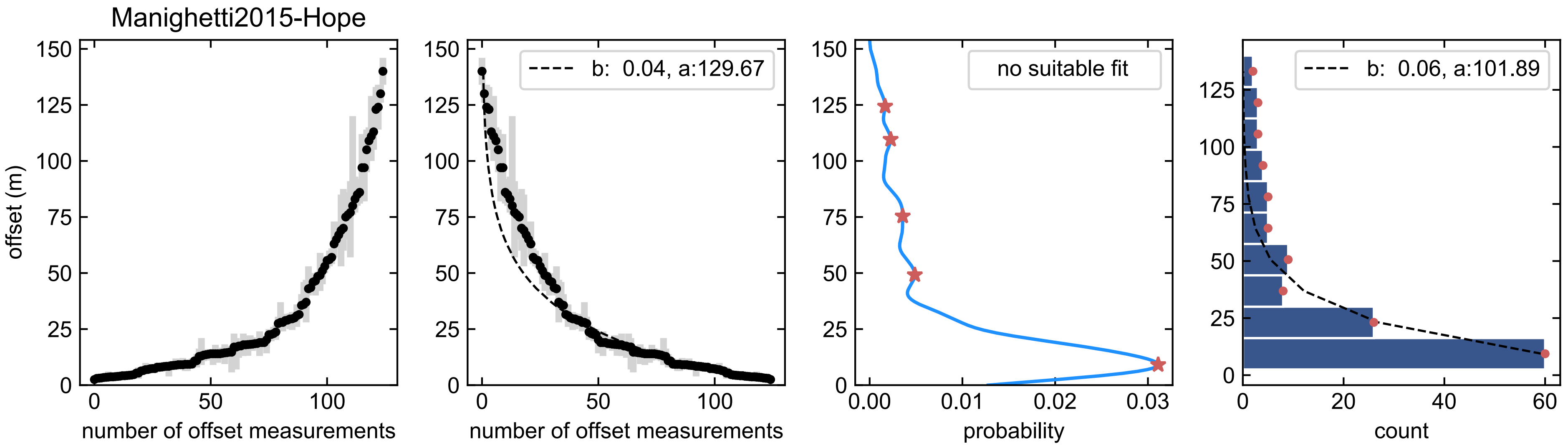
Manighetti2015-Hope
offset (m)
number of offset measurements
b: 0.04, a:129.67
number of offset measurements
no suitable fit
probability
b: 0.06, a:101.89
count

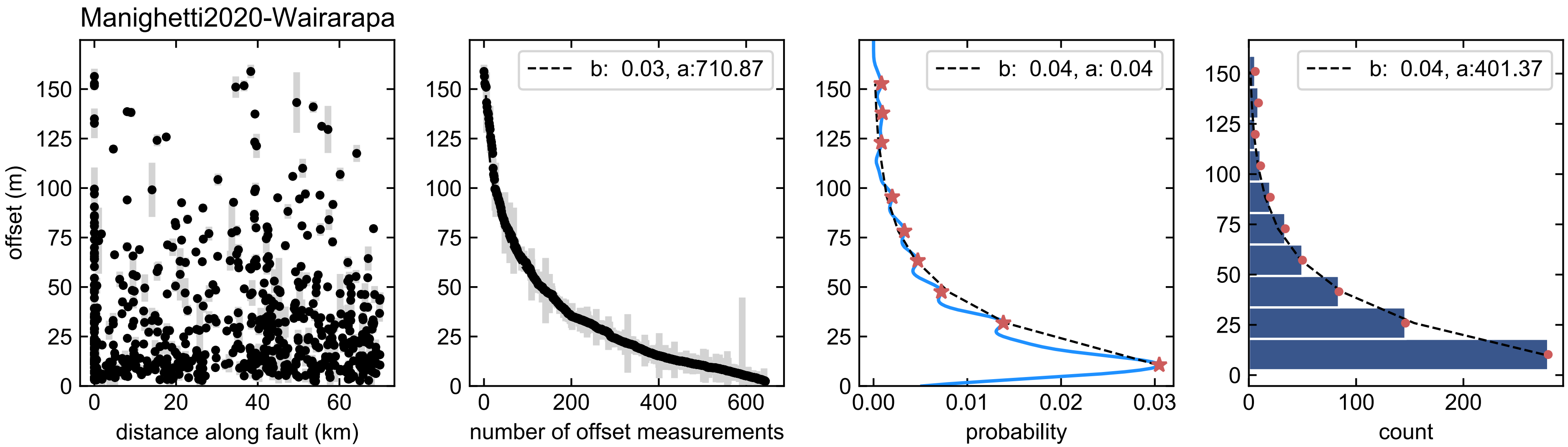

Manighetti2020-Wairarapa
offset (m)
distance along fault (km)
number of offset measurements
b: 0.03, a:710.87
probability
b: 0.04, a: 0.04
count
b: 0.04, a:401.37

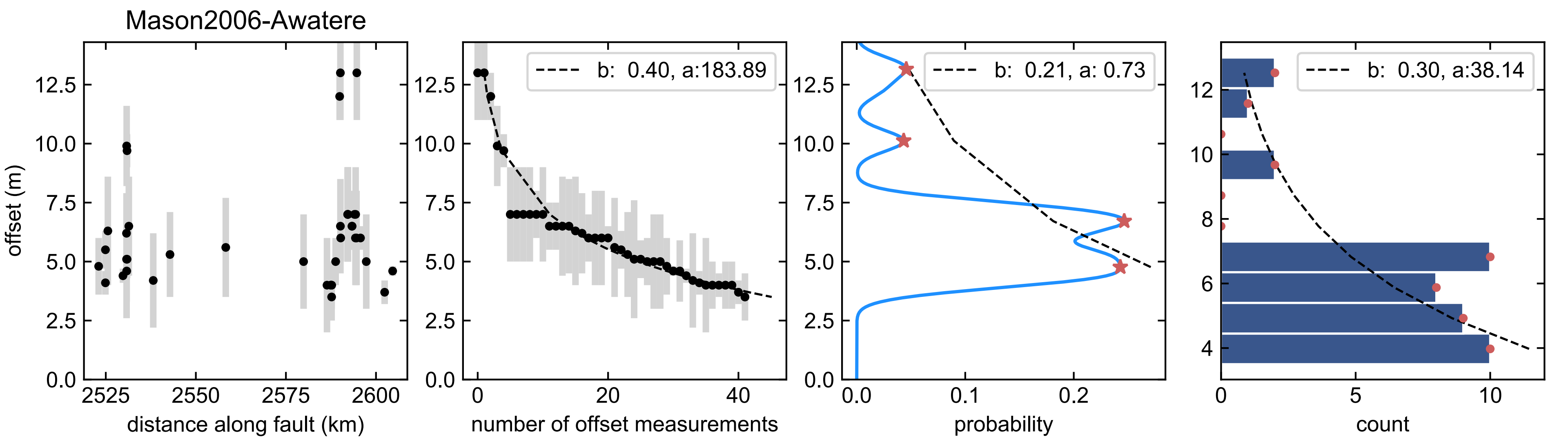
Mason2006-Awatere
offset (m)
distance along fault (km)
number of offset measurements
b: 0.40, a:183.89
probability
b: 0.21, a: 0.73
count
b: 0.30, a:38.14

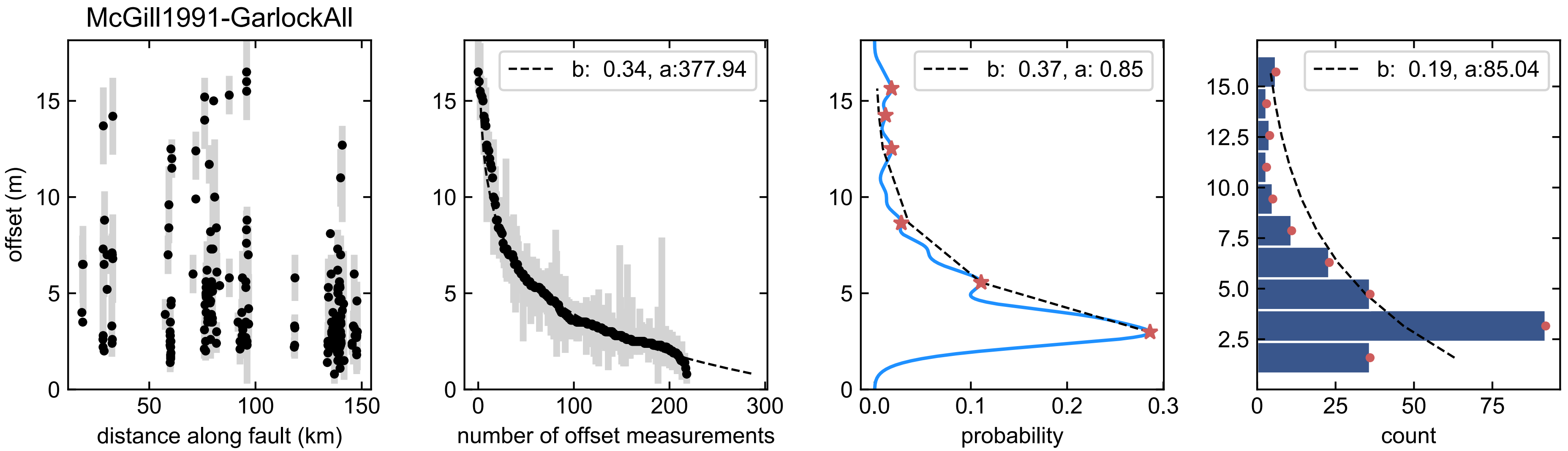
McGill1991-GarlockAll
offset (m)
distance along fault (km)
b: 0.34, a:377.94
number of offset measurements
b: 0.37, a: 0.85
probability
b: 0.19, a:85.04
count

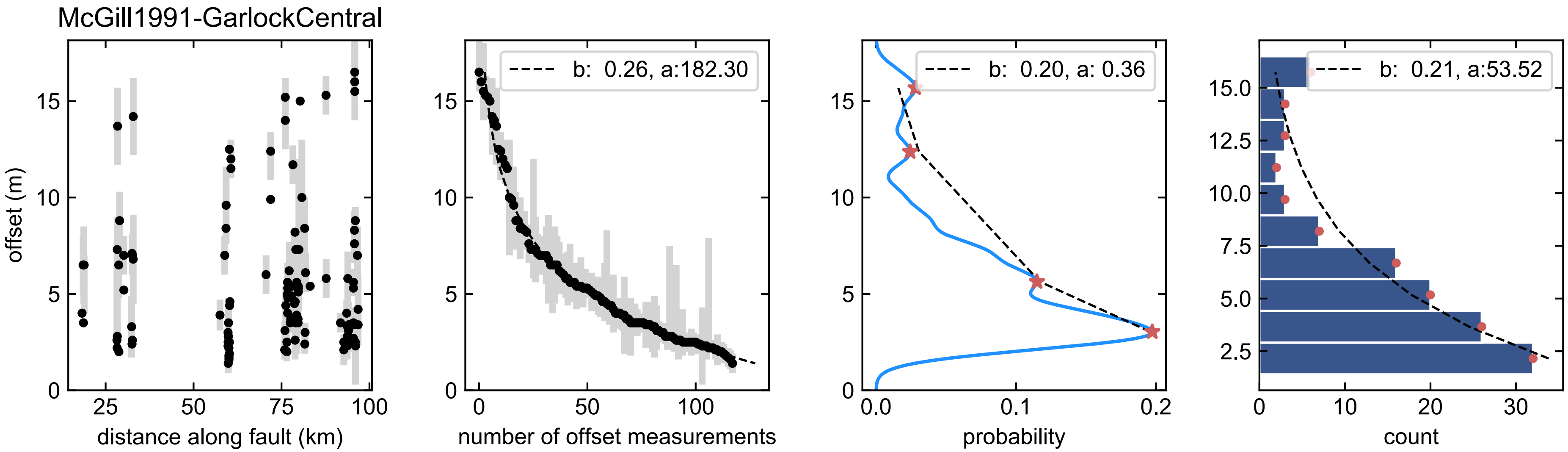

McGill1991-GarlockCentral
offset (m)
distance along fault (km)
b: 0.26, a:182.30
number of offset measurements
b: 0.20, a: 0.36
probability
b: 0.21, a:53.52
count

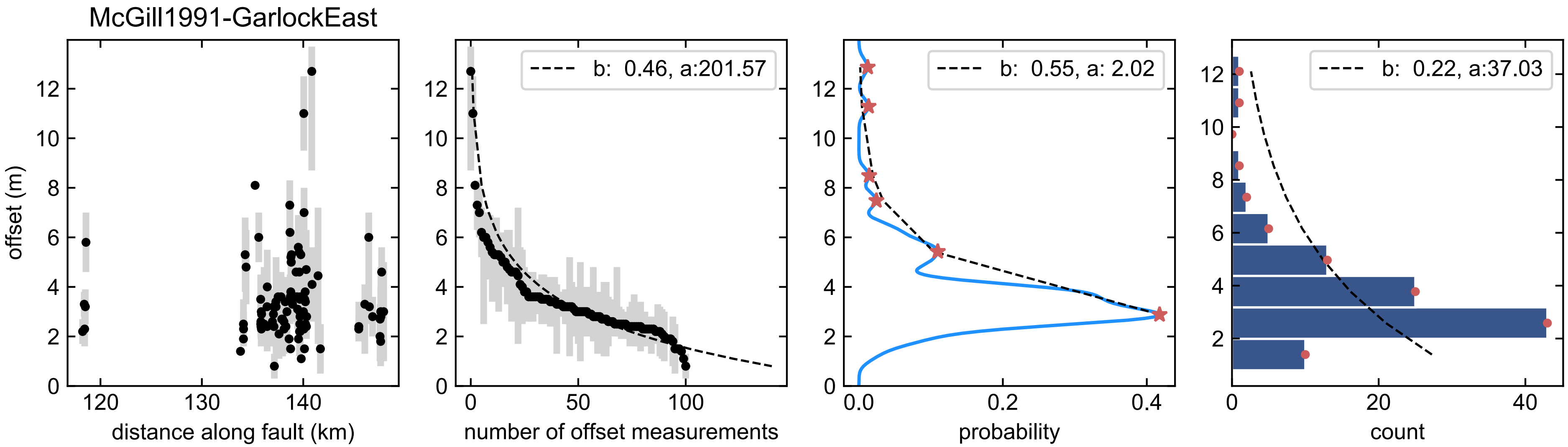

McGill1991-GarlockEast
offset (m)
distance along fault (km)
number of offset measurements
b: 0.46, a:201.57
probability
b: 0.55, a: 2.02
count
b: 0.22, a:37.03

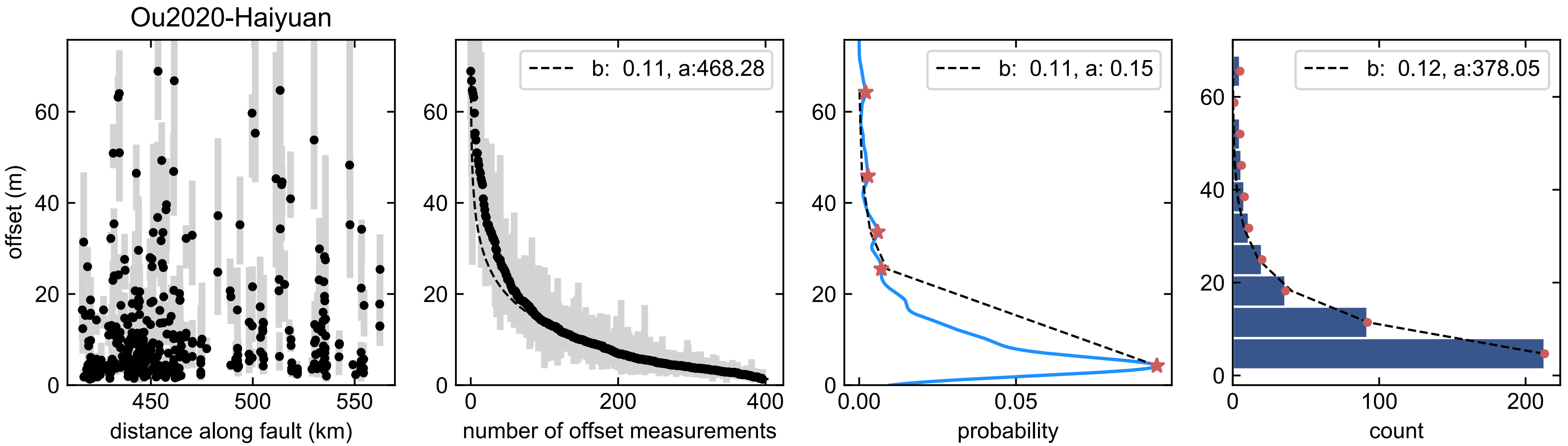

Ou2020-Haiyuan
offset (m)
distance along fault (km)
number of offset measurements
b: 0.11, a:468.28
probability
b: 0.11, a: 0.15
count
b: 0.12, a:378.05

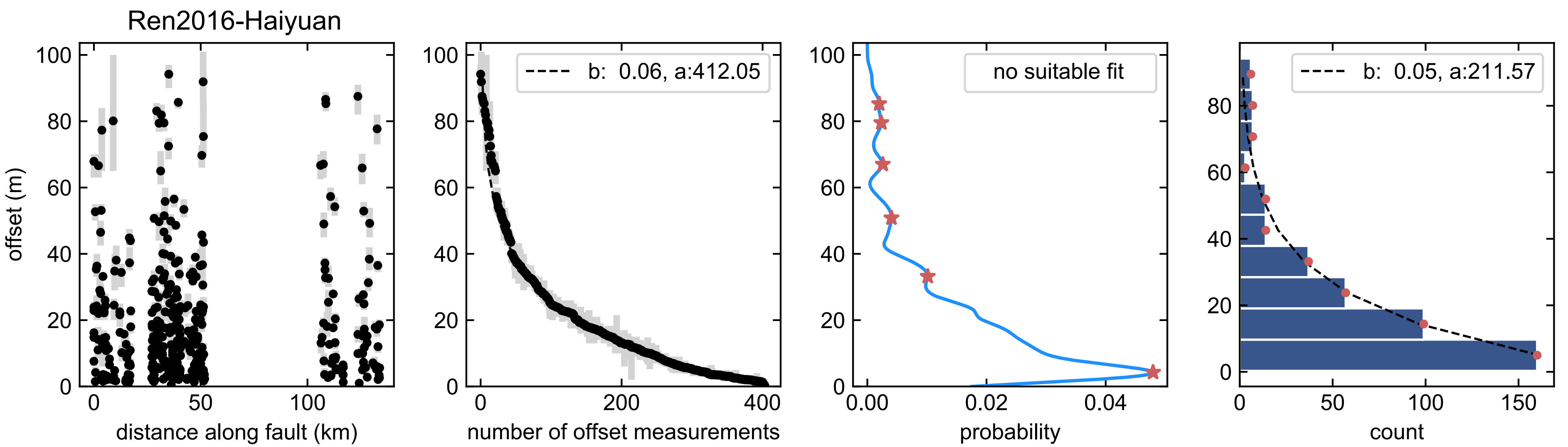
Ren2016-Haiyuan
offset (m)
distance along fault (km)
b: 0.06, a:412.05
number of offset measurements
no suitable fit
probability
b: 0.05, a:211.57
count

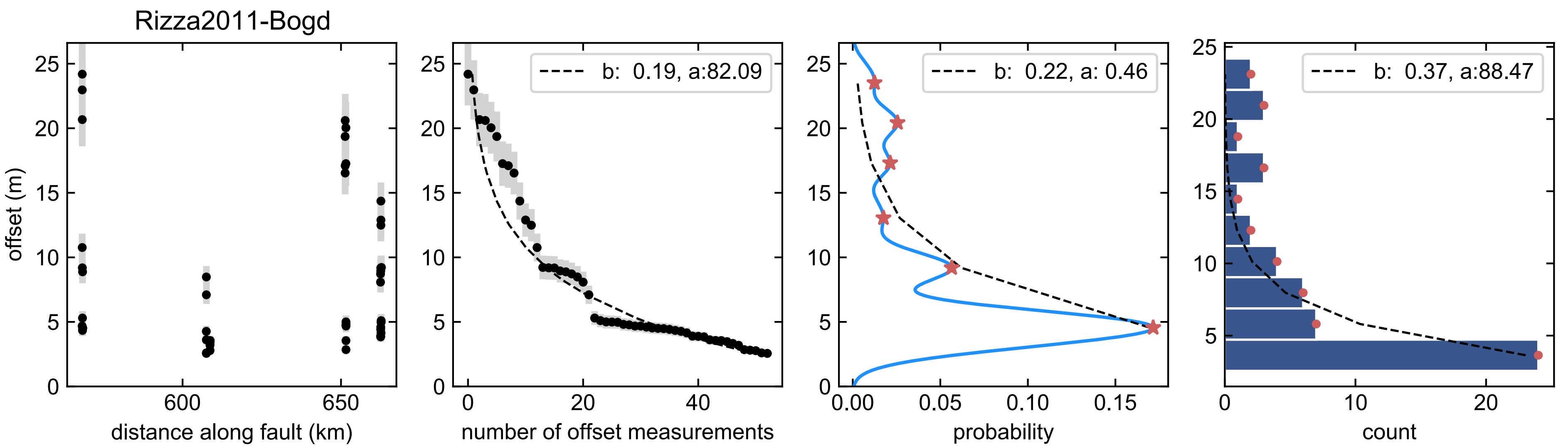

Rizza2011-Bogd
offset (m)
distance along fault (km)
b: 0.19, a:82.09
number of offset measurements
b: 0.22, a: 0.46
probability
b: 0.37, a:88.47
count

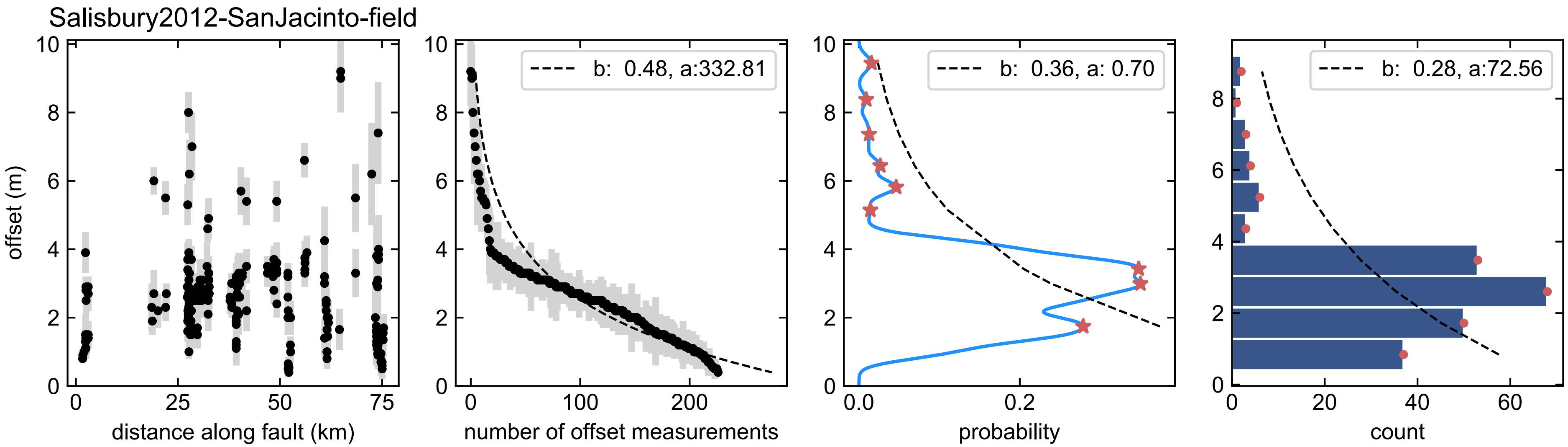

Salisbury2012-SanJacinto-field
offset (m)
distance along fault (km)
number of offset measurements
b: 0.48, a:332.81
probability
b: 0.36, a: 0.70
count
b: 0.28, a:72.56

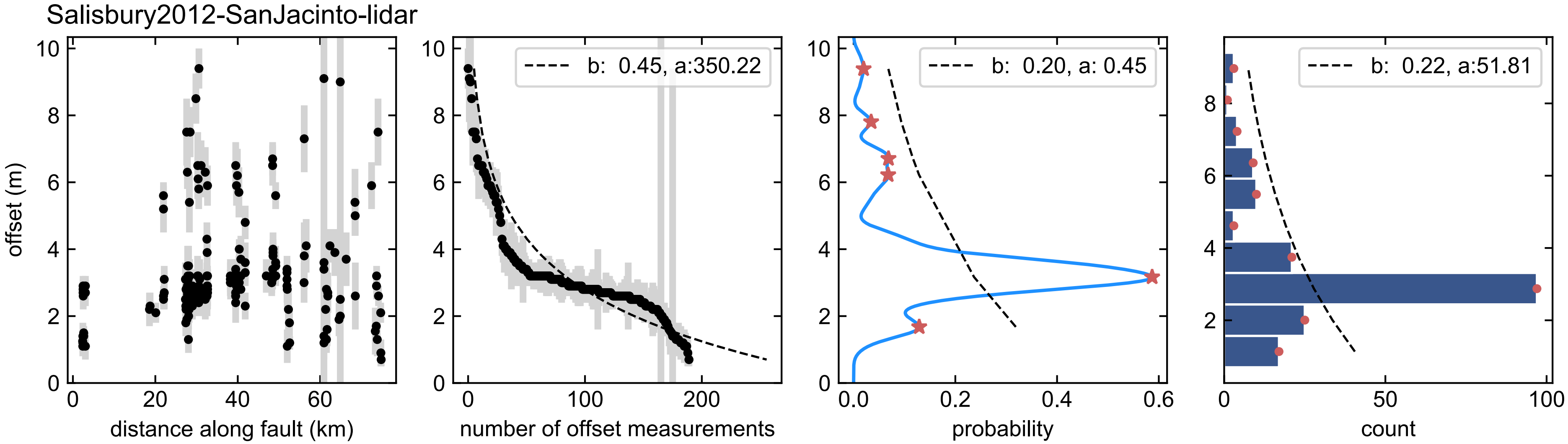

Salisbury2012-SanJacinto-lidar
offset (m)
distance along fault (km)
number of offset measurements
b: 0.45, a:350.22
probability
b: 0.20, a: 0.45
count
b: 0.22, a:51.81

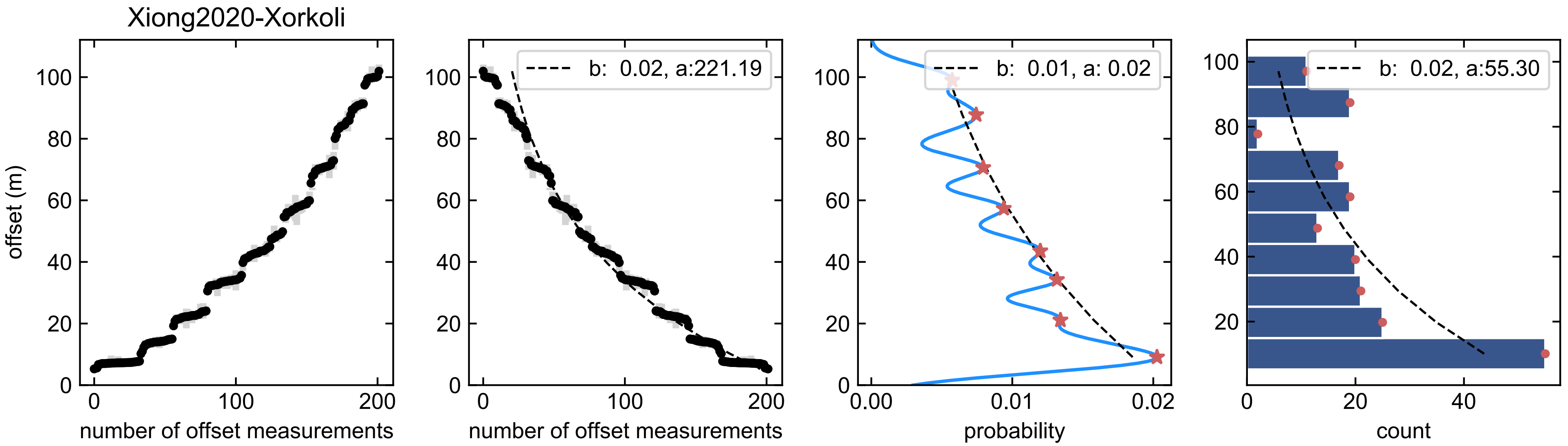

Xiong2020-Xorkoli
offset (m)
number of offset measurements
number of offset measurements
b: 0.02, a:221.19
probability
b: 0.01, a: 0.02
count
b: 0.02, a:55.30

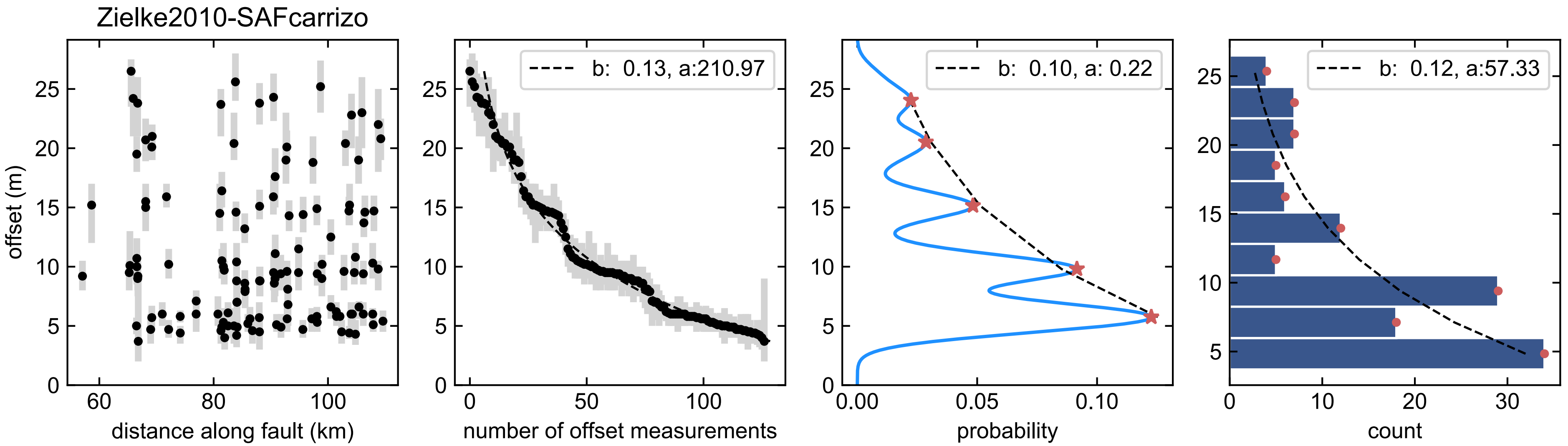

Zielke2010-SAFcarrizo
offset (m)
distance along fault (km)
b: 0.13, a:210.97
number of offset measurements
b: 0.10, a: 0.22
probability
b: 0.12, a:57.33
count

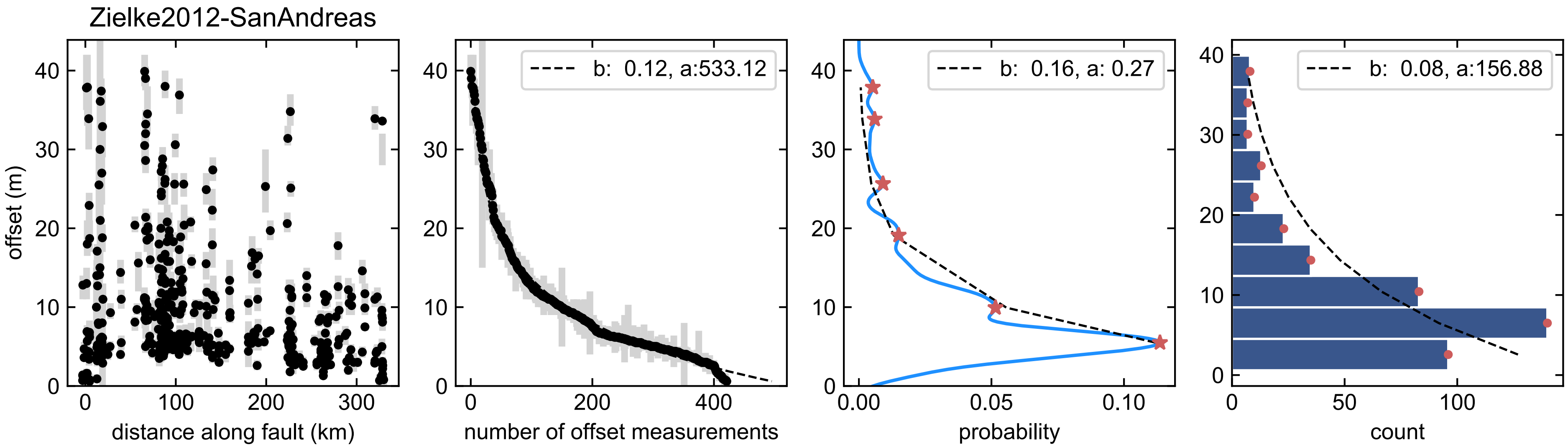
Zielke2012-SanAndreas
offset (m)
distance along fault (km)
b: 0.12, a:533.12
number of offset measurements
b: 0.16, a: 0.27
probability
b: 0.08, a:156.88
count

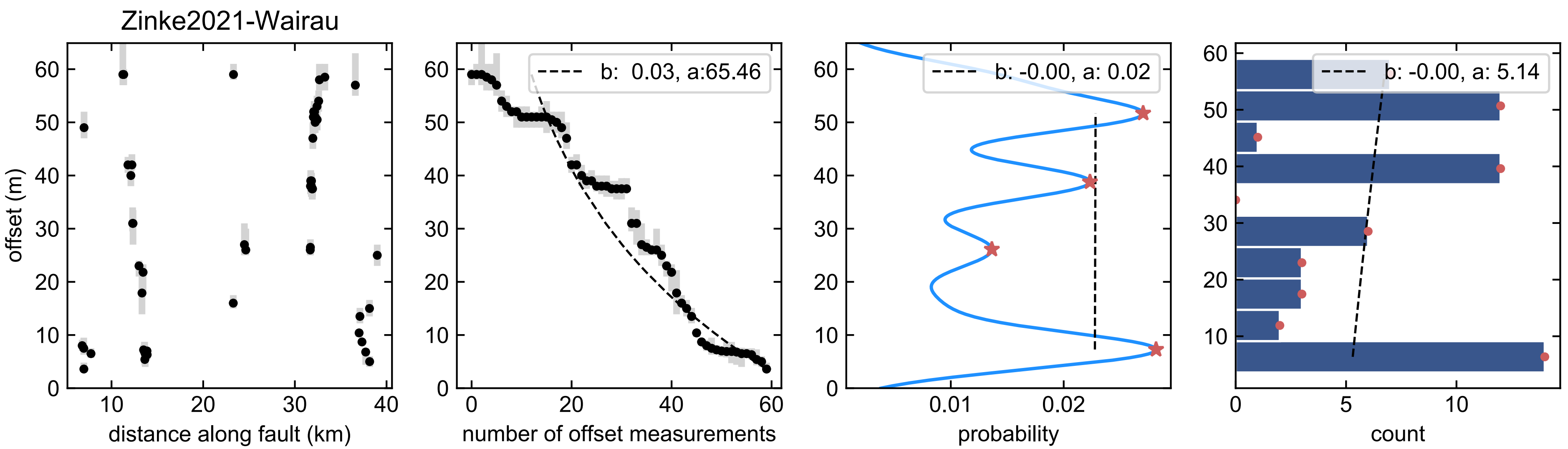

Zinke2021-Wairau
offset (m)
distance along fault (km)
b: 0.03, a:65.46
number of offset measurements
b: -0.00, a: 0.02
probability
b: -0.00, a: 5.14
count